

https://dspace.org/

Effectiveness of laser shock peening in post-processing additive manufactured Ti-6Al-4V

Ivanovic, N

2021
https://hdl.handle.net/10539/33003

Downloaded from a DSpace repository. https://dspace.org/



SCHOOL OF MECHANICAL,
INDUSTRIAL & AERONAUTICAL
ENGINEERING

Effectiveness of Laser Shock Peening in Post-processing Additive Manufactured Ti-6Al-4V

MECN8000 - MSc Dissertation

N Ivanovic

Student number: 363397

Supervisor: Prof. Claudia Polese (Wits), Co-supervisor: Prof. Igor Yadroitsev (CUT)

A dissertation submitted to the Faculty of Engineering and the Built Environment, University of the Witwatersrand, Johannesburg, in fulfilment of the requirements for the degree of Master of Science in Engineering.

Johannesburg, October 2021

Declaration

I declare that this dissertation is my own, unaided work, except where otherwise acknowledged. It is being submitted for the degree of Master of Science in Engineering in the University of the Witwatersrand, Johannesburg. It has not been submitted before for any degree or examination at any other university.

Signed this 9th day of October 2021



N Ivanovic

Acknowledgements

I would like to thank the following people and institutions for their contributions:

- My family and friends for their love and support.
- My supervisor, Prof. Claudia Polese of the University of the Witwatersrand, for her unwavering patience, support and motivation in the pursuit of this project.
- My co-supervisor, Prof. Igor Yadroitsev of the Centre for Rapid Prototyping and Development (CRPM) for his expert guidance and teachings on the intricacies of the Laser Powder Bed Fusion (L-PBF) Process.
- Prof. Willie du Preez, for his kindness and enthusiasm to facilitate this collaboration.
- Dr Daniel Glaser of the Council for Scientific and Industrial Research (CSIR) National Laser Centre for assistance in Laser Shock Peening.
- Mr Sean van Staden for teaching me the patient art of incremental hole drilling and his support in the project as a whole.
- Mr Gerrard Peters of the Wits School of Physics Material Preparation Lab.
- The Department of Science and Innovation's National Research Foundation (DSI-NRF) Centre of Excellence in Strong Materials (CoE-SM) for sponsoring this project.
- Mrs Marina Labuschagne of the DSI-NRF CoE-SM, for her kindness in assisting me with administrative matters.
- Prof. Lesley Cornish, Mrs Casey Sparks and Mrs Jacqui Jacobs of the DSI-NRF CoE-SM for all their help and support in this project.
- The Centre for Rapid Prototyping and Manufacturing (CRPM) of Central University of Technology (CUT) for the use of their machines, and manufacturing samples.
- Dr Ina Yadroitsava for her kind assistance in sample preparation, optical microscopy and expert opinion at the CUT Microscopy Unit.

- The Centre for Scientific and Industrial Research - National Laser Centre (CSIR NLC) Rental Pool Program (RPP), funded by the DSI.
- The DSI Collaborative Program in Additive Manufacturing (CPAM), the implementation programme for the South African Additive Manufacturing strategy, for the supporting research funds.

Abstract

The purpose of this work was to set the groundwork for post-processing Additive Manufactured (AM) Ti-6Al-4V manufactured by Laser Powder Bed Fusion (L-PBF) using the Laser Shock Peening (LSP) surface treatment process. Samples of varying thicknesses were manufactured on a wrought substrate plate, and one half of the samples were processed using LSP. Residual stresses were measured using Laboratory X-Ray Diffraction and Incremental Hole Drilling techniques. These measurements showed that LSP is capable of successfully inducing compressive residual stress to a good depth and magnitude in as-built AM Ti-6Al-4V samples. Surface roughness was measured and showed a decrease in surface roughness after LSP treatment. This was attributed to the peaks being affected more than the valleys by the peening action of the expanding plasma. Microhardness was investigated along the depth of an LSP treated sample and its measurements compared to as-built AM Ti-6Al-4V as well as wrought Ti-6Al-4V plate. The microhardness of AM Ti-6Al-4V was more than double that of the wrought Ti-6Al-4V plate. LSP treatment increased the microhardness slightly. Optical microscopy and SEM were used to inspect the grain structure and surface morphology of the samples before and after LSP treatment. No difference in microstructure was observed between as-built and LSP treated material. Atypical oxidation was found on the LSP treated samples, characteristic of the extreme temperatures, pressures and presence of oxygen during the LSP process. This research forms the groundwork of knowledge in the combined capability of AM and LSP technologies to potentially produce highly complex components for specialised industries such as aerospace.

Contents

Declaration i

Acknowledgements ii

Abstract iv

Contents v

List of Figures x

1 Introduction 1

2 Literature Survey 2

2.1 Additive Manufacturing 2

2.1.1 Overview 2

2.1.2 Additive Manufacturing Applications 4

2.1.2.1 Aerospace 4

2.1.2.2 Tooling 4

2.1.2.3 Medical 5

2.1.3 Types of Additive Manufacturing Processes 5

2.1.4 Powder Bed Fusion 6
2.2 Laser Powder Bed Fusion Part Performance 8
2.3 Titanium Alloy (Ti-6Al-4V) 11
2.3.1 Overview 11
2.3.2 Phases and Alloying 12
2.3.3 Titanium Beneficiation Program in South Africa 12
2.4 Laser Shock Peening 12
2.4.1 Laser Shock Peening System Parameters 13
2.4.2 Effects of Laser Shock Peening 14
2.4.2.1 Residual Stress 14
2.4.2.2 Deformation 16
2.4.2.3 Surface Roughness 16
2.4.2.4 Microhardness 17
2.5 Residual Stress Measurement 18
2.5.1 Incremental Hole Drilling 18
2.5.2 Diffraction-Based Methods 19
2.5.2.1 Laboratory X-Ray Diffraction 20
2.5.2.2 Synchrotron X-Ray Diffraction 20
2.5.2.3 Neutron Diffraction 20
2.6 Objectives 20

3 Methods and Experimental Setup **22**

3.1 Laser Powder Bed Fusion 22

3.1.1 Apparatus . . . 23
3.1.2 Process Parameters . . . 23
3.2 Laser Shock Peening . . . 24
3.2.1 Method . . . 24
3.2.2 Process Parameters . . . 25
3.3 Surface Roughness . . . 25
3.3.1 Method . . . 26
3.4 X-Ray Diffraction . . . 27
3.4.1 Method . . . 27
3.5 Incremental Hole Drilling . . . 28
3.5.1 Method . . . 28
3.5.1.1 Mounting Strain Gauge . . . 28
3.5.1.2 Wiring . . . 29
3.5.1.3 Alignment and Positioning . . . 29
3.5.1.4 Drilling . . . 30
3.5.1.5 Strain Data Processing . . . 30
3.6 Microhardness . . . 31
3.6.1 Method . . . 31
3.7 Light Microscopy . . . 32
3.7.1 Preparation . . . 33
3.8 Scanning Electron Microscopy . . . 34
3.8.1 Method . . . 35

4 Results and Discussion **36**

4.1 Laser Powder Bed Fusion 36

4.2 Laser Shock Peening 38

4.3 Surface Roughness 40

4.4 X-Ray Diffraction 41

4.5 Incremental Hole Drilling 42

4.6 Microhardness 44

4.7 Light Microscopy 46

4.8 Scanning Electron Microscopy 50

4.9 Comparison of Results to Literature 56

4.9.1 Residual Stress 56

4.9.2 Microhardness 57

4.9.3 Surface Roughness 57

5 Conclusions and Recommendations **58**

5.1 Conclusion 58

5.2 Evaluation of Objectives 59

5.3 Recommendations 59

6 Contributions to the Scientific Community **60**

6.1 Conferences 60

6.1.1 International Conference on Mechanical Stress Evaluation by Neutron and Synchrotron Radiation (MECA SENS) 60

6.1.2 18th Annual Rapid Product Development Association of South Africa (RAPDASA) Conference 60

6.1.3 International Conference on Laser Peening and Related Phenomena (ICLPRP) 60

6.2 Workshops 61

6.2.1 African Laser Center (ALC) Student Workshop 61

6.3 Awards 61

Appendix A Conference Abstracts, Proceedings and Posters **68**

Appendix B Engineering drawing of sample array **90**

Appendix C L-PBF Powder Specification **91**

Appendix D Incremental Hole Drilling ASTM Standard **92**

List of Figures

2.1 Subtractive vs Additive Manufacturing Geometry [6] 2

2.2 Human Femur [9] 3

2.3 Topology Optimised Hinge (Airbus A380) [12] 4

2.4 Tool Insert with Conformal Cooling [13] 5

2.5 Hemi-Maxilla Implant [14] 5

2.6 L-PBF Process [17] 7

2.7 Fatigue Failure of Bolt [18] 8

2.8 Shot Peening Residual Stress [25] 9

2.9 Residual Stress Simplified 10

2.10 Compressive Residual Stress Benefit 11

2.11 LSP Diagram 13

2.12 Residual Stress Before and After LSP [37] 14

2.13 Residual Stress at Various Process Conditions [38] 15

2.14 Microhardness Before and After LSP [37] 17

2.15 Microhardness at Various Process Conditions and LSP Laser Power [38] . . . 17

2.16 IHD Diagram (a) and ASTM Type A Strain Gauge Rosette (b) 18

2.17 Diffraction Theory [43] 19

3.1 Planned Sample Array 22
3.2 EOSINT M280 L-PBF Machine [47] 23
3.3 LSP 25
3.4 SR Measurement Device PS1 26
3.5 Proto iXRD [48] 27
3.6 Restan MTS3000 [49] 28
3.7 Drilling Process 30
3.8 Stereo-Discovery-V8 Light Microscope [50] 32
3.9 Buehler IsoMet LS [51] 33
3.10 Struers LaboPol System [52] 34
3.11 Zeiss Sigma SEM [53] 35

4.1 Printed Samples 36
4.2 Dino-Lite AM3111 37
4.3 AM Surface (20X Magnification) 37
4.4 AM Surface (75X Magnification) 38
4.5 Peened Surface (20X Magnification) 39
4.6 Peened Surface (75X Magnification) 39
4.7 Surface Roughness Comparison (R_a) 40
4.8 Surface Roughness Comparison (R_z) 40
4.9 XRD 0 Layers 41
4.10 XRD 10 Layers 41
4.11 Residual Stress Comparison in 80 Layer As-Built (a) and LSP (b) Samples . 43

4.12 Residual Stress Comparison in 40 Layer As-Built (a) and LSP (b) Samples . 43
4.13 Microhardness Indentation Array 44
4.14 Microhardness Comparison 45
4.15 Comparison Section 46
4.16 Plate Low Magnification 47
4.17 Ti-6Al-4V Plate High Magnification 47
4.18 AM Boundary 48
4.19 AM Low Magnification LSP Sample 49
4.20 AM High Magnification LSP Treated Region 49
4.21 SEM AM 100X 50
4.22 SEM AM 1000X 51
4.23 SEM AM Edge 51
4.24 SEM AM Last LSP Spot 52
4.25 SEM AM LSP Surface 500X 53
4.26 SEM AM LSP Surface 2000X 53
4.27 EDX Composition Plate 54
4.28 EDX Composition AM 54
4.29 EDX Composition AM LSP Last Spot 55
4.30 EDX Composition AM LSP Mid Raster 55
4.31 Comparison of LSP Parameters 56

1 Introduction

This research project is the result of a collaboration of the School of Mechanical, Industrial and Aeronautical Engineering at the University of the Witwatersrand, and the Centre for Rapid Prototyping and Manufacturing at the Central University of Technology. It contributes to the research and furthering of knowledge in the fields of Laser Shock Peening and Additive Manufacturing.

Laser Shock Peening (LSP) is a mechanical process of surface enhancement which exploits the energy delivery capability of a laser pulse. This laser pulse generates plasma at the surface whose rapid expansion results in a shock wave that travels into the material, plastically deforms the region, and leaves it in a state of compressive residual stress. This stress results in improved fatigue performance of components by preventing/retarding crack initiation and propagation. This technology has been used, amongst others, in the power generation and aerospace industries to improve the useful life of turbine blades which are under highly cyclic loading. [1]

Laser Powder Bed Fusion (L-PBF) is a type of Additive Manufacturing (AM) technology which builds metal parts up in layers from powder. For each layer of the part, a powder layer is deposited, and a laser selectively melts the two dimensional profile required. This process repeats until the part is complete. The cost of such a thermally demanding process is that the residual stresses (specifically tensile stresses) are detrimental to the performance of the part under fatigue loading. [2] [3] [4] To add to this effect, the L-PBF process results in surfaces of high roughness which also negatively impacts fatigue life.

The purpose of this research is thus to investigate the effectiveness of using LSP on L-PBF manufactured components, by measuring the residual stresses of LSP processed L-PBF samples and comparing to as-built samples. Samples of varying thickness are investigated, and multiple residual stress measurement methods are utilised. Ti-6Al-4V is the material of choice for this research project since it is widely used in AM and the aerospace industry. [5]

2 Literature Survey

The purpose of the literature survey below is to gain a general understanding of the fundamentals of the technologies, concepts and phenomena relevant to furthering the research in improving fatigue life of additive manufactured components. This review is not constrained to particular sources, but rather aims to widely explore the topics of Additive Manufacturing (specifically the process of Laser Powder Bed Fusion), the theory behind fatigue failure and its interplay with residual stress. This will be followed by an investigation into the field of Laser Shock Peening, its theory and applications. This review of literature will be concluded with a short investigation into the properties, characteristics and metallurgical details of Ti-6Al-4V which is to be used in this experiment.

2.1 Additive Manufacturing

2.1.1 Overview

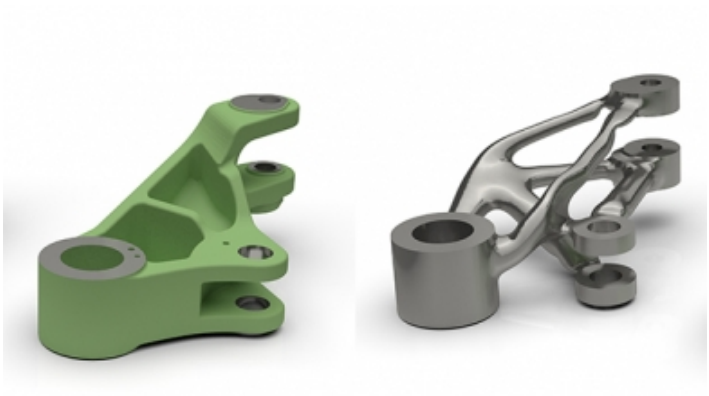


Figure 2.1: Subtractive vs Additive Manufacturing Geometry [6]

Figure 2.1 shows the difference in final geometry of additive manufacturing versus traditional (subtractive) manufacturing for a part with an identical purpose and expected loads.

In the machined part (left) it is clear from the artifacts of its primitive geometry that the part began its life as a stock piece of metal, upon which several machining operations were performed in order to achieve the final geometry, designed to remove as much material as required to reduce weight but retain strength. These machining methods however have significant physical restrictions based on the geometrical capabilities of a mill/CNC/lathe. [7]

The AM part (right) has been designed using a simulated topology optimisation, where 'dead' material (material which contributes to mass but does not contribute significantly to strength) has been minimised. The result bears a somewhat organic resemblance and contains just the right amount of material much like the structures of tree branches or animal bones both of which are, incidentally, additively manufactured (by cell division) for only the exact strength they require and the loads they are designed to bear, at very specific locations. Figure 2.2 shows how the structure of a human femur is highly specific to its localised function. The trabecular bone inside the femoral head bears compressive and tensile loads within the confines of the hip joint, while the cortical bone in the shaft bears compressive and flexural loads. [8]



Figure 2.2: Human Femur [9]

With these examples in mind, engineering should place increasing focus on biomimicry to design with inspiration from nature, since it is often the most efficient, leanest and cleverest designs that originate from our natural world. [10]

2.1.2 Additive Manufacturing Applications

2.1.2.1 Aerospace

AM can add value in the aerospace industry where there is a need for complexity and individuality and minimising weight. In the fields of aerospace (military and commercial) manufacturing time and rapid prototyping is of great importance, making AM an economically viable and elegant solution. [11]



Figure 2.3: Topology Optimised Hinge (Airbus A380) [12]

2.1.2.2 Tooling

Eliminating the need for tool-path generation and time consuming processes like Electric Discharge Machining (EDM), tool inserts can be designed and built with a very short lead time compared to conventional methods. Furthermore, the geometrical freedom allows for optimisation of tool performance. For example in plastic injection moulding, rapid and uniform cooling is paramount in ensuring efficient manufacture and preventing warping of parts. [11] This is achieved through the incorporation of conformal cooling channels in the tool inserts as shown in Figure 2.4.

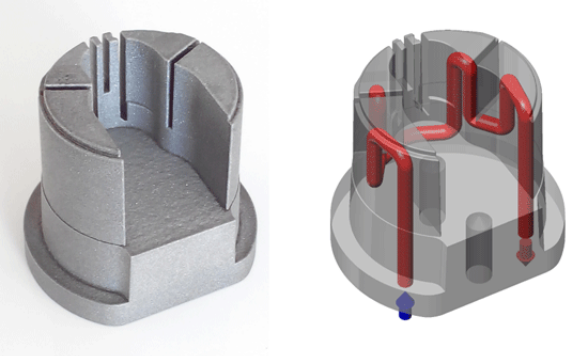


Figure 2.4: Tool Insert with Conformal Cooling [13]

2.1.2.3 Medical

Medical implants and devices are highly complex and valuable products. Furthermore, they require custom geometries tailored to the patient since each individual's anatomy is slightly different. Conforming the geometry of a medical implant tightly to a patient's anatomy is key in minimising operating time, and preventing complications from poor fits. These capabilities coupled with high variance in designs and small volumes of each design (often only one part manufactured), makes AM the manufacturing technology of choice for this application. [11]



Figure 2.5: Hemi-Maxilla Implant [14]

2.1.3 Types of Additive Manufacturing Processes

There are seven classifications of AM processes according to ASTM standard F42. [15]

- Vat photopolymerisation
- Sheet lamination

- Powder bed fusion
- Directed energy deposition
- Material jetting
- Binder jetting
- Material extrusion

Each process has its characteristic range of materials, cost considerations, manufacturing process limitations/complexities and part performance implications. For the purposes of this research, focus will be placed on the powder bed fusion process.

2.1.4 Powder Bed Fusion

Powder bed systems deposit a layer of powder of material on a substrate plate, and a beam of energy selectively melts a profile of the powder, fusing the profile to the material below. This process is repeated for each layer deposited (usually on the order of micrometers thickness), until the part is built up fully. The part is then removed from the loose powder and cut off the substrate plate. Powder bed systems which utilise a laser as the energy beam are available from various suppliers and are under trade names such as Selective Laser Melting (SLM), Laser Cusing, and Direct Metal Laser Sintering (DMLS). A similar process called Electron Beam Melting (EBM) exists which differs from the laser-based processes in that it utilises electrons as its energy beam and as such requires a full vacuum in the build chamber. [16]

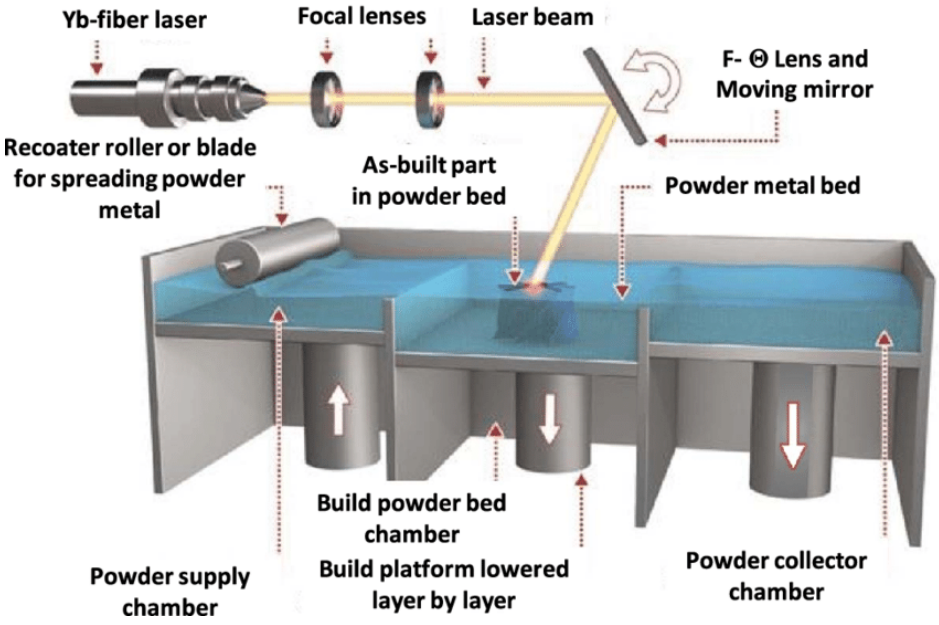


Figure 2.6: L-PBF Process [17]

This research project will make use of the metal L-PBF process for Additive Manufacturing. Figure 2.6 shows a diagrammatic representation of a typical L-PBF machine where the printing process follows these steps:

1. A base plate is mounted on the surface of the print bed (5)
2. Metal powder is loaded into feed chamber (8)
3. Re-coat arm (7) deposits a thin layer of powder on the base plate with excess powder falling into the overflow catch (10)
4. Laser (1) melts the required profile into the layer of powder by means of a X-Y scanning mirror galvanometer (3)
5. Print bed moves downward equal to the distance of the pre-set layer height
6. The machine repeats steps 3 to 5 until the part is complete
7. The base plate along with the parts (6) is removed from the powder, cleaned from excess powder and sent for post processing
8. Part is stress relieved, heat treated, cut off the base plate, machined and finished with a range of techniques

2.2 Laser Powder Bed Fusion Part Performance

Components in static applications are designed based on a function of their yield strength or deflection considerations. In a cyclic loading scenario where the load is applied and removed (or reversed) many times, flaws in the material could lead to cracking and ultimately total fatigue failure (see Figure 2.7) even at loads well below the yield strength of the material. [18]

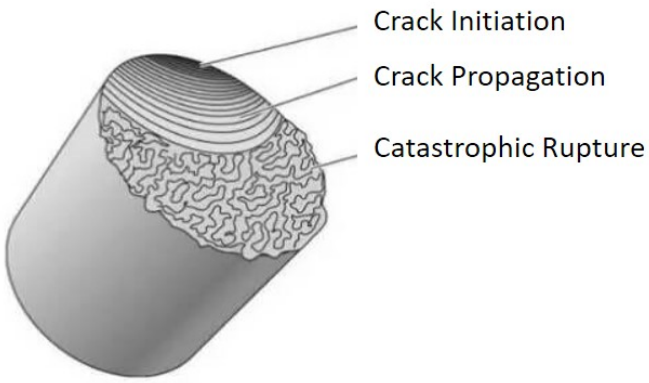


Figure 2.7: Fatigue Failure of Bolt [18]

Fatigue failure has three stages:

1. A small crack nucleates at or just below the surface of a component where it experiences the highest tensile stresses. This usually occurs at locations of scratches, burrs, pitting, sharp changes in geometry, atomic inclusions, grain boundaries, or regions of high dislocation density.

2. The small crack propagates slowly with each cycle of tension. This happens initially at a very slow rate, however with sequential growth of the crack, the component becomes weaker locally, and the load on the crack increases, which accelerates the rate of crack growth.

3. Finally, the remaining material undergoes sudden plastic fracture, when it is too weak to support the applied load statically.

Cracks grow with each tensile portion of a cyclic loading, so preventing a state of tension in regions where flaws are expected (usually the surface), would delay fatigue failure greatly.

With this in mind, measures need to be taken to reduce the possibility of cracking by ensuring a smooth surface and preventing the surface of a material from experiencing tension altogether. [18]

Due to the nature of the L-PBF manufacturing process, the residual stresses present in the as-built component are very high and often tensile at surfaces. [19] In addition to this, it is well documented that L-PBF component surface roughness is a critical factor that affects fatigue strength. [20] In L-PBF components, the surface roughness is a complex function of the powder size, scanning rate, layer thickness, and many other process parameters. Regardless of parameters, the surface roughness of most of today's L-PBF AM components exceeds that of conventionally machined parts, [21] and as such, contributes to the components' lower fatigue strength. [22] It is thus an important consideration to evaluate the fatigue loading of L-PBF manufactured components, and address this problem by means of reducing surface roughness especially at loci where critical loads are found (fastener holes, stress concentrations, surfaces under cyclic tensile loading, etc.). [23] [24]

During any loading-unloading event which results in plastic deformation, a portion of the applied stress remains in the material in the form of residual stress. Residual stresses are often not desired, and are removed by a heat treatment process called stress-relief annealing. In some instances however, a compressive residual stress is deliberately induced at the surface of a component in order to enhance its performance. Residual stresses are never uniform throughout an entire object because of the requirement for the object to be in equilibrium. As an example, a component with high surface compressive residual stress will exhibit an energy-equivalent tensile residual stress along its depth. Figure 2.8 shows an example of the residual stress depth profile when the surface of a material is peened with an impact from a particle.

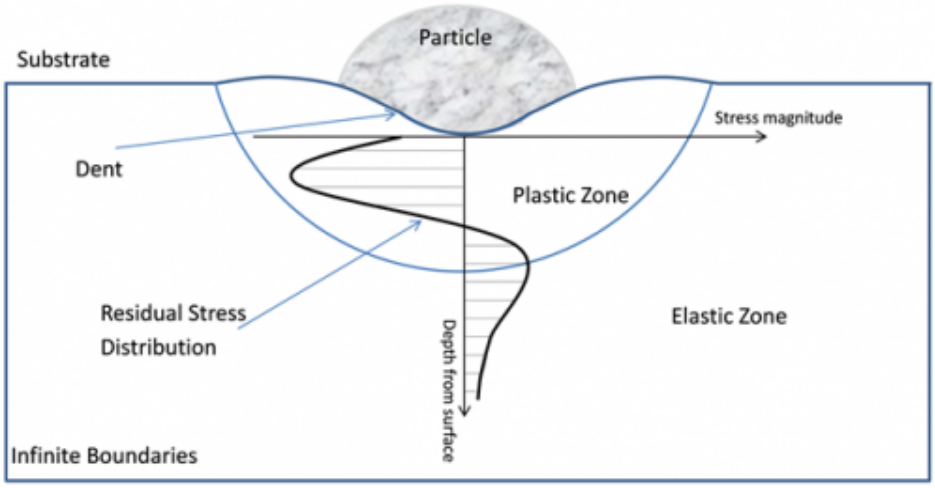


Figure 2.8: Shot Peening Residual Stress [25]

Figure 2.9 shows a simplified representation of the affected region in Figure 2.8 before and after a typical shot peening process. In the image on the left, the stress field is in a relaxed state. The image to the right shows how the stress field changes as plastic deformation takes place. The lattice spacing closer to the surface is smaller, which means it is in a state of compressive residual stress. [25] The region at the bottom of the lattice has not been plastically deformed however the plastic deformation from above is forcing the lattice spacing to increase, making the stress field in this region tensile. Note that the depth profile plot of stress in Figure 2.8 corresponds to the horizontal lattice spacing in Figure 2.9.

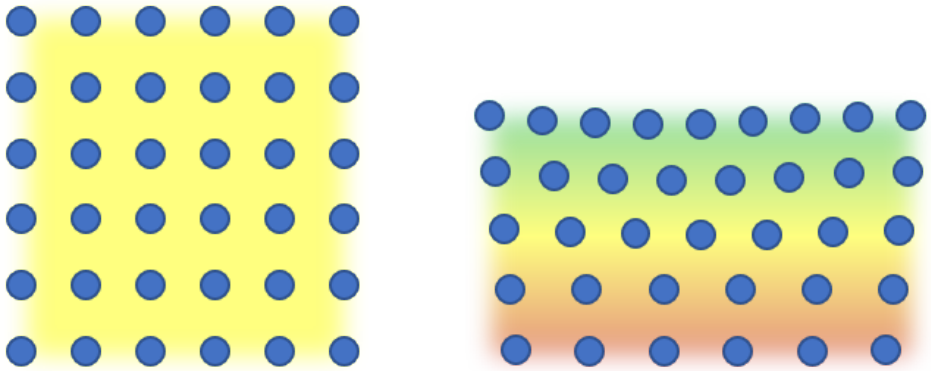


Figure 2.9: Residual Stress Simplified

Residual stresses originating from cold working change the ability of a part to carry load. A compressive residual stress at the surface of a stress-critical region of a component could be highly beneficial to the mechanical properties of that region, since any existing flaw/crack on the surface that could ultimately lead to fatigue failure is kept from growing and propagating into the material bulk. This is because of the principle of superposition of stresses. A tensile stress applied to a region which is already in tensile residual stress, results in a sum of the residual and applied stresses. If the stored residual stress is compressive in nature, the region can withstand a higher than normal tensile loading since the vector sum results in stresses partly cancelling out.

With the mechanics of fatigue failure in mind, one can start to appreciate the beneficial effect of the aforementioned superposition behaviour. Figure 2.10 shows a simple bending scenario where LSP has been used to treat the surface. The Z axis denotes depth below the surface. The plot on the left describes the stress state of a basic cross section (no residual stress), under a simple bending load. It is clear that the surface would experience the highest tensile stress, and since most cracking and fatigue failure originates from the surface of materials, this stress scenario under cyclic loading could lead to fatigue failure.

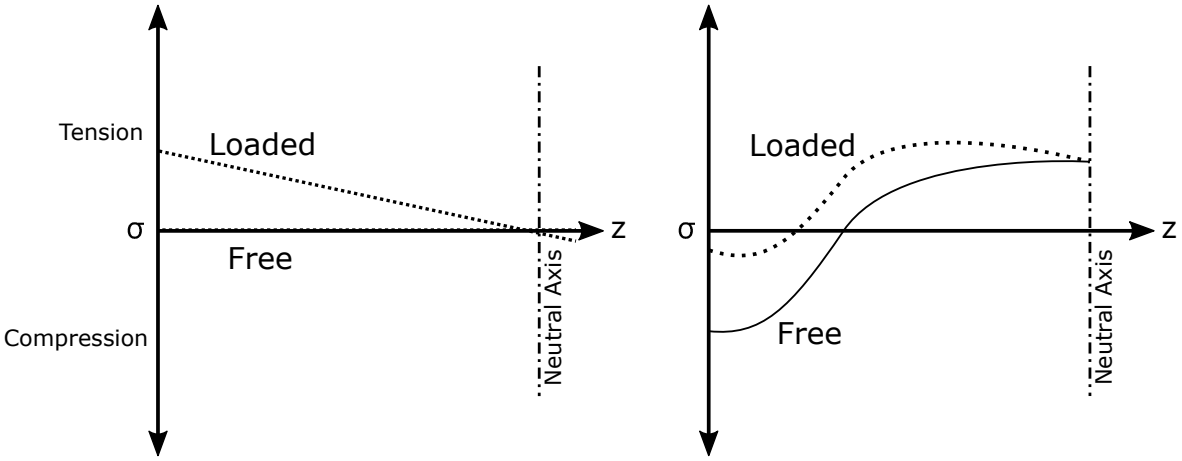


Figure 2.10: Compressive Residual Stress Benefit

The plot on the right shows the same geometry under the same loading, but with the pre-loading of a surface compressive residual stress. The benefit of this residual stress is realised when observing the surface stress state under loading. In this case the magnitude of the applied load is small enough that the surface of the component is still experiencing a net compressive stress. If one were to imagine the load increasing such that the surface experiences a net tensile stress, it would be clear that the magnitude of this net tensile stress would be far lower than what would be experienced without having the benefit of the compressive residual stress.

2.3 Titanium Alloy (Ti-6Al-4V)

2.3.1 Overview

Ti-6Al-4V is a widely used alpha-beta alloy of titanium which exhibits an excellent combination of toughness, strength, density and formability - all desirable properties for highly specialised applications. [26] In the aerospace field, titanium and its alloys have been used extensively for decades. The use of titanium in aircraft structures and engines reduces the overall weight, and results in a lower fuel consumption per flight. [27] It is also extremely corrosion resistant, non-toxic, and bio-compatible, making it a popular choice of material for biomedical applications such as prostheses and implants. Furthermore, the layer of oxide found on the surface is stable, provides protection to the metal below, and facilitates osseointegration. [28]

2.3.2 Phases and Alloying

In their solid state, titanium atoms can align in one of two arrangements:

- α -phase (hexagonal close-packed crystalline structure)
- β -phase (body-centered cubic crystalline structure)

In its pure form, titanium has an alpha to beta transformation temperature of 883 °C. In Ti-6Al-4V , the alpha and beta phases are stabilised using aluminium and vanadium respectively. Aluminium as an alloying element bears high importance, since it acts as a strengthener without compromising ductility of the alloy. Final mechanical working and heat treatments of Ti-6Al-4V are generally conducted below the beta transus temperature in order to achieve the desired microstructural phase distribution and grain size.

2.3.3 Titanium Beneficiation Program in South Africa

A partnership has been formalised in 2013 between Boeing and the Council for Scientific and Industrial Research (CSIR) in the form of the Titanium Beneficiation Cooperative Research Plan. The collaboration aims to develop ways of incorporating use of titanium powder into new products and manufacturing processes. This plan, coupled with South Africa's rich titanium ore reserves (second largest in the world), will support the nation's long-term goals with regards to economic development in the titanium sector. The CSIR has already developed and patented an innovative process of converting titanium tetrachloride to titanium powder. [29]

2.4 Laser Shock Peening

Laser Shock Peening (LSP) is a method of surface treatment which utilises the high-power energy delivered by a laser to change the material properties of materials such as metals and ceramics. Figure 2.11 is a diagrammatic representation of the LSP Process. A laser is aimed at a material's surface, where the target region is confined by a transparent medium (usually water). An extremely short but high power laser pulse arrives at the surface of the material, creating a rapidly expanding plasma.

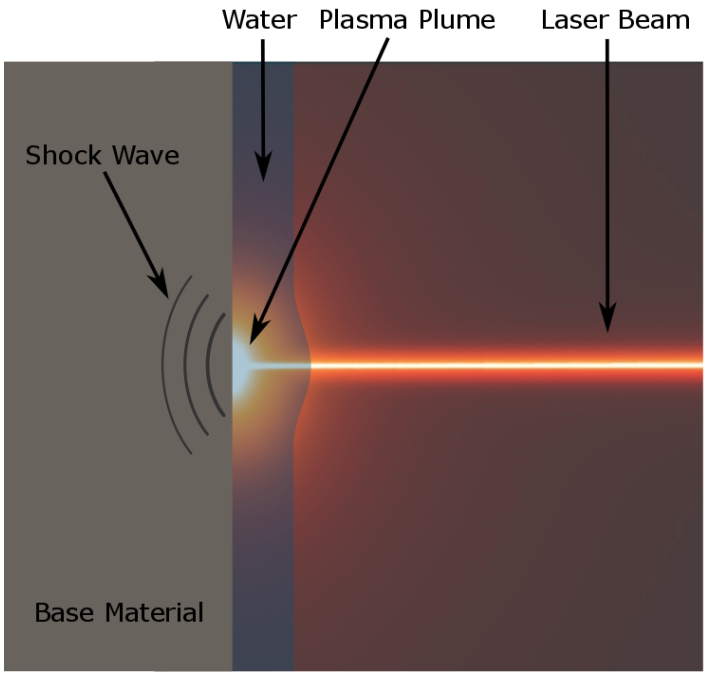


Figure 2.11: LSP Diagram

The confinement medium confines the expanding plasma and in doing so, amplifies the pressure pulse resulting in a strong compression shock wave being driven into the material. The confinement medium must be transparent to the laser and must also conform tightly to the surface of the part being processed. [30] Laminar flow of deionised water is the most common confinement medium used. [31]

2.4.1 Laser Shock Peening System Parameters

Although LSP is a relatively novel technology, the process is found in many variants of systems around the world. A few parameters that vary from system to system are as follows:

- Laser Type
- Laser Power
- Wavelength
- Pulse (energy, duration, size, shape)
- Spot Overlap/Coverage Density
- Confinement Medium (laminar flow of water/submerged).

- Ablative layer (Coating/No Coating)

These parameters ultimately determine the extent of peening action imparted on the material being processed. The parameters that can be adjusted on a LSP system (laser power, pulse duration, pulse size, pattern and coverage) ultimately determine the extent of plastic deformation, and hence the magnitude and depth of the resulting compressive residual stress in the material. Power, duration and spot size determine the intensity of the peening imparted with each shot, while coverage and pattern determine the effective number of shots any point on the surface receives and the anisotropy of the resulting stresses. [32] [33]

2.4.2 Effects of Laser Shock Peening

2.4.2.1 Residual Stress

As the shock wave travels into the depth of the material, the pressure exceeds the material's Hugoniot Elastic Limit (HEL). The result of this is that a Poisson stretching occurs in the plane normal to the direction of shock wave propagation and results in permanent plastic deformation outward. When the plastic deformation is complete, the spring-back effect (from the undeformed material) leaves the deformed material in a permanent state of compression [34]. Any compression resulting from deformation is always statically balanced by tension elsewhere in the material, and this typically occurs deeper than the compressive region. [35] It has been shown that LSP is capable of attaining higher depths and magnitudes of compressive residual stress when compared to Shot Peening (SP) - a method of peening a surface using high velocity impact from metal shot. [36]

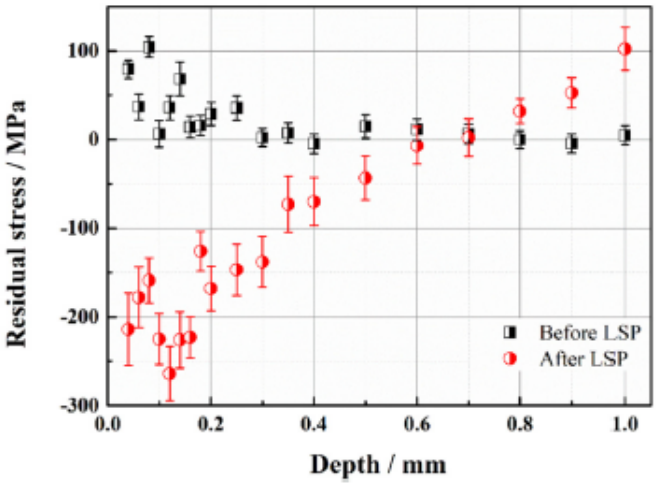


Figure 2.12: Residual Stress Before and After LSP [37]

Figure 2.12 shows the residual stress along the depth of AM Ti-6Al-4V processed by LSP in a paper by Guo et al. [37]

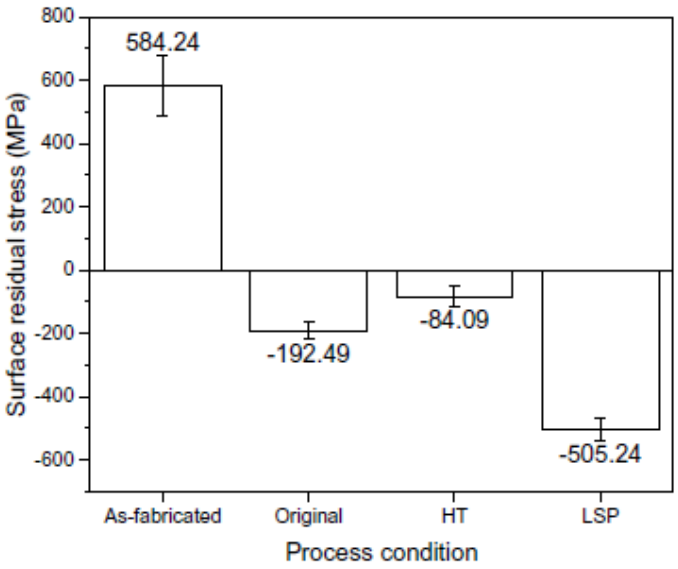


Figure 2.13: Residual Stress at Various Process Conditions [38]

Figure 2.13 shows the surface residual stresses of Ti-6Al-4V material at various process conditions. It shows that as-built Ti-6Al-4V has a tensile residual stress of 584 MPa. When the material is machined and heat treated, the residual stress was compressive at 84 MPa. LSP resulted in a compressive residual stress up to 505 MPa. [38]

It is important here to note that LSP has different outcomes with regards to compressive residual stress and depth depending on the nature and magnitude of the residual stress in the material before LSP processing (for AM this would typically be the difference between as-built and heat treated).

The compressive residual stresses induced by LSP have been shown to be beneficial across a wide range of applications in increasing overall fatigue life, reducing the rate of propagation of fatigue cracks and reducing propensity for stress corrosion cracking. Typical applications include the treatment of turbine blades in aircraft engines and in power generation to extend their useful service life and treating aircraft skins (especially regions around fastener holes) to reduce susceptibility to catastrophic fatigue failure. [27]

2.4.2.2 Deformation

One potentially adverse effect of LSP is that due to a change in the stress field of a component, an appreciable deformation could result depending on the geometry, location, and sequence of processing. Although this phenomenon can cause undesirable consequences, LSP has (in some cases) been leveraged for this very effect:

1. In the selection/calibration of LSP process parameters and approximation of residual stress through the deflection-based Almen method. An Almen strip is a low-stress rectangular coupon of metal thin enough to undergo an appreciable deformation when undergoing a surface peening process. The flat strip will permanently deform into an arc, whose height can give a measure of the energy imparted upon the sample during the peening process. This process is typically used to determine or verify appropriate LSP process parameters for a particular material. [39]
2. In the forming process of aerospace sheet metal. This forming method is unique because it induces curvature on a sheet by creating a compressive residual stress on both surfaces but of varying magnitudes. A conventional bending of sheet metal will always result in one surface having tension after spring-back. [40]

2.4.2.3 Surface Roughness

When LSP is applied directly on the surface of a material, there is an ablative effect from the high temperatures and pressures caused by the plasma expansion and subsequent bubble collapse cavitation effects. To reduce this ablative effect and increase the energy absorption, a dark sacrificial layer is applied to the surface before LSP. This is referred to as an ablative layer, since its purpose is to partially ablate, and leave the surface of the material unaffected by the thermal effects of the plasma.

LSP is typically known to increase surface roughness when performed without a coating on machined/polished material. However, given the typical surface roughness of as-built L-PBF components, it was expected that this may not necessarily be the case for LSP on as-built L-PBF material. Coverage/overlap is a strong factor influencing surface roughness induced by LSP, since it directly determines the frequency of the regular pattern an LSP shot leaves behind in the surface. [41]

2.4.2.4 Microhardness

LSP causes shock waves whose load exceeds the yield strength of a material. This plastic deformation causes an increase in dislocation density and results in the material undergoing strain-hardening, increasing the hardness of the material.

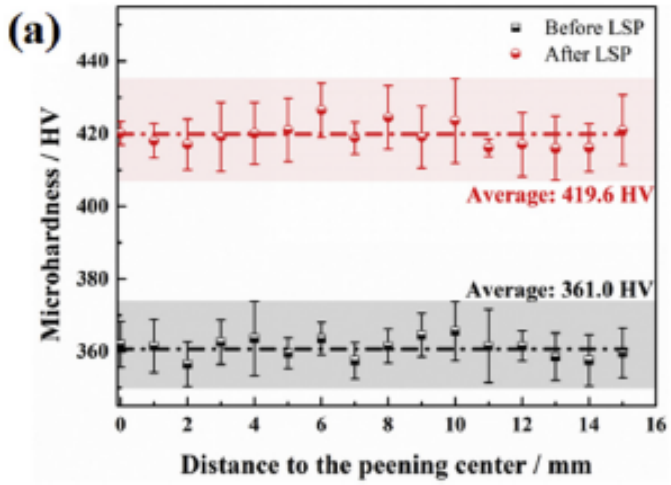


Figure 2.14: Microhardness Before and After LSP [37]

Figure 2.14 shows the comparison of microhardness in AM Ti-6Al-4V before and after LSP. [37] In this case the microhardness increased from approximately 360 HV to 420 HV.

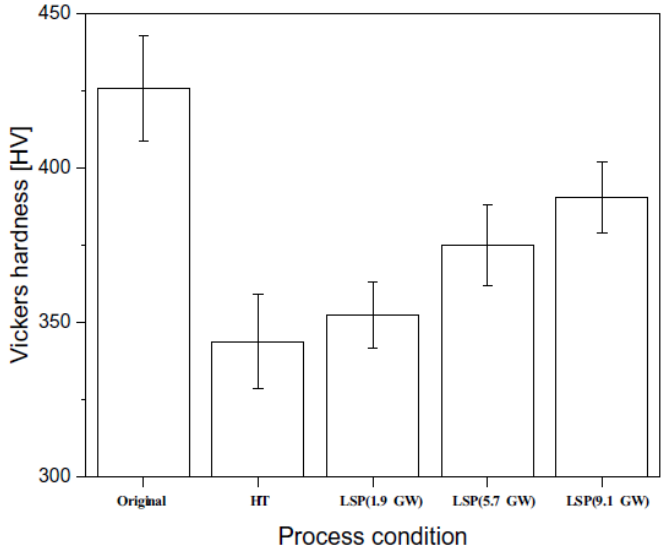


Figure 2.15: Microhardness at Various Process Conditions and LSP Laser Power [38]

Figure 2.15 shows the comparison of microhardness in AM Ti-6Al-4V in various process conditions (As-built, heat treated, LSP). [38] The microhardness of the as-built Ti-6Al-4V material is approximately 425 HV. The material was then heat treated, reducing the microhardness to approximately 345 HV, and then LSP was performed with varying laser power, increasing the hardness to a max value of 385 HV.

These examples show that regardless of prior condition (As-built or heat treated), the microhardness of a material increases after LSP.

2.5 Residual Stress Measurement

2.5.1 Incremental Hole Drilling

If one machines a small amount of metal from the surface of a cold-worked part, material is removed which contained residual stresses and contributed to an overall stress balance in the part. To restore the balance, the surrounding bulk must distort. [42]

In order to determine the depth profile of residual stress in the samples, a semi-destructive strain measurement technique was employed. Incremental Hole Drilling (IHD) uses specialised strain gauge rosettes and operates on the aforementioned principle of incremental removal of stressed material, allowing the surrounding stressed material to attain a new equilibrium with each step. These measured strains are then used in conjunction with Finite Element Analysis (FEA) determined calibration coefficients to determine the stresses under the assumption of elastic deformation. Figure 2.16 shows the configuration and the strain gauge used in the IHD process.

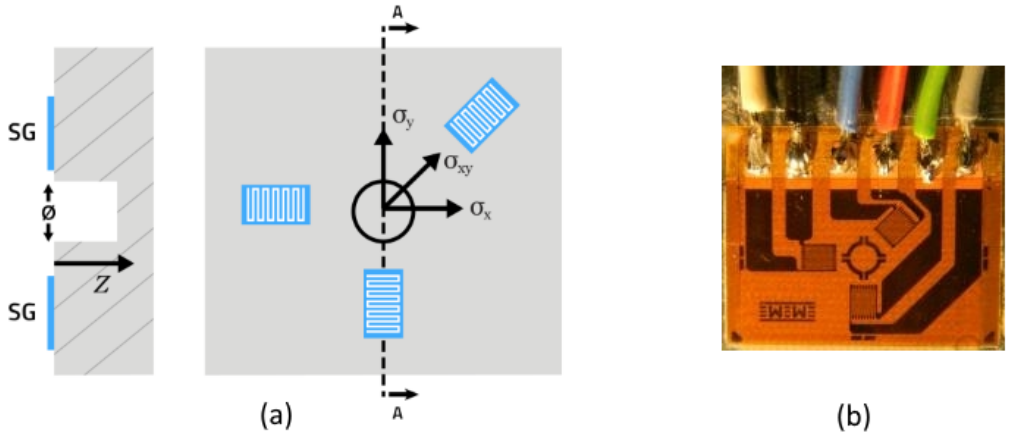


Figure 2.16: IHD Diagram (a) and ASTM Type A Strain Gauge Rosette (b)

The rosette (b) consists of three gauges which radiate from the centre point and the end mill is aligned with the cross-hair. An inverted conical tungsten carbide end mill is used with a compressed air turbine at a high speed and low feed rate to minimise heat build-up and expansion of bulk material during drilling. A further precaution against expansion is a feature called *acquisition delay* which takes the strain readings with a delay after each drilling increment.

2.5.2 Diffraction-Based Methods

Some residual stress measurement techniques use the principle diffraction to determine the inter-planar spacing of the atoms that make up a crystal lattice. This spacing can then be used to determine the strain in the material, and hence the residual stress that it contains. Diffraction methods are all non-destructive, and include Laboratory X-Ray Diffraction, Synchrotron X-Ray Diffraction, and Neutron Diffraction.

A crystal lattice is an arrangement of atoms in a regular structure, which can be described by values called Miller indices. These values define which directions the lattice planes lie in. The spacing between two adjacent planes is called the inter-planar spacing or d-spacing. [18]

The principle of diffraction is explained using the diagram in Figure 2.17. A beam, incident at a certain angle to parallel lattice planes gets diffracted, and a pattern is formed due to interference. Constructive interference occurs at angles where Bragg's law is satisfied. These angles are used to calculate the d-spacing between the lattice planes. [43]

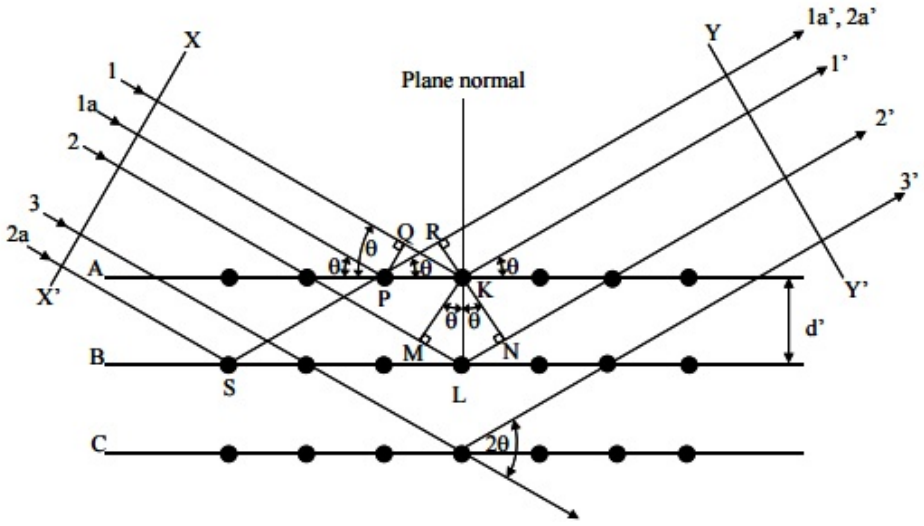


Figure 2.17: Diffraction Theory [43]

2.5.2.1 Laboratory X-Ray Diffraction

Laboratory X-Ray Diffraction uses the aforementioned principle to measure stresses to depths of 8 to 30 µm at a resolution of 10 µm to 1 mm. So called owing to its compact size, Laboratory X-Ray Diffraction apparatus typically fits on a tabletop in a laboratory and is found at a broad range of academic, research and industrial institutions. [44]

2.5.2.2 Synchrotron X-Ray Diffraction

Synchrotron X-Ray Diffraction works on the same principles as X-Ray Diffraction but with a much higher energy delivery. Depths of stress measurement with synchrotrons ranges from 10 µm to 60 mm with resolution ranging from 1 µm to 1 mm. There are very few synchrotron facilities around the world, and the use thereof is expensive. This makes Synchrotron X-Ray Diffraction a less practical method of residual stress measurement, however it does provide a nature of measurement that other techniques cannot match. [45]

2.5.2.3 Neutron Diffraction

This technique employs a source of neutrons (typically a nuclear reactor) as the beam, and much like with X-Rays, diffraction of neutrons follows Bragg's Law and the strain (and associated stress) is determined by using the diffraction angle peaks. Neutron Diffraction provides residual stress measurements with resolutions of 100 µm to 10 mm and to much greater depths (1 mm to 100 mm) than X-Ray Diffraction methods. [46]

This research project employed Laboratory X-Ray Diffraction and Incremental Hole Drilling as complementary techniques by which to measure residual stresses.

2.6 Objectives

Upon reviewing the literature of the fields of LSP and AM, it was decided that a significant contribution to the furthering of knowledge in both fields would be established by performing LSP on AM Ti-6Al-4V .

If successful, the compressive residual stress benefits from LSP treatment would directly address the negative stress effects of the AM process. As mentioned in the literature review,

LSP is known to increase surface roughness on a smooth aluminium plate, however the surface roughness on as-built AM Ti-6Al-4V could be such that LSP might actually reduce it.

With these considerations in mind, the following is a list of the primary objectives of the research project in alignment with the requirements of the University of the Witwatersrand and the CRPM:

- To determine whether LSP can be effective in inducing a beneficial compressive residual stress of sufficient depth and magnitude in AM Ti-6Al-4V
- To determine the effect of the LSP process on the surface roughness of AM Ti-6Al-4V
- To determine the microstructural and surface morphological changes induced by performing LSP on as-built AM Ti-6Al-4V

3 Methods and Experimental Setup

This chapter serves to describe, in detail, the design of the experiment for this research project. The sections included below are in order of experimental steps, including manufacture of samples, processing of samples, and all the subsequent measurements, tests and observations keeping destructive/non-destructive nature of processes in mind.

3.1 Laser Powder Bed Fusion

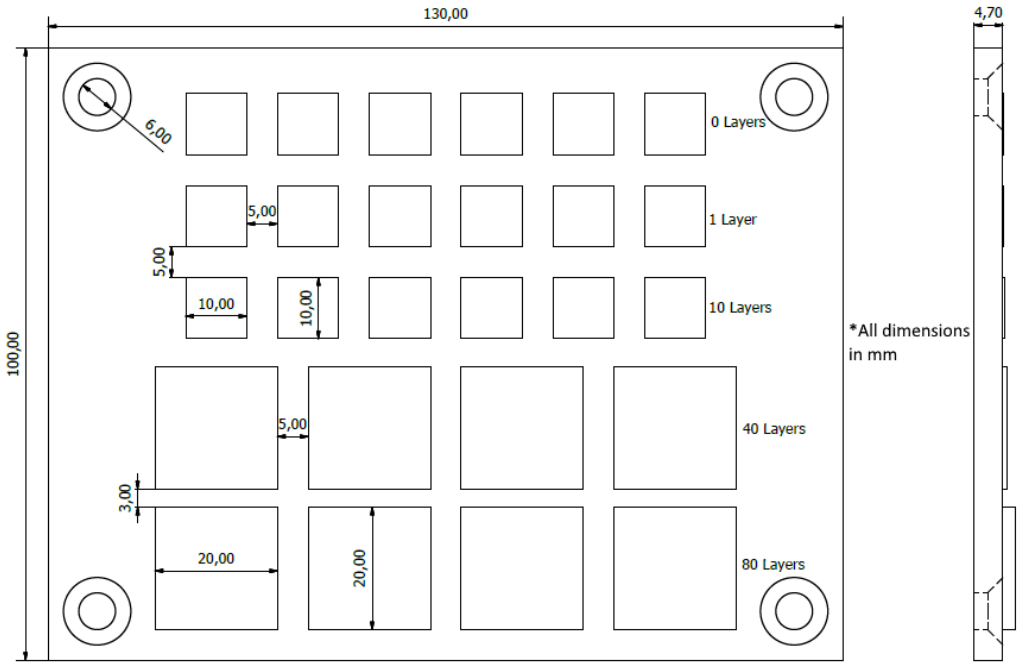


Figure 3.1: Planned Sample Array

As shown in Figure 3.1, an array of 26 square sample prints on a 5mm thick Ti-6Al-4V substrate base plate were planned of varying thickness and two area sizes.

18 Small samples (10 mm x 10 mm) were to be used for the purpose of measuring stress using X-Ray Diffraction, which only measures the very surface state of residual stress. The small samples were to be 0 layers (no powder), 1 layer and 10 layers high, where each layer is 30 m. These samples are labelled numerically.

8 Large samples (20 mm x 20 mm) were planned for the purposes of IHD stress measurement (depth profiling), and are of appropriate dimensions for performing IHD (Area sufficient for mounting strain gauge rosettes and height sufficient for drilling). These large samples were to be 40 layers and 80 layers high. These samples are labelled alphabetically.

The samples were to be left on their base plate, and in their as-built state to explore the detrimental tensile residual stresses inherent in the L-PBF process, and the ability of LSP to reverse these.

3.1.1 Apparatus

The L-PBF machine used to print the sample array was an EOSINT M280 by EOS GmbH. Manufacturing was done at the Centre for Rapid Prototyping and Manufacturing at the Central University of Technology (Bloemfontein).



Figure 3.2: EOSINT M280 L-PBF Machine [47]

3.1.2 Process Parameters

The process parameters, as recommended by Prof. Igor Yadroitsev (Central University of Technology) for the geometry and material in question, were as follows:

Laser Power	170 W
Scanning Speed	1.2 m/s
Spot Size	80 µm
Layer Thickness	30 µm
Hatch Distance	100 µm
Scanning Strategy	Back-and-forth (Zig Zag)
Protective Gas	Argon

Table 3.1: L-PBF Process Parameters

3.2 Laser Shock Peening

Both large and small sample groups would be subdivided, where one half of the samples were to be treated with LSP to induce beneficial compressive residual stresses near the surface, and the other half left in their as-built state. Appropriate LSP parameters such as spot size, overlap, pulse energy, pulse duration, etc. would be determined from a deflection based method (Almen Strips Approach).

It should be noted that for this research, the samples would be processed by LSP without coating and with a high overlap/coverage in order to determine the effect this has on the high surface roughness on the as-built AM surface.

3.2.1 Method

In order to determine appropriate LSP process parameters for the AM Ti-6Al-4V samples, an Almen strips (deflection coupons) approach was utilised. By Prof. Igor Yadroitsev's recommendation (to use the same parameters used for processing wrought Ti-6Al-4V), the spot overlap/coverage and power intensity were optimised by tests performed on wrought Ti-6Al-4V Almen strips laser cut from a stock plate. The standard dimensions of the coupons were 19.05 mm by 76.2 mm, at a thickness of 1.2 mm. It was found that an energy per pulse of 0.265 J, a spot size of 0.8 mm at a coverage of 40 spots per mm resulted in an appropriate Almen intensity (extent of arching of samples) to be used as process parameters for this material.

With the LSP parameters established, half of the sample array was processed by LSP (without coating) as follows.

Sample array was mounted on the 3-axis CNC stage, and the focal plane was located. The alignment laser was placed on the corner of the first sample square, and a peening grid was

programmed into the CNC control software. The water (confinement medium) nozzle was positioned and the flow rate adjusted to ensure uniform and laminar flow along the target area, and the energy of the laser pulse checked.

3.2.2 Process Parameters

The samples were processed as per the following:

Laser	CSIR NLC - Nd:YAG (Yttrium-Aluminum Garnet)
Energy per pulse	0.265 J
Wavelength	1064 nm
Pulse Frequency	20 Hz
Power Density	8 GW/cm^2
Spot size	0.8 mm
Coverage	40 spots/mm^2
Pattern	Raster (Scanning and Stepping)

Table 3.2: LSP Process Parameters



Figure 3.3: LSP

3.3 Surface Roughness

Measurement using a digital surface roughness probe would be done to establish the difference in surface roughness values between as-built samples and LSP treated samples. R_a and R_z

values will be measured for a range of locations on several samples, and averages will be taken of these readings.

High surface roughness is a well-documented consequence of powder bed fusion, and is a direct function of the process parameters of the L-PBF machine and the angle of the measured surface in relation to the build direction. Two surface roughness values were of interest in this measurement:

- R_a - Arithmetical mean deviation along the sampling length profile
- R_z - Distance between highest peak to lowest valley

Surface roughness measurements were taken along the top of the sample squares using a SRM-PS1 mechanical probe scanner by Chris-Marine (Figure 3.4).



Figure 3.4: SR Measurement Device PS1

3.3.1 Method

Sample array was placed on a level surface and the SR measurement device placed on top, with the probe aligned to the upper third of a sample square. The start buttons on either side of the device were pressed and the device was left to scan a 5 mm length of the sample surface. Three measurements were taken on different locations on the sample for averaging. The process was repeated for samples of thickness 0, 1, 10 and 40 layers.

3.4 X-Ray Diffraction

Laboratory XRD technique was employed to accurately measure the surface stress state of the samples. XRD (especially Laboratory XRD) does not have the ability to resolve stress along the depth of a part, so its measurements should be interpreted as the stress state in the final L-PBF layer.

3.4.1 Method

The Proto iXRD machine at the CSIR NLC was used to perform XRD measurement (Figure 3.5).



Figure 3.5: Proto iXRD [48]

The following are the details of the XRD process used:

X-Ray Source	Cu K Alpha (1.5418 Å)
Phi angles	0°45°90°
HKL	{213}
Aperture size	2 mm
Bragg angle	142°
X-ray elastic constants	same as wrought Ti-6Al-4V
Goniometer range	+- 20°, 3°oscillation
Measurement angles per sample	7
Exposure time	4 sec
Number of exposures	20

Table 3.3: XRD Process Parameters

3.5 Incremental Hole Drilling

IHD measurement was performed to determine the nature of the residual stress depth profile. This technique does not give reliable measurements near the surface so the near surface measurements from IHD should be interpreted with great care.

3.5.1 Method

A SINT Restan MTS3000 system (Figure 3.6) at the Wits School of Mechanical, Industrial and Aeronautical Engineering lab was used to perform incremental hole drilling. It is a fully automatic device which performs drilling increments and strain data acquisition. Procedures were followed as per the ASTM E837-01 standard (Appendix C).



Figure 3.6: Restan MTS3000 [49]

3.5.1.1 Mounting Strain Gauge

Perhaps the most critical aspect of successful IHD is reliably mounting the strain gauge on the material being measured. Without proper bonding, the strain gauge will not reflect true strains as experienced by the surface of the material and will result in bad data. The process of mounting the ASTM type A strain gauge rosette involved the following steps:

1. Surface is gently ground with fine grit silicon carbide paper.
2. Surface is degreased using acetone spray and wiped clean.
3. Conditioner is applied to the surface and wiped away.
4. Neutraliser is applied to the surface and wiped away.
5. The strain gauge is placed on the surface.
6. Strain gauge tape is used to temporarily secure the strain gauge in its final position.
7. The tape is pulled back partially and strain gauge lifted, and a coat of catalyst is brushed onto the gauge.
8. After a minute, two drops of M-Bond Adhesive is applied to the surface and the strain gauge is pressed down for three minutes.
9. The tape is removed with a low angle relative to the surface to minimise the normal component of force on the gauge.

3.5.1.2 Wiring

The strain gauge is connected to the data acquisition device (DAQ) following these steps:

1. The solder terminals on the gauge are roughened with an abrasive pen, and cleaned with a flux pen.
2. Small domes of solder are added onto each terminal.
3. The wires are placed onto each dome, and soldered on.
4. The resistances are checked using a multimeter, verifying that the electrical connections are adequate.
5. The stability and repeatability of strain measurements is checked on the computer, verifying that the bonding is secure.

3.5.1.3 Alignment and Positioning

Before the automated drilling process begins, one needs to ensure that the end mill is concentric with the gauge, the drilling is level and that the drilling starts on the true surface of the material. The following steps were taken to ensure this:

1. IHD device is aligned with the centre of the strain gauge by eye.
2. Circular spirit level is used to ensure that drilling is normal to the surface.
3. Fine X-Y adjustment is made using the scope to align cross-hairs of machine and gauge.
4. Drill is manually activated and lowered until a small amount of strain gauge material is removed.
5. Concentricity of the cut gauge material and gauge circle is verified with the scope.
6. Automatic surface detection (electrical contact) is used to zero the end mill on the surface of the metal.

3.5.1.4 Drilling

The ASTM E837-13 Ext Non-Uniform Standard was followed for the hole-drilling test.

The incremental drilling operation is fully automatic and was left to run, with regular check-ups on strain measurement values, and aural monitoring of turbine noise level and pitch. Upon completion it was important to take measurements of the size of the hole using the cross-hair, and determine the eccentricity.

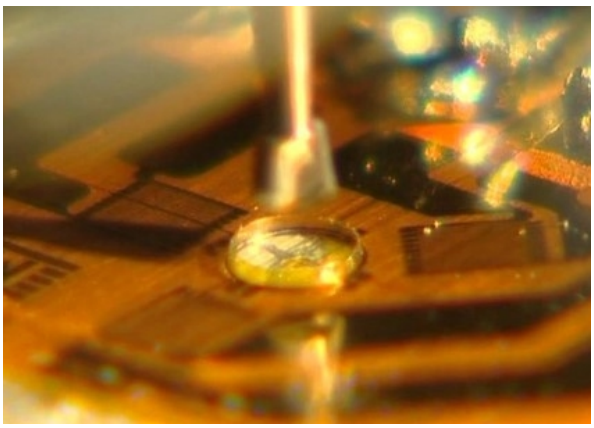


Figure 3.7: Drilling Process

3.5.1.5 Strain Data Processing

SINT Eval 7.12 software was used following the ASTM E837-13 Ext Non-Uniform standard in processing the strain and hole data in order to back-calculate the depth profile stress state. The stress results were given in 125 micrometer increments to a final depth of 0.975 mm.

3.6 Microhardness

The samples were sectioned in a vertical plane (normal to the top surface of the as-built samples). Regular microhardness measurements were measured along a vertical line on the cut face of the samples, to establish the depth profile of microhardness in a LSP treated sample and compare this to the microhardness values in as-built AM material. Microhardness of the wrought base plate was measured to use as a reference. A Vickers Hardness testing machine was used to take measurements. Microhardness is directly related to cold work and dislocation density so this would show how prevalent these phenomena are.

3.6.1 Method

Microhardness testing was performed on the samples at the Wits School of Mechanical, Industrial and Aeronautical Engineering laboratory using the Innovatest Falcon 500 machine. The machine uses a Vicker's Hardness method with a diamond indenter. The samples are positioned at the appropriate height using an objective lens, and their x-y position is adjusted using micrometer screw-gauges.

The machine was set-up with the following parameters:

- Indent force 200 g
- Dwell time 10 sec

A measurement was performed with the following steps:

- Position sample on stage underneath probe.
- Rotate the turret to the 50x mag objective lens.
- Using the micrometers, adjust sample to desired measurement position.
- Adjust the focus on the objective lens until the surface is perfectly focused.
- Click the measure button.
- Turret revolves to the microhardness indenter and performs an indent using the parameters as specified above.
- When indentation is complete, machine automatically rotates turret back to the objective lens, and a the edges of the indent are automatically located.

- The edge detection is verified visually, and the software calculates the microhardness value.
- These steps are repeated for each microhardness sampling location.

The recommended distance between indents was at least three indent diameters according to the best practice for microhardness testing. The distance between measurements was thus chosen to be 0.15 mm. Microhardness testing was done by taking three measurements per depth location and averaging the result out. Depth profiling was done on LSP AM and as-built AM cross sections, and was performed on the Ti-6Al-4V base plate as a reference.

3.7 Light Microscopy

Light microscopy would be performed on the samples for the purposes of a metallographic analysis. The samples would be cut along a vertical plane, mounted, etched and a comparison done between the microstructures of wrought, AM (as-built) as well as LSP processed AM regions of Ti-6Al-4V.

Samples were individually examined under light microscope, in order to determine the characteristics of sectioned microstructure. It was of particular importance to see the grain size and arrangement of AM Ti-6Al-4V compared to hot rolled Ti-6Al-4V plate, and the influence that LSP has on these characteristics. The metallographic sections were inspected using a stereo light microscope (Figure 3.8).



Figure 3.8: Stereo-Discovery-V8 Light Microscope [50]

3.7.1 Preparation

Micro-sections were prepared with the following procedure:

1. A low-speed diamond saw (Figure 3.9) was used to section samples along the plane of interest.
2. The cut samples were mounted in metallographic resin.
3. Grinding with silicon carbide paper (320 grit) (All grinding and polishing was done on a laboratory polishing machine seen in Figure 3.10).
4. Grinding with silicon carbide paper (1000 grit).
5. Primary polishing using a napped cloth and diamond suspension (6 µm).
6. Final polishing using a napped cloth and an attack polishing agent (80% Colloidal Silica 20% Hydrogen Peroxide).
7. Polished surface was swab-etched for 10 seconds using Kroll's Reagent.



Figure 3.9: Buehler IsoMet LS [51]



Figure 3.10: Struers LaboPol System [52]

3.8 Scanning Electron Microscopy

Scanning Electron Microscopy (SEM) analysis would be done on the samples to gain an appreciation of the surface morphology of AM material, and how LSP processing affects it.

SEM was performed on the samples using a Zeiss Sigma Scanning Electron Microscope (Figure 3.11) at the Wits School of Chemical and Metallurgical Engineering Laboratory. The microscope also features Energy Dispersive X-Ray (EDX) analysis which was used to determine the approximate chemical composition of the analysed region.



Figure 3.11: Zeiss Sigma SEM [53]

3.8.1 Method

The following steps were performed to capture an SEM image for each sample:

1. A sample is fixed on the sample holder using electrically conductive adhesive tape.
2. The sample holder is placed on the stage of the evacuation chamber.
3. Chamber is evacuated using a vacuum pump.
4. Stage position is adjusted until the region of interest is in the field of view.
5. Images using SE2, BSD and EDX are saved at various locations and magnifications.

These steps were performed for each sample loaded into the SEM. For multiple images from the same sample, only steps 4 and 5 were repeated.

4 Results and Discussion

4.1 Laser Powder Bed Fusion

The sample array was not stress relieved or heat treated after manufacture, and as such retained substantial tensile residual stresses in the printed material, which were observed to induce a slight curvature in the 5 mm base plate. Figure 4.1 shows the Ti-6Al-4V sample array as manufactured by the CRPM. Streaks were observed along the surface which aligned with the direction of the powder re-coater arm, and it was observed that there was a correlation between number of layers printed and surface finish quality.

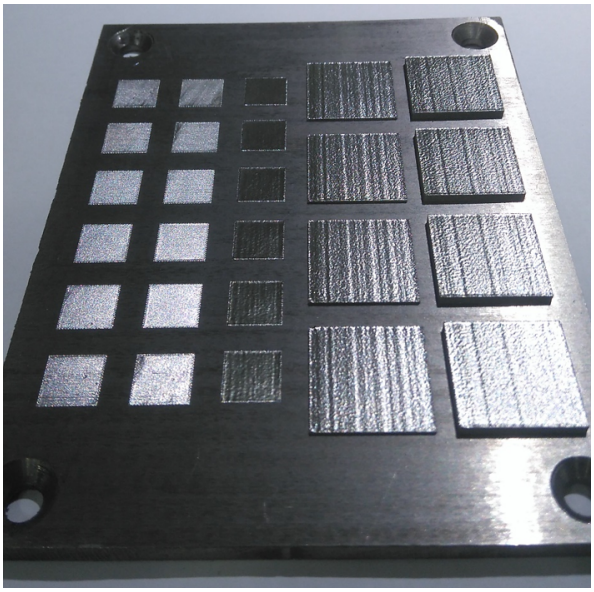


Figure 4.1: Printed Samples

The surface of the samples was inspected using a low magnification digital microscope (Figure 4.2), and the following observations were made:



Figure 4.2: Dino-Lite AM3111

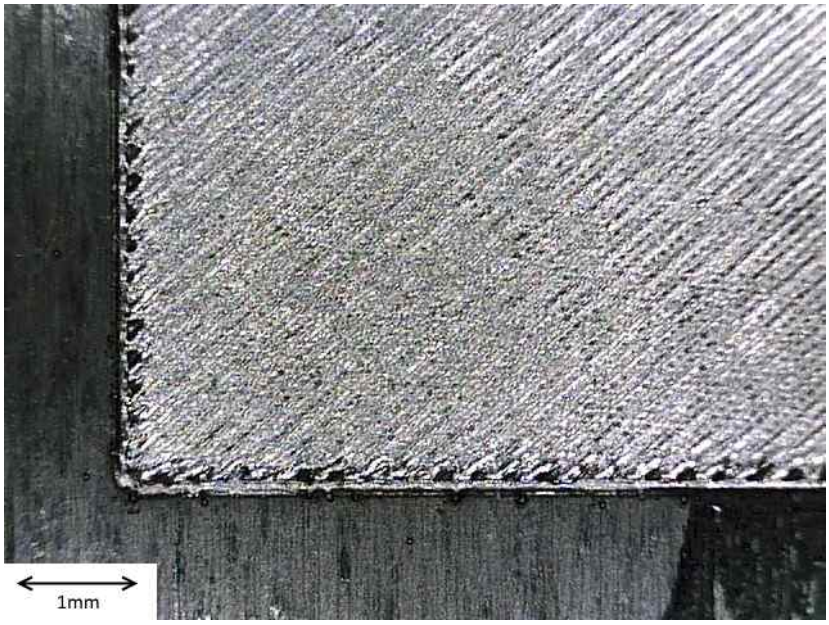


Figure 4.3: AM Surface (20X Magnification)

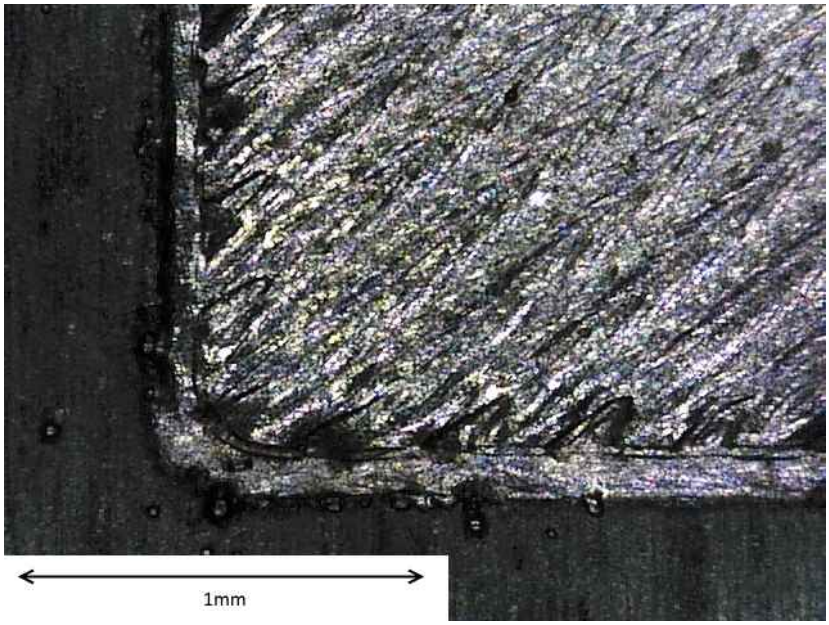


Figure 4.4: AM Surface (75X Magnification)

Figures 4.3 and 4.4 show the laser scanning direction at the angle set for the surface layer. The outline of a layer is also clearly visible, which is scanned first before the fill hatching. Small gaps are seen in the hatching near the outlines. Some spatter from the melting process is observed on the Ti-6Al-4V substrate plate near the sample square.

4.2 Laser Shock Peening

From initial observations, it was seen that the peened surface exhibited a matte black residue, and the location of the last LSP pulse had a relatively clean metallic centre surrounded by matte black residue.

The peened surface was inspected under a low magnification digital microscope which yielded the following images:



Figure 4.5: Peened Surface (20X Magnification)

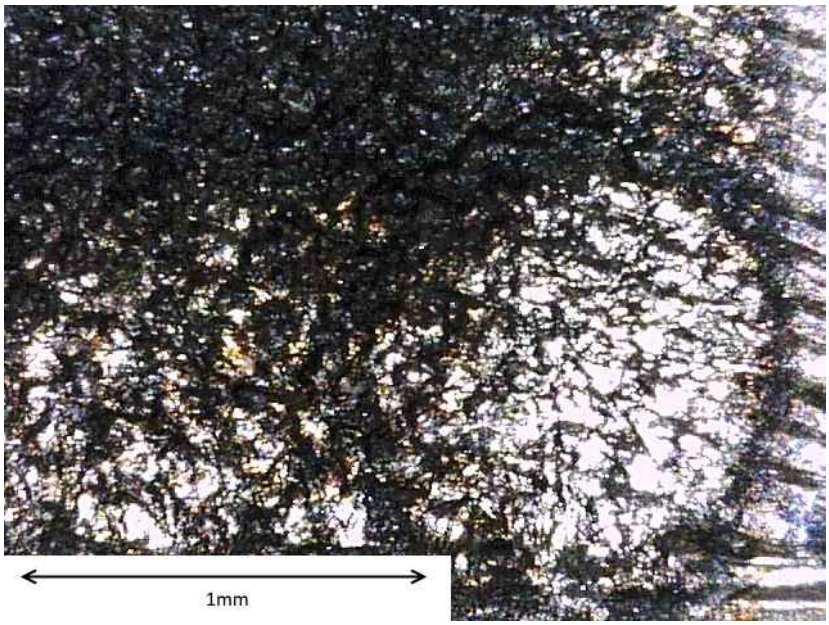


Figure 4.6: Peened Surface (75X Magnification)

Figures 4.5 and 4.6 show the surface after LSP. The most prominent characteristic is the black appearance, which is attributed to surface oxidation during the plasma formation phase of each pulse. It is interesting to note that this oxide only gets left behind in a ring shape after each pulse. This is evident in both images, where the dark patterns on the right and bottom edges of the peened area are not solid black, and the final pulse (bottom right) can be seen to contain a clean central area. The fact that the central region of the last pulse is clean also

suggests that the surface oxide layer is not strongly embedded and is purely superficial. This remains to be confirmed during a metallography section examination.

4.3 Surface Roughness

The following two graphs show the comparison between AM (as made) surface versus LSP (peened) surface for both R_a and R_z surface roughness values.

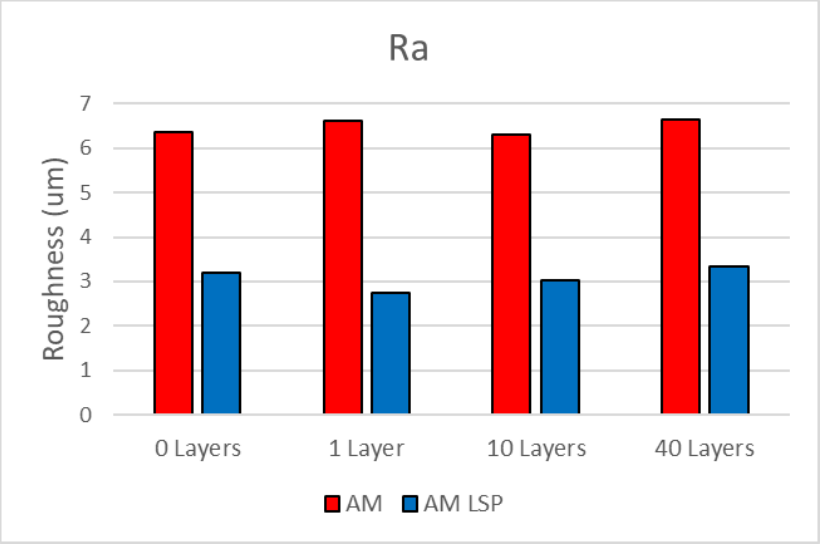


Figure 4.7: Surface Roughness Comparison (R_a)

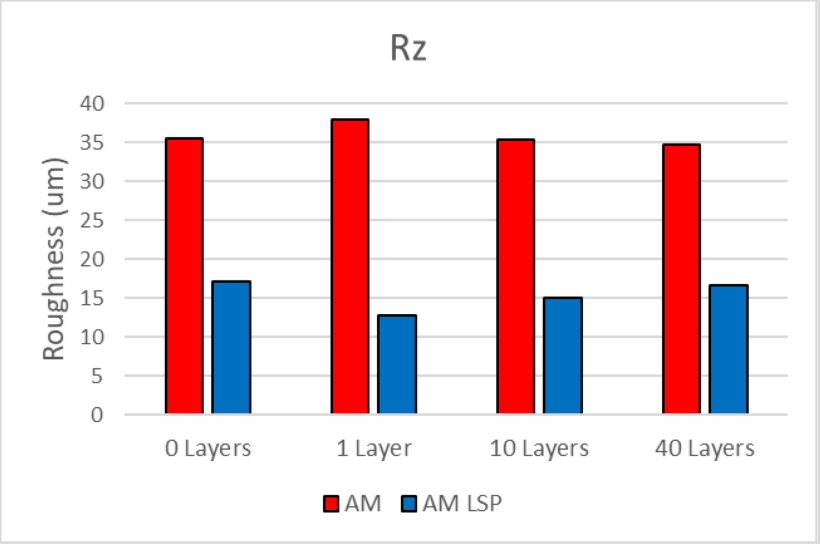


Figure 4.8: Surface Roughness Comparison (R_z)

It is of interest to note that after the LSP processing, both the roughness values R_a and R_z had at least halved in magnitude. This result implies that during the LSP pulse, larger plastic deformation was experienced by the peaks along the surface relief, ablating and flattening them and making both average and maximum peak-to-valley distance smaller. It must however be noted that the surface roughness measurements on peened samples may include the effect of the surface oxide layer whose roughness values may differ from the underlying metal.

4.4 X-Ray Diffraction

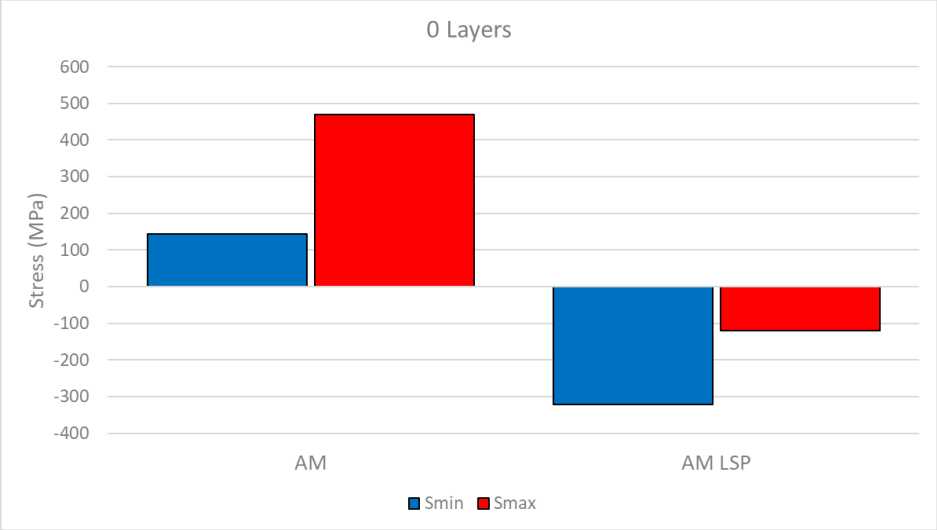


Figure 4.9: XRD 0 Layers

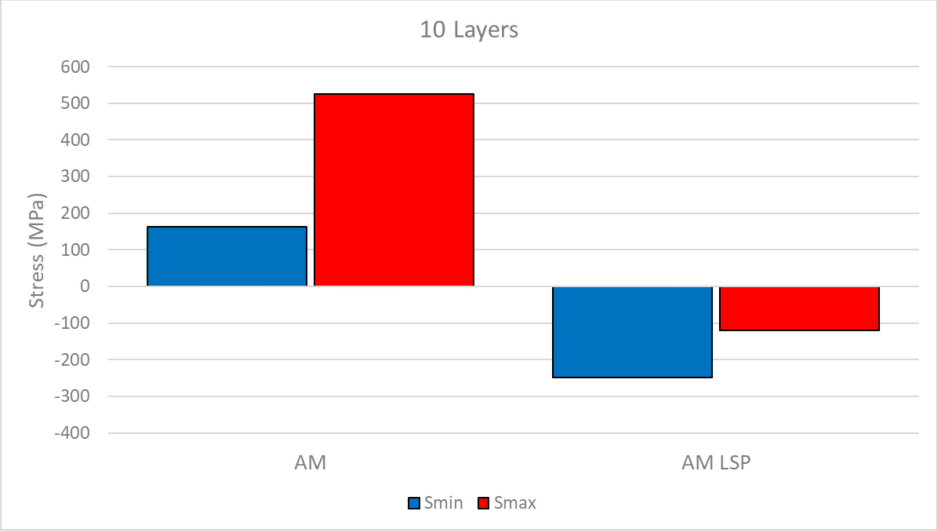


Figure 4.10: XRD 10 Layers

The trend seen in the results above, shows that for both 0 layers and 10 layers, the residual stress in the as-built state is highly tensile, in the range of 450-550 MPa S_{max}.

The large discrepancy between S_{min} and S_{max} indicates a highly anisotropic stress field across all the samples. This can be explained by considering the nature of the L-PBF process. A layer is melted by scanning in a zig-zag manner in a certain stepping direction. This means that melted material has directional cooling and as such develops an anisotropic stress when it is solidified and fully cooled. In the LSP processed samples, the anistropy can similarly be explained by the LSP process following a scanning and stepping strategy (raster pattern). This results in a highly directional stress field aligned with the orthogonal raster pattern. This is confirmed by observing beta angles of S_{max} and S_{min} in the raw data.

It is observed that the residual stress in the as-built samples is higher in the 10 layer samples than in the 0 layer samples. This could be attributed to the fact that the 0 layer sample only has one pass of a melting scan (no powder) over the base plate, and as such, only has itself, and a small depth below sitting in a highly tensile stress state. The 10 layer sample has more stressed AM material below the surface, which might result in the surface sitting at a slightly higher stress state than the 0 layer sample.

The difference in residual stress between the 0 layer and 10 layer LSP treated samples could also be explained by the state of the underlying material. In the 0 layers samples, the underlying material is relatively low-stress wrought titanium plate. Thus to perform cold work on this takes less total energy when compared to material in a highly tensile stress to begin with. Since each pulse delivers the same amount of energy, the 0 layers sample attained a higher state of compressive residual stress than the 10 layers sample.

4.5 Incremental Hole Drilling

The back-calculated S_{min} and S_{max} depth profile is seen in the following graphs, where two samples in each group are labelled 1 and 2. These graphs show results for both 80 layer and 40 layer thick samples.

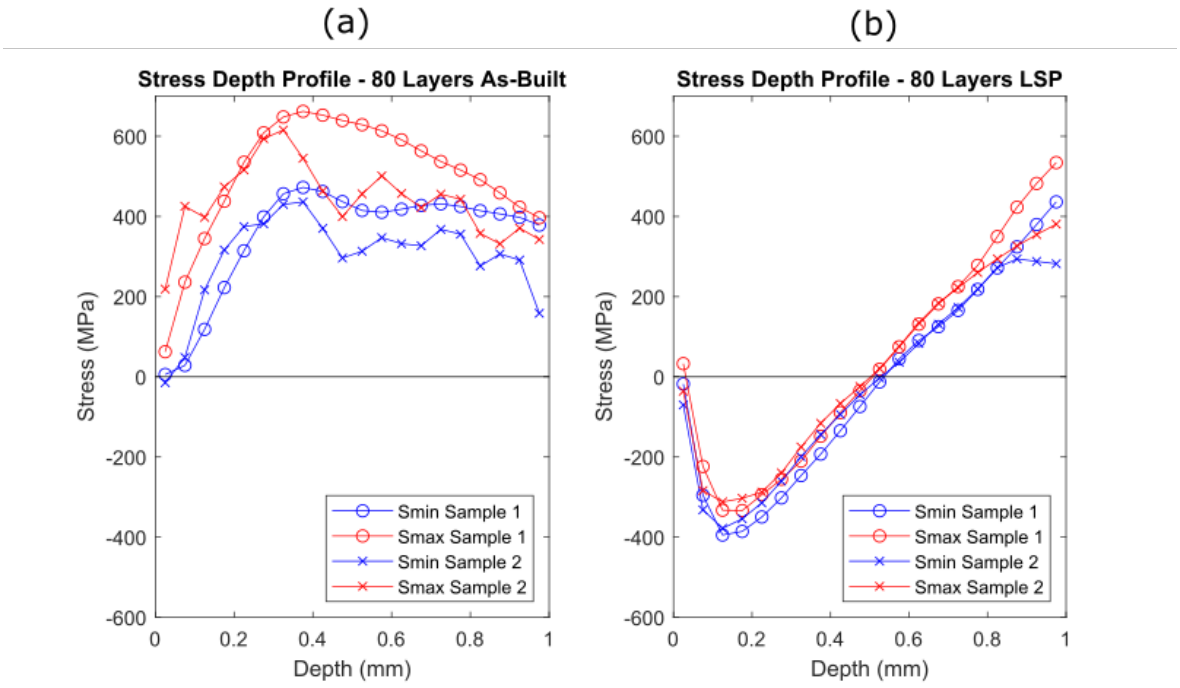


Figure 4.11: Residual Stress Comparison in 80 Layer As-Built (a) and LSP (b) Samples

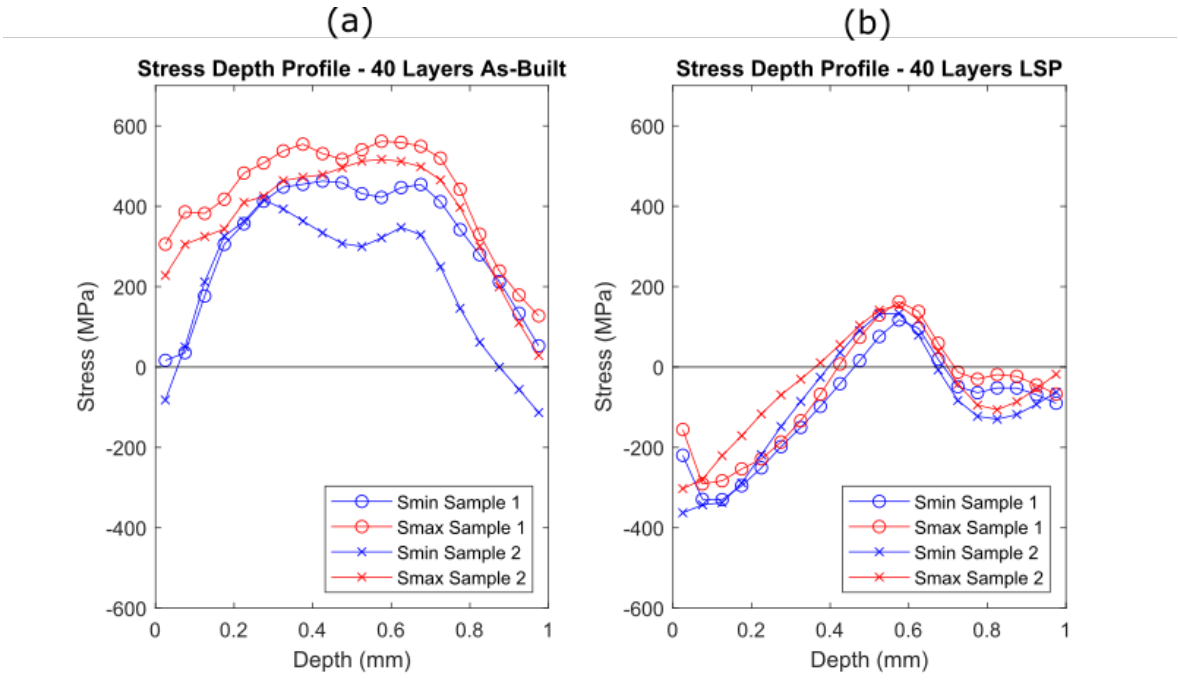


Figure 4.12: Residual Stress Comparison in 40 Layer As-Built (a) and LSP (b) Samples

In Figure 4.11 (a), it is seen that the depth profile of the 80 layer thick as-built samples is highly tensile across the entire depth measured. In (b), it is evident that LSP has reversed the tensile stresses, and left the sample in a state of compressive residual stress. The maximum compressive residual stress is between 300 MPa and 400 MPa, and the sample remains in

compression to a depth of approximately 0.5 mm. It should be noted that Sample 2 in this group had it's strain gauge partially de-bond from the surface of the sample which resulted in a strain measurement pattern somewhat inconsistent with the other samples. It was found that the partial de-bonding occurred due to inconsistent glue film thickness caused by the high surface roughness of the samples.

In Figure 4.12, a similar stress depth profile is observed in the as-built samples. In the LSP treated samples (b), an identical inflexion is observed in both samples measured. This clearly shows the compressive residual stress, with a similar maximum value close to the surface, a compressive to tensile transition depth of approximately 0.4 mm, and a tensile region 0.4 mm and 0.7 mm. The distinct shape to the right of this curve is due to the hole drilling reaching the substrate plate bulk. This means that the stress state before LSP processing at this depth was compressive (relatively stress-free before L-PBF, and then compressive upon being printed on). This is not the case for the thicker samples since the drilling did not reach the substrate plate.

Between X-Ray Diffraction and Incremental Hole Drilling, it is evident that LSP on AM Ti-6Al-4V is capable of inducing a compressive residual stress to a substantial depth and magnitude. It is important to remember that this experiment was done on samples that were not stress-relieved or heat treated after the L-PBF process.

4.6 Microhardness

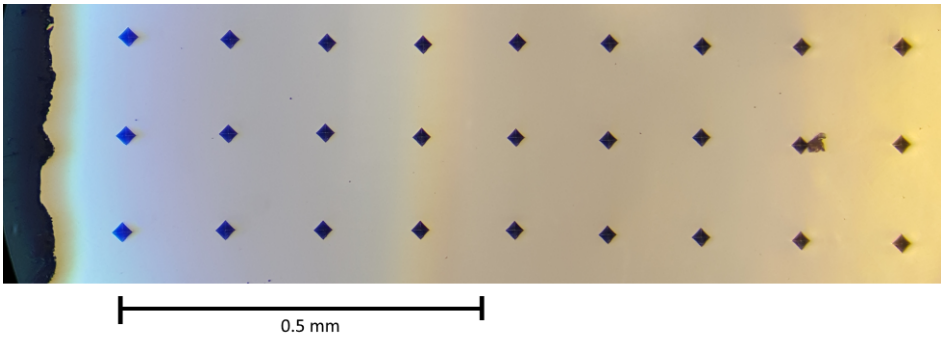


Figure 4.13: Microhardness Indentation Array

Figure 4.13 shows the indentation array created in the sample. Each depth has three measurements whose mean was calculated to represent the microhardness value at that depth. The depths measured ranged from 0.15 mm to 1.2 mm. The results of measurement were as follows:

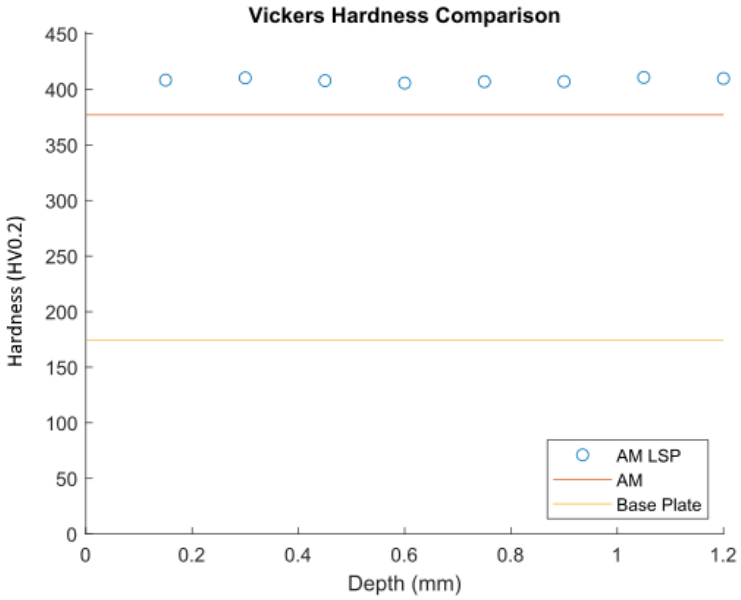


Figure 4.14: Microhardness Comparison

The Vickers microhardness of the Ti-6Al-4V wrought base plate is approximately 175 HV. This is less than half of the microhardness of as-built AM Ti-6Al-4V which averages 375 HV. Figure 4.14 shows the depth profile of microhardness for the LSP processed sample, the average microhardness of as-built AM Ti-6Al-4V, and the average microhardness of Ti-6Al-4V wrought plate. It is seen that the microhardness of as-built AM Ti-6Al-4V is consistently more than double the hardness of wrought Ti-6Al-4V plate, and the values measured were close to those found in literature. [54][55] LSP treatment is shown to increase the microhardness slightly. This can be attributed to an increase in dislocation density through cold work. A slight microhardness increase in the peened field has been observed in both shot peening [56] as well as LSP. [54]

4.7 Light Microscopy

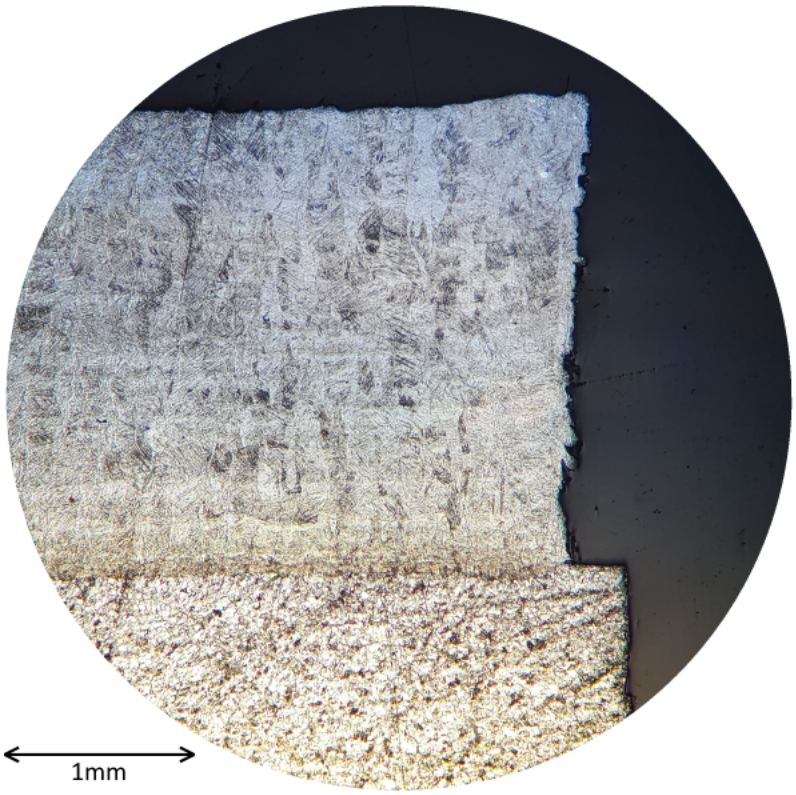


Figure 4.15: Comparison Section

Figure 4.15 shows a cross section of the edge of an 80 layer AM LSP treated sample. It is clear that L-PBF Ti-6Al-4V and wrought Ti-6Al-4V have vastly different microstructure. The microstructure of the wrought plate shows an equiaxed grain distribution with distinct alpha and beta phases. The L-PBF material exhibits columns of acicular microstructure, extending up in the build direction. Evidence of LSP processing is also visible on the top surface of the sample in the form of an indented surface due to the peening deformation.

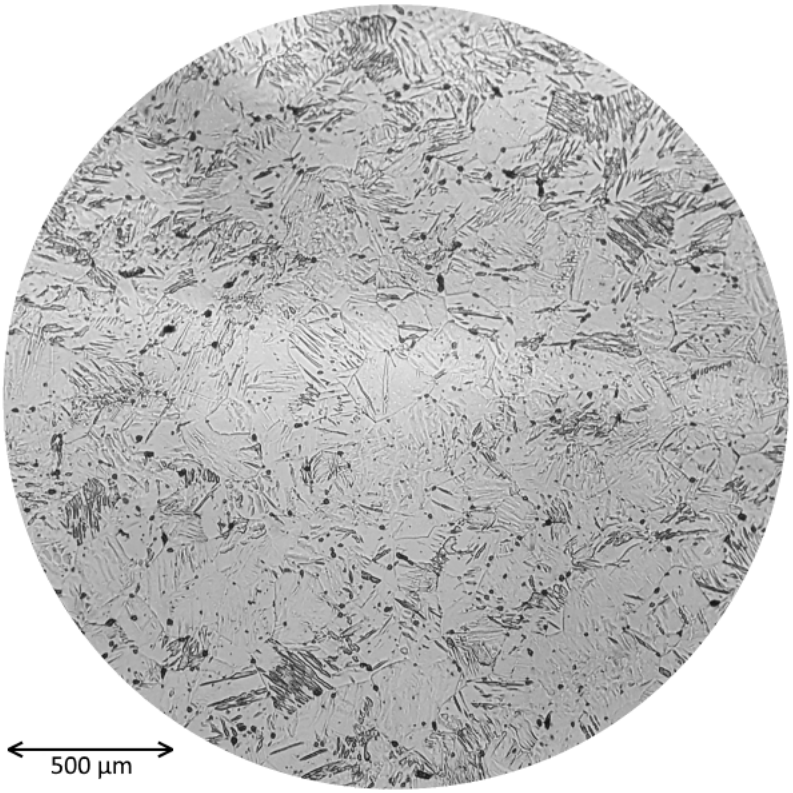


Figure 4.16: Plate Low Magnification

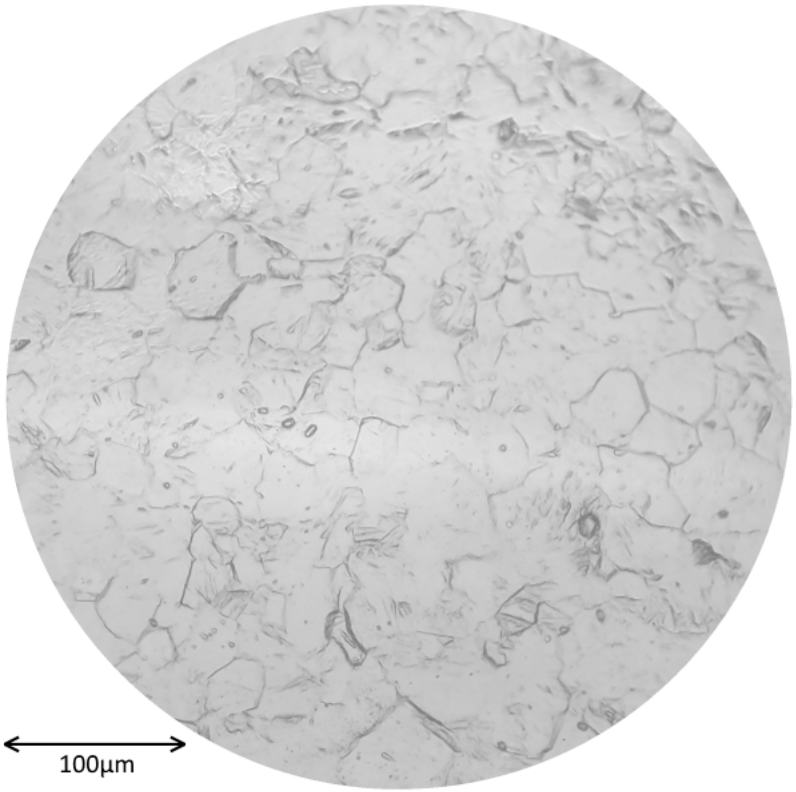


Figure 4.17: Ti-6Al-4V Plate High Magnification

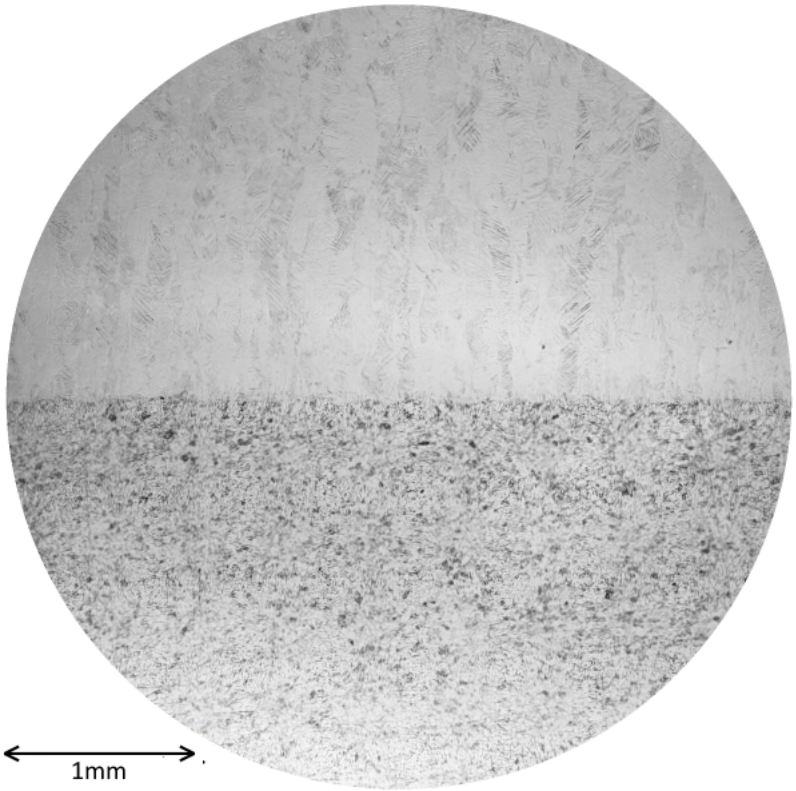


Figure 4.18: AM Boundary

Figures 4.16 and 4.17 show in more detail, the microstructure of the wrought Ti-6Al-4V base plate. Alpha and beta phases are clearly distinguishable, and average grain size is approximately 30 microns.

In Figure 4.18, the interface between wrought and AM material shows that there is no gradual change in microstructure which implies almost no heat affected zone in the substrate.

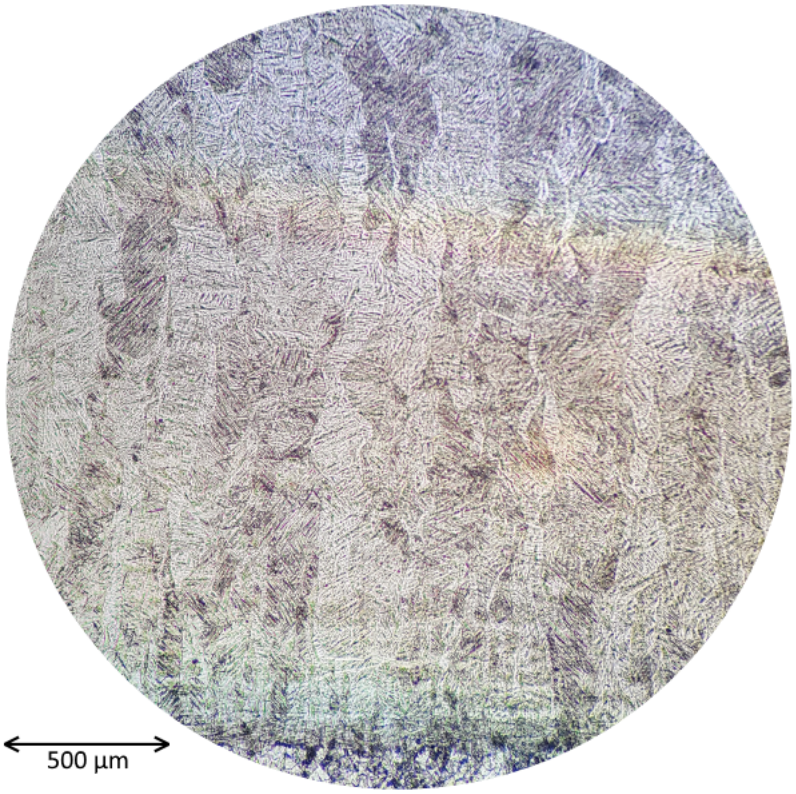


Figure 4.19: AM Low Magnification LSP Sample

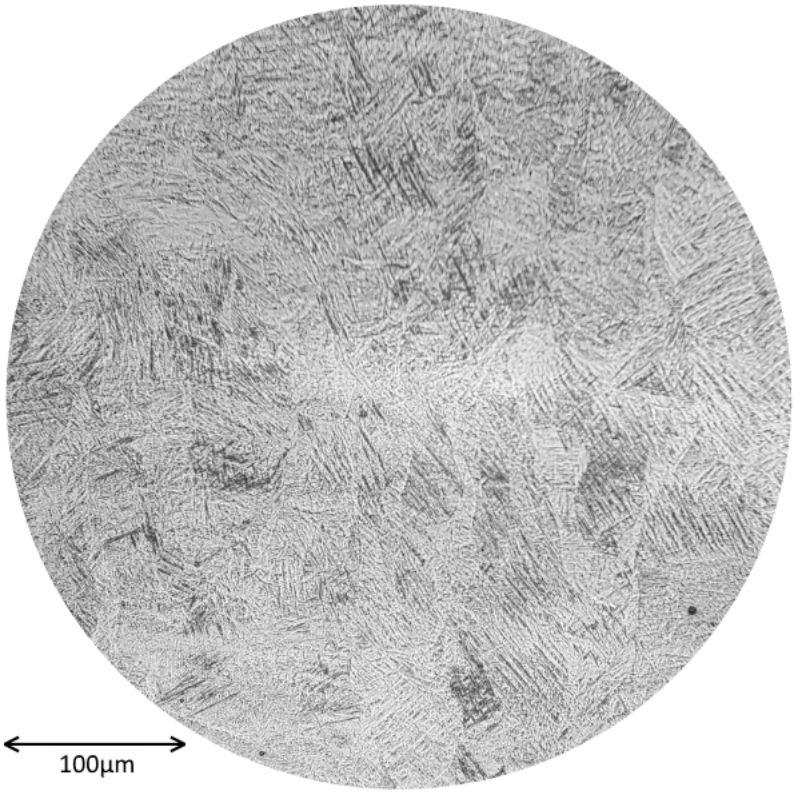


Figure 4.20: AM High Magnification LSP Treated Region

Figures 4.19 and 4.20 show the cross section of an 80 layer sample treated with LSP. There is no appreciable change in microstructure in the LSP treated region compared to the rest of the AM Ti-6Al-4V material. The acicular martensitic structures are abundant and this makes smaller changes in grain structure and distribution difficult to observe.

As-built L-PBF Ti-6Al-4V shows an anisotropic texture with columnar grains in the build direction. These columnar structures are beta phase, and they grow in this manner due to the partial remelting of the material below the current layer being melted. [57] L-PBF of Ti-6Al-4V results in extensive structures of alpha martensite as a result of the rapid cooling rates during the L-PBF process. [55] This can be mitigated by appropriate heat treatment after the L-PBF process.

4.8 Scanning Electron Microscopy

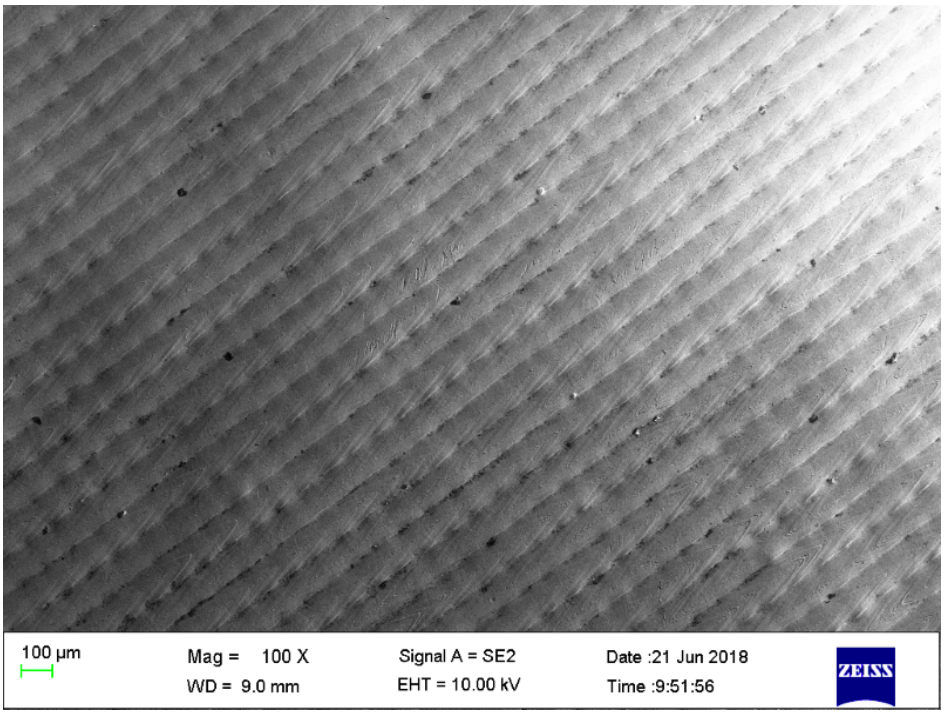


Figure 4.21: SEM AM 100X

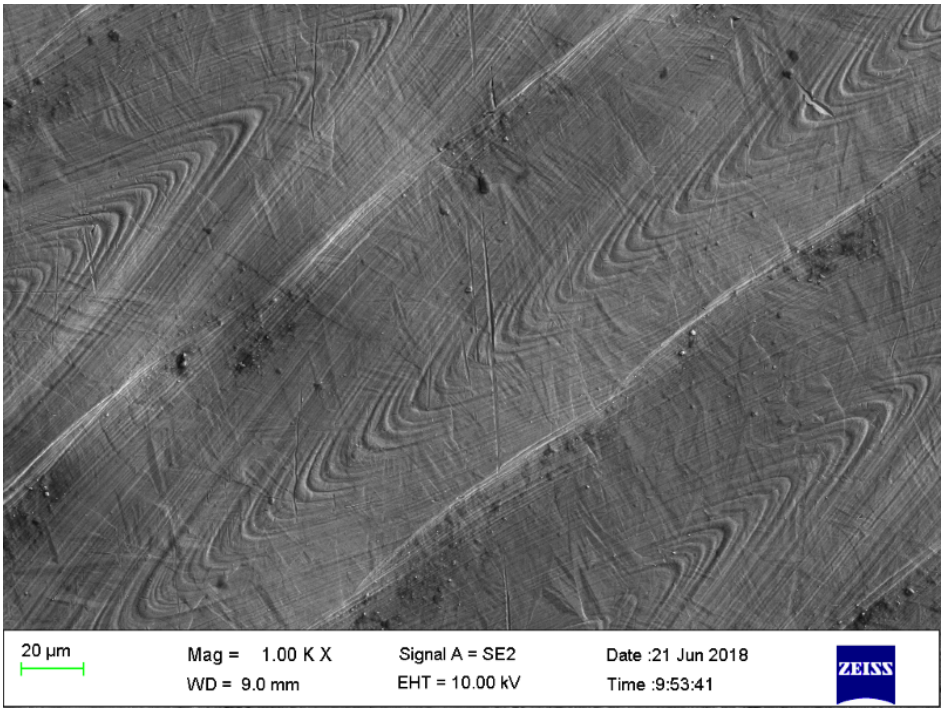


Figure 4.22: SEM AM 1000X

Figures 4.21 and 4.22 show the surface morphology of the as-built 1 layer sample. The weld pools are clearly seen, and the direction of the laser during each pass of hatching can be determined by the ripples.

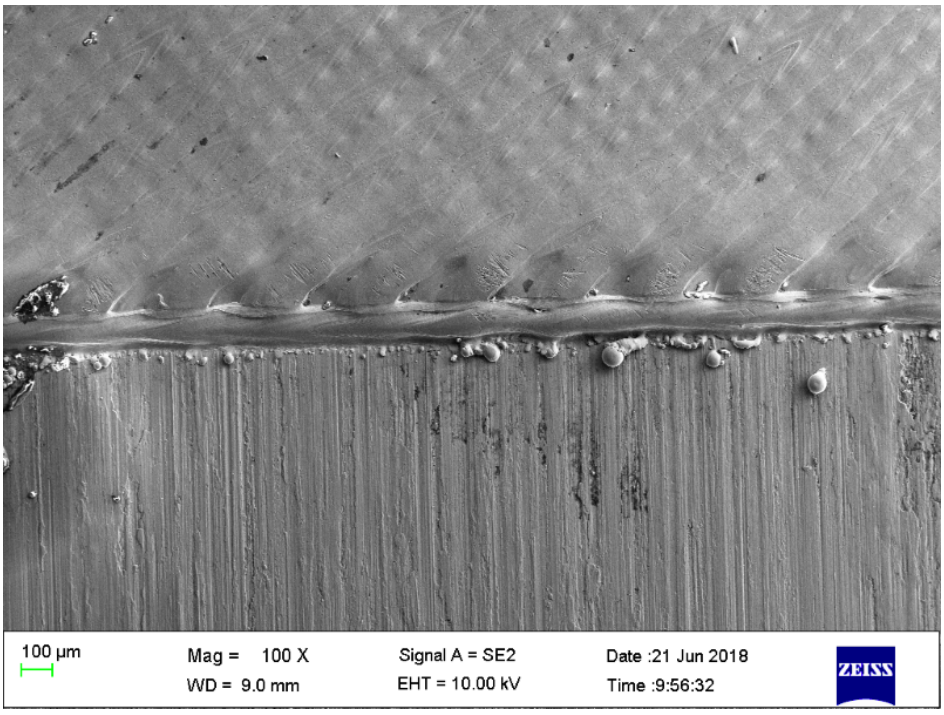


Figure 4.23: SEM AM Edge

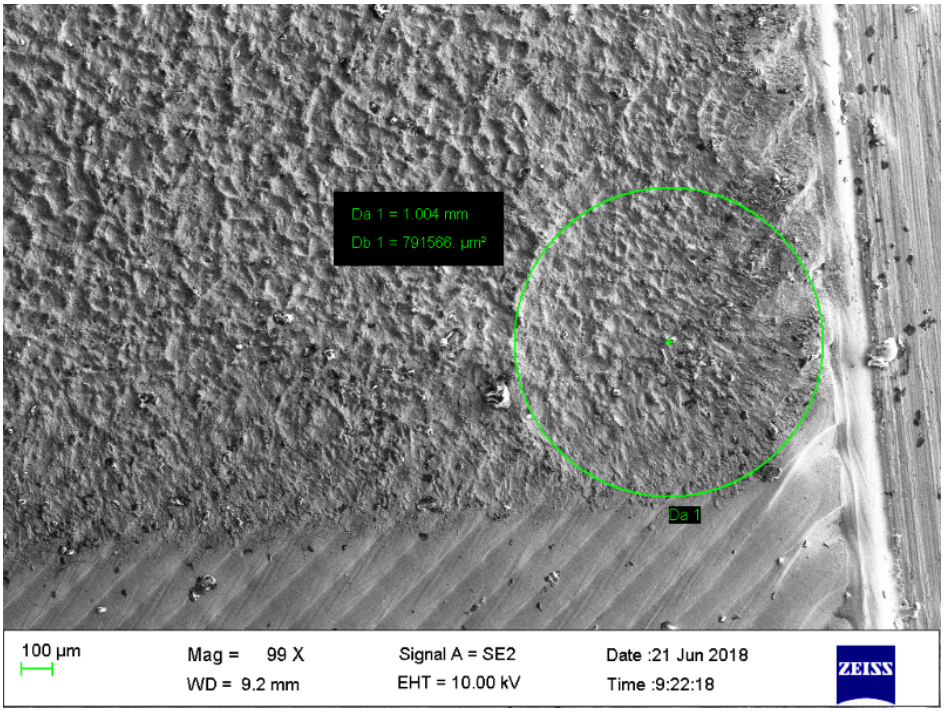


Figure 4.24: SEM AM Last LSP Spot

The edge of a sample is seen in Figure 4.23, with a small amount of spatter on the substrate plate. Small surface imperfections are evident between hatch lines which are candidates for crack initiation under fatigue loading.

Figure 4.24 shows the peened surface, and a crater from the last LSP pulse. There is loose oxide on the material around the LSP treated region.

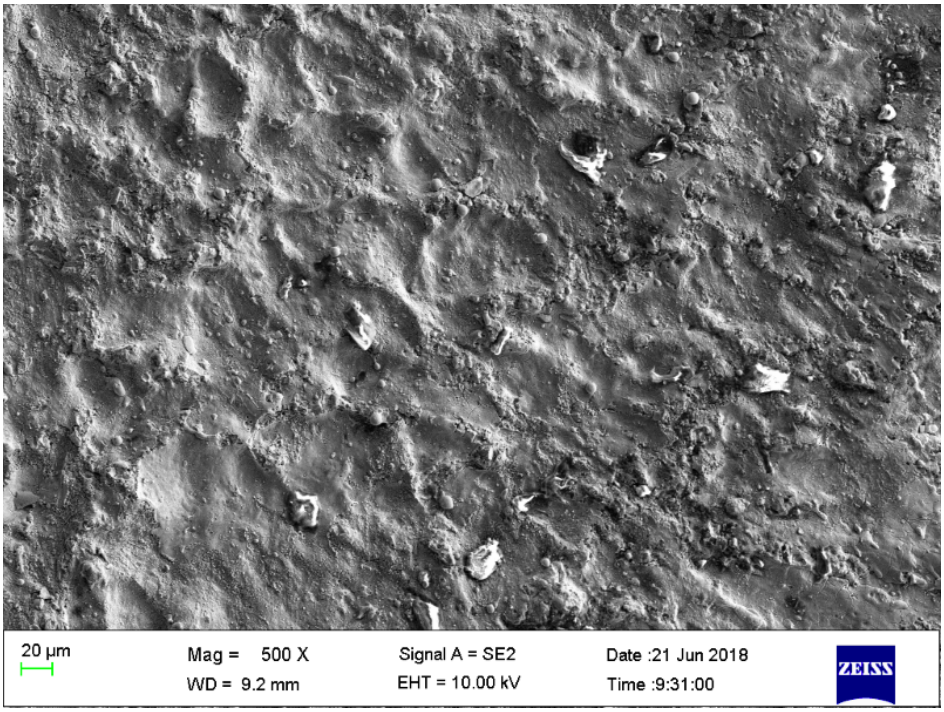


Figure 4.25: SEM AM LSP Surface 500X

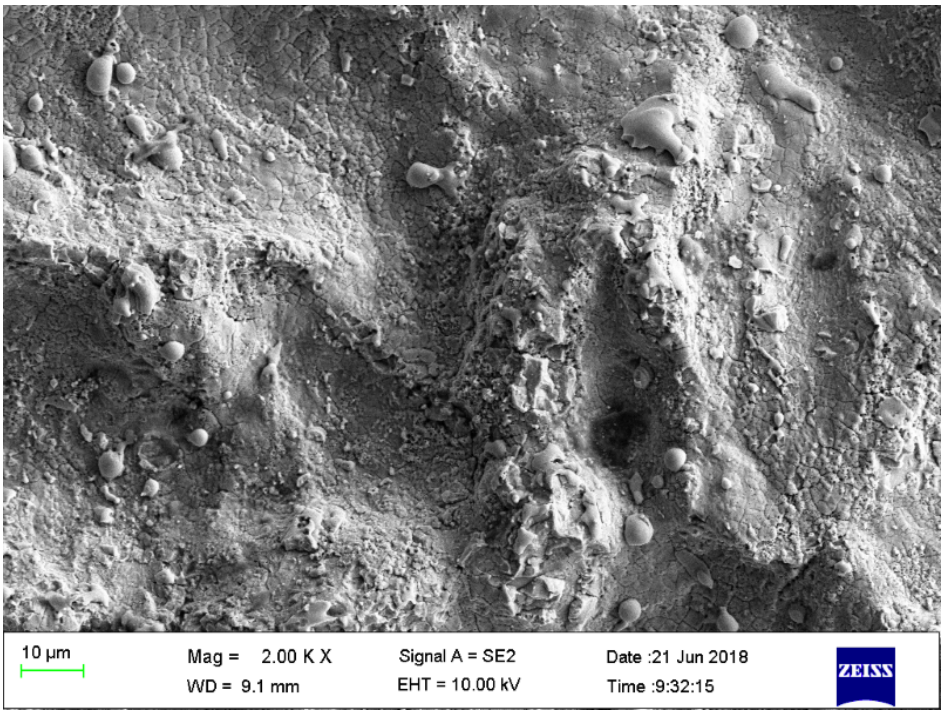


Figure 4.26: SEM AM LSP Surface 2000X

Figures 4.25 and 4.26 are close-ups of the peened surface. The oxide layer is brittle (lots of small cracks formed during cooling) and the relief highly irregular.

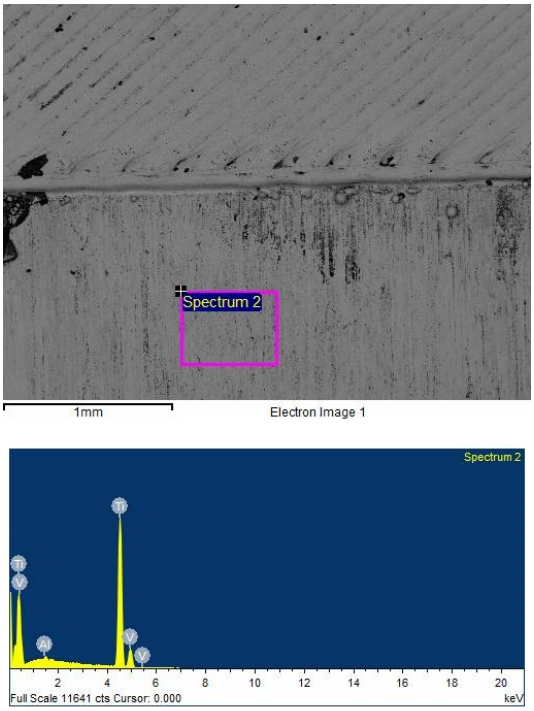


Figure 4.27: EDX Composition Plate

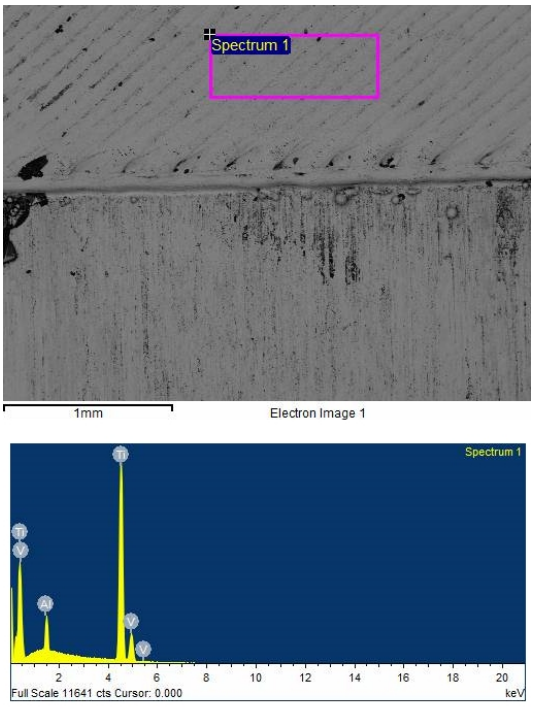


Figure 4.28: EDX Composition AM

The EDX graphs above (Figures 4.27 and 4.28) show the composition of the Ti-6Al-4V base plate and the L-PBF Ti-6Al-4V regions. As expected, the composition is titanium, aluminium, and vanadium.

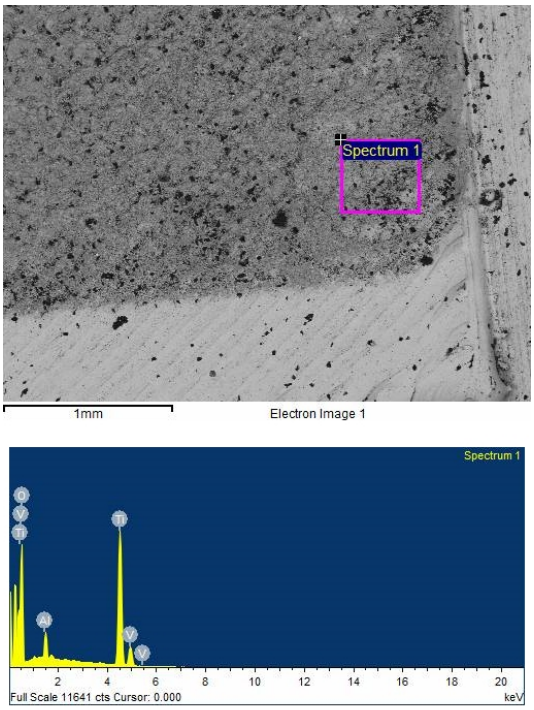


Figure 4.29: EDX Composition AM LSP Last Spot

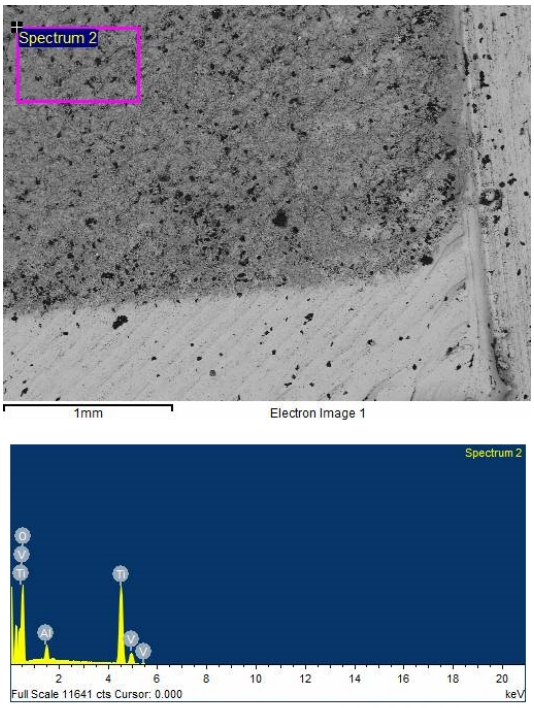


Figure 4.30: EDX Composition AM LSP Mid Raster

The EDX graphs for the LSP processed samples (Figures 4.29 and 4.30) reveals a major addition of oxygen to the composition of the scanned region. This shows the extent of the oxidation on the surface.

The SEM images reveal a wealth of information about the surface of the as-built and LSP L-PBF Ti-6Al-4V surface morphologies. The as-built surface has highly regular hatch patterns with small imperfections occurring mainly between scan lines. The surface of LSP processed samples is shown to have a brittle, superficial layer of oxide which perhaps makes the surface look much worse than the metal below. Further work includes removing the oxide layer using chemical techniques to observe the surface of the underlying Ti-6Al-4V material. The EDX Composition scans confirm that the black appearance is Titanium Oxide. The short but extreme temperature achieved during the plasma generation followed by rapid cooling forms a metastable TiO. [58] The surface of Ti-6Al-4V could be protected using sacrificial coatings applied before LSP processing.

4.9 Comparison of Results to Literature

Four papers are of particular interest when comparing results of this research project. Kalentics et al.[1], Glaser et al.[59], Guo et al. [37] and Yeo et al. [38] conducted research with many similarities to this experiment, however with different LSP parameters, and with some differences in surfaces and residual stresses pre-LSP. It was thus important to assess the results critically against those of these four papers.

	Ivanovic	Kalentics	Glaser	Guo	Yeo
Pulse Energy (J)	0.265	0.4	0.265	15	1.4
Wavelength (nm)	1064	532	1064	1064	532
Frequency (Hz)	20	1	20	1	10
Power Density (GW/cm2)	8	7.2	8	5.6	9.75
Spot Size (mm)	0.8	1	0.8	4	1.34
Coverage (%)	98	80	98	50	50
Pattern	Raster	Raster	Raster	Raster	Raster
Notes	As-Built	As-Built	Machined	Machined	Heat Treated

Figure 4.31: Comparison of LSP Parameters

4.9.1 Residual Stress

This experiment shows that LSP on AM Ti-6Al-4V resulted in a substantial reversal of residual stresses found in the as-built samples. Maximum compressive residual stress achieved

was approximately 350 MPa and the depth to which it was in compression was approximately 0.5 mm. In comparison, Kalentics et al. observed a maximum compressive residual stress of approximately 275 MPa to a depth of 0.45 mm using a coverage of 40%, and a maximum compressive residual stress of approximately 700 MPa up to a depth of 0.8 mm using a coverage of 80%. Guo et al. shows a maximum compressive residual stress after LSP of approximately 200 MPa, to a depth of 0.7 mm. Yeo et al. achieved approximately 505 MPa compressive residual stress at the surface of the material. However, as noted above, the samples did undergo heat treatment first and were thus relatively low-stress before LSP, so this result should be considered with that in mind. The residual stress results in this research are thus found to be in reasonable agreement with those found in existing literature.

4.9.2 Microhardness

The measurements in this experiment show a microhardness of 175 HV for wrought Ti-6Al-4V, 375 HV for as-built AM Ti-6Al-4V, and an increase in microhardness after LSP to approximately 410 HV near the surface of the material. This compares very closely with the microhardness findings by Guo et al. (361 HV before to 420 HV after LSP).

Although Yeo et al. had processed their samples with heat treatment before LSP, it is still shown in the paper that an increase in microhardness by approximately 45 HV was seen after LSP.

4.9.3 Surface Roughness

This experiment found the surface roughness of as-built AM Ti-6Al-4V to be 6.5 µm Ra and 35 µm Rz. After LSP the surface roughness reduced to 3 µm Ra and 15 µm Rz. The as-built values corresponds to the findings of Glaser et al., and the LSP surface roughness values are also very close despite Glaser et al. machining and polishing the samples prior to LSP. This indicates that the surface roughness post LSP may not be particularly sensitive to the initial surface roughness before LSP. Yeo et al. also observed a reduction in surface roughness post LSP, however the results should not be compared directly since the coverage of the LSP set-up was much lower than what was used in this experiment and hence would result in a substantially less uniform surface (higher roughness).

5 Conclusions and Recommendations

This chapter contains a summary of the observations, results and conclusions established through this research, a critical evaluation of the objectives, and it also provides suggestions and recommendations for further research on this topic and the field in general.

5.1 Conclusion

The purpose of this project was to set the groundwork for post-processing L-PBF Ti-6Al-4V using the Laser Shock Peening (LSP) surface treatment process. Understanding the intricacies of L-PBF process is of high value but high complexity. The thermal processes that occur with each layer melting and cooling, result in a part which contains extremely high tensile residual stresses near the surface, which have to be mitigated.

Ti-6Al-4V samples of varying thickness were manufactured using the L-PBF process on a wrought substrate plate, and one half of the samples was processed using LSP to incorporate compressive residual stress in the near-surface region of the samples. The surface roughness although being an improvement on the as-built state, was of higher frequency and was mostly attributed to the presence of the superficial oxide layer. Using X-Ray Diffraction it was shown that the surface was in a good state of compression, and using Incremental Hole Drilling, the depth profile showed acceptable performance of LSP using the current set-up and process parameters. The microhardness analysis showed that due to the increased dislocation density in the cold worked region, there was a slight increase in microhardness in the LSP treated region. It was also concluded that the microhardness of as-built L-PBF Ti-6Al-4V was more than double that of wrought Ti-6Al-4V plate. Using microscopy it was concluded that there was no obvious change in microstructure in the LSP treated region of L-PBF Ti-6Al-4V when compared to as-built material. Since LSP is a cold working mechanical process, this is in agreement with expectation. SEM microscopy has shown the nature of the effects of LSP on the surface of the AM Ti-6Al-4V samples, and the that the resulting oxide layer was thin and purely superficial.

5.2 Evaluation of Objectives

- The experiment was deemed successful, and the results proved insightful into the effectiveness of the use of the LSP process as a method of post-processing AM (L-PBF) manufactured Ti-6Al-4V.
- This experiment thus concludes that LSP can indeed be effective in inducing a beneficial compressive residual stress of sufficient depth and magnitude in AM Ti-6Al-4V.
- The effect that the LSP process had on the surface of AM Ti-6Al-4V was found to be a substantial reduction in surface roughness.
- There were found to be no noticeable changes to the microstructure by performing LSP on as-built AM Ti-6Al-4V. The surface morphology was seen to have changed substantially upon performing LSP on AM Ti-6Al-4V, which results in a superficial oxide layer and a much smaller amplitude but higher frequency surface roughness.

5.3 Recommendations

The first recommendation for furthering of this research is to stress relieve and heat treat Ti-6Al-4V samples to a standard appropriate for use in a selected application. Starting with relatively stress-free material would be a better representation of LSP capability on production parts. Since AM components often undergo final machining at dimensionally critical regions (bearing surfaces and fastener holes), it would be beneficial to investigate these scenarios by machining a portion of L-PBF Ti-6Al-4V samples, and exploring the stresses and surface roughness before and after machining and also before and after LSP on the machined surface. A parametric study should also be performed on exploring the effects of changing LSP process parameters on the stress, hardness and surface state of L-PBF Ti-6Al-4V samples. It would also be useful to measure stress using more techniques such as Synchrotron X-Ray Diffraction and Neutron Diffraction to get deeper diffraction measurements. Investigation should also be done to determine the effectiveness of LSP in closing pores which are often characteristic of the L-PBF process. This project has set the groundwork for research of LSP on L-PBF Ti-6Al-4V and has provided just as many new questions as it has answers. The understanding in the field of LSP on L-PBF Ti-6Al-4V is still in its infancy, but there is a lot of knowledge to be gained. Since both of these technologies are used in abundance in the field of aerospace, it would be recommended that further research on this topic be performed in direct context of a particular aerospace application.

6 Contributions to the Scientific Community

This chapter contains the various contributions made by this research project to the broader scientific community in the form of posters, presentations, and abstracts which are included in Appendix A.

6.1 Conferences

6.1.1 International Conference on Mechanical Stress Evaluation by Neutron and Synchrotron Radiation (MECA SENS)

The author presented the research project at the 9th International Conference on Mechanical Stress Evaluation by Neutron and Synchrotron Radiation on the 19-21 September 2017 hosted in Skukuza, South Africa.

6.1.2 18th Annual Rapid Product Development Association of South Africa (RAPDASA) Conference

The author contributed to experimental work towards a paper by D. Glaser et al. and a presentation thereof at the 18th Annual Rapid Product Development Association of South Africa Conference 7 - 10 November 2017 hosted by the Durban ICC, South Africa.

6.1.3 International Conference on Laser Peening and Related Phenomena (ICLPRP)

This project featured in the book of abstracts for the 7th International Conference on Laser Peening and Related Phenomena 17-22 June 2018 hosted in Singapore. A poster describing

the experiment and outlining the results and findings was prepared and put on display at the conference.

6.2 Workshops

6.2.1 African Laser Center (ALC) Student Workshop

The author presented the research project at the 10th African Laser Centre Student Workshop 30 November - 2 December 2017 hosted at the Wallenburg Research Centre of the University of Stellenbosch.

6.3 Awards

The following awards were won by the author during the course of the project:

- 3rd Best Student Presentation Prize at the 9th International Conference on Mechanical Stress Evaluation by Neutron and Synchrotron Radiation, MECA SENS 2017 in September 2017.
- Best MSc Student Presentation Award at the 10th African Laser Centre Student Workshop 2017 in December 2017.

References

[6] Siemens, "Additive manufacturing with nx," 2018. [Online]. Available: https://europac3d.com/wp-content/uploads/2018/03/Siemens-PLM-Additive-Manufacturing-with-NX-fs-61073-A5.pdf

[9] J. Kerr, "Human femur," Royal Photographic Society, 2018, part of a photographic collection. [Online]. Available: https://rps-science.org/events/International-Images-for-Science/photographer/image/2176/

[12] G. Speak, "Airbus study finds significant advantage in 3d printing for standardized parts," 2014. [Online]. Available: https://gfxspeak.com/2014/02/28/significant-advantage-standardized/

[13] Metal-AM, "Spritzguss + formenbau bergmann adds eos metal additive manufacturing system for high grade tool production," 2014. [Online]. Available: https://www.metal-am.com/spritzguss-formenbau-bergmann-adds-eos-metal-additive-manufacturing-system-for-high-grade-tool-production/

[14] CRPM, "Hemi-maxilla implant," 2017. [Online]. Available: http://www.crpm.co.za/project/hemi-maxilla-implant/

[17] T. zel, A. Altay, B. Kaftanolu, N. Senin, R. Leach, and M. Donmez, "Focus variation measurement and prediction of surface texture parameters using machine learning in laser powder bed fusion," *Journal of Manufacturing Science and Engineering*, vol. 142, p. 011008, 11 2019.

[18] Askeland, "Science and engineering of materials," in *Science and Engineering of Materials*. Cengage, 2010, ch. 7-6.

[25] U. of Waterloo, "Residual stress," 2018. [Online]. Available: https://uwaterloo.ca/fatigue-stress-analysis-lab/research/residual-stress

[37] W. Guo, R. Sun, B. Song, Y. Zhu, F. Li, Z. Che, B. Li, C. Guo, L. Liu, and P. Peng, "Laser shock peening of laser additive manufactured ti6al4v titanium alloy," *Surface and Coatings Technology*, vol. 349, pp. 503–510, 2018. [Online]. Available: https://www.sciencedirect.com/science/article/pii/S0257897218305954

[38] I. Yeo, B. Seongguk, A. Amanov, and S. Jeong, "Effect of laser shock peening on properties of heat-treated ti6al4v manufactured by laser powder bed fusion," *International Journal of Precision Engineering and Manufacturing-Green Technology*, 06 2020.

[43] M. F. et al., "Determination of residual stresses by x-ray diffraction - issue 2," p. 74, 2005.

[47] Vasantha, "Manufacturing," 2019. [Online]. Available: https://www.vasantha.com/manufacturing.html

[48] ProtoXRD, "ixrd standard," 2018. [Online]. Available: https://www.protoxrd.com/products/residual-stress-measurement/ixrd-portable

[49] S. Technology, "Mts3000 restan," 2018. [Online]. Available: https://sint-technology.com/mts-3000/

[50] Zeiss, "Stereo discovery v8," 2018. [Online]. Available: https://www.micro-shop.zeiss.com/en/de/system/stereo+discovery-stereo+discovery.v8-stereomicroscopes/10156/

[51] Buehler, "Isomet low speed precision cutter," 2019. [Online]. Available: https://www.buehler.com/isoMet-low-speed-cutter.php

[52] Struers, "Labosystem," 2019. [Online]. Available: https://www.struers.com/en/Products/Grinding-and-Polishing/Grinding-and-polishing-equipment/LaboSystem

[53] Labcompare, "Zeiss sigma fe-sem for high quality imaging and advanced analytical microscopy from carl zeiss microscopy," 2019. [Online]. Available: https://www.labcompare.com/1346-Scanning-Electron-Microscopes-SEM/56203-SIGMA-Field-Emission-Scanning-Electron-Microscopes/

[1] N. Kalentics, E. Boillat, P. Peyre, C. Gorny, C. Kenel, C. Leinenbach, J. Jhabvala, and R. E. Log, "3d laser shock peening a new method for the 3d control of residual stresses in selective laser melting," *Materials & Design*, vol. 130, pp. 350–356, 2017. [Online]. Available: https://www.sciencedirect.com/science/article/pii/S0264127517305658

[2] I. Yadroitsev and I. Yadroitsava, "Evaluation of residual stress in stainless steel 316l and ti6al4v samples produced by selective laser melting," *Virtual and Physical Prototyping*, vol. 10, no. 2, pp. 67–76, 2015. [Online]. Available: https://doi.org/10.1080/17452759.2015.1026045

[3] P. Edwards and M. Ramulu, "Fatigue performance evaluation of selective laser melted ti6al4v," *Materials Science and Engineering: A*, vol. 598, pp. 327–337, 2014. [Online]. Available: https://www.sciencedirect.com/science/article/pii/S0921509314000720

[4] C. Li, Z. Liu, X. Fang, and Y. Guo, "Residual stress in metal additive manufacturing," *Procedia CIRP*, vol. 71, pp. 348–353, 2018, 4th CIRP Conference on Surface Integrity (CSI 2018). [Online]. Available: https://www.sciencedirect.com/science/article/pii/S221282711830667X

[5] Y. Zhang, J. Lu, X. Ren, H. Yao, and H. Yao, "Effect of laser shock processing on the mechanical properties and fatigue lives of the turbojet engine blades manufactured by ly2 aluminum alloy," *Materials & Design*, vol. 30, no. 5, pp. 1697 – 1703, 2009. [Online]. Available: http://www.sciencedirect.com/science/article/pii/S0261306908003555

[7] C. Klahn, B. Leutenecker, and M. Meboldt, "Design strategies for the process of additive manufacturing," *Procedia CIRP*, vol. 36, pp. 230 – 235, 2015, cIRP 25th Design Conference Innovative Product Creation. [Online]. Available: http://www.sciencedirect.com/science/article/pii/S2212827115008938

[8] A. PARFITT, "Chapter 28 - modeling and remodeling: How bone cells work together," in *Vitamin D (Second Edition)*, second edition ed., D. FELDMAN, Ed. Burlington: Academic Press, 2005, pp. 497–513. [Online]. Available: https://www.sciencedirect.com/science/article/pii/B9780122526879500310

[10] Engineering.com, "Lessons engineers and architects should learn from nature and topology optimization," 2017. [Online]. Available: https://www.engineering.com/DesignSoftware/DesignSoftwareArticles/ArticleID/15463/Lessons-Engineers-and-Architects-Should-Learn-from-Nature-and-Topology-Optimization.aspx

[11] D. Technology, "Dmls applications," 2018. [Online]. Available: https://dmlstechnology.com/dmls-applications

[15] ASTM, "Subcommittee f42.05 on materials and processes," 2018. [Online]. Available: https://www.astm.org/COMMIT/SUBCOMMIT/F4205.htm

[16] Metal-AM, "Metal additive manufacturing processes," 2019. [Online]. Available: https://www.metal-am.com/introduction-to-metal-additive-manufacturing-and-3d-printing/metal-additive-manufacturing-processes/

[19] M. Zäh and G. Branner, "Investigations on residual stresses and deformations in selective laser melting," *Production Engineering*, vol. 4, pp. 35–45, 2010.

[20] L. C. Campanelli, "A review on the recent advances concerning the fatigue performance of titanium alloys for orthopedic applications," *Journal of Materials Research*, p. 115, 2020.

[21] M. Kahlin, H. Ansell, D. Basu, A. Kerwin, L. Newton, B. Smith, and J. Moverare, "Improved fatigue strength of additively manufactured ti6al4v by surface post

processing," *International Journal of Fatigue*, vol. 134, p. 105497, 2020. [Online]. Available: https://www.sciencedirect.com/science/article/pii/S0142112320300281

[22] J. Pegues, M. Roach, R. Scott Williamson, and N. Shamsaei, "Surface roughness effects on the fatigue strength of additively manufactured ti-6al-4v," *International Journal of Fatigue*, vol. 116, pp. 543–552, 2018. [Online]. Available: https://www.sciencedirect.com/science/article/pii/S0142112318302986

[23] M. Nakatani, H. Masuo, Y. Tanaka, and Y. Murakami, "Effect of surface roughness on fatigue strength of ti-6al-4v alloy manufactured by additive manufacturing," *Procedia Structural Integrity*, vol. 19, pp. 294–301, 2019, fatigue Design 2019, International Conference on Fatigue Design, 8th Edition. [Online]. Available: https://www.sciencedirect.com/science/article/pii/S2452321619305001

[24] D. Greitemeier, C. D. Donne, F. Syassen, J. Eufinger, and T. Melz, "Effect of surface roughness on fatigue performance of additive manufactured ti6al4v," *Materials Science and Technology*, vol. 32, no. 7, pp. 629–634, 2016. [Online]. Available: https://doi.org/10.1179/1743284715Y.0000000053

[26] S. Liu and Y. C. Shin, "Additive manufacturing of ti6al4v alloy: A review," *Materials and Design*, vol. 164, p. 107552, 2019. [Online]. Available: https://www.sciencedirect.com/science/article/pii/S026412751830916X

[27] R. Boyer, "An overview on the use of titanium in the aerospace industry," *Materials Science and Engineering: A*, vol. 213, no. 1, pp. 103–114, 1996, international Symposium on Metallurgy and Technology of Titanium Alloys. [Online]. Available: https://www.sciencedirect.com/science/article/pii/0921509396102331

[28] V. S. de Viteri and E. Fuentes, "Titanium and titanium alloys as biomaterials," in *Tribology*, J. Gegner, Ed. Rijeka: IntechOpen, 2013, ch. 5. [Online]. Available: https://doi.org/10.5772/55860

[29] CSIR, "Boeing joins hands with south africa to research and develop titanium powder for manufacturing," 2013. [Online]. Available: https://www.csir.co.za/boeing-joins-hands-south-africa-research-and-develop-titanium-powder-manufacturing

[30] N. Shen, H. Ding, Q. Wang, and H. Ding, "Effect of confinement on surface modification for laser peen forming without protective coating," *Surface and Coatings Technology*, vol. 289, pp. 194–205, 2016. [Online]. Available: https://www.sciencedirect.com/science/article/pii/S0257897216300548

[31] L. Technologies, "Laser peening process," 2018. [Online]. Available: https://www.lsptechnologies.com/laser-peening-process.php

[32] P. Smith, M. Shepard, P. Prevey, and A. Clauer, "Effect of power density and pulse repetition on laser shock peening of ti-6al-4v," *Journal of Materials Engineering and Performance - J MATER ENG PERFORM*, vol. 9, pp. 33–37, 02 2000.

[33] C. Correa, D. Peral, J. Porro, M. Daz, L. Ruiz de Lara, A. Garca-Beltrn, and J. Ocaa, "Random-type scanning patterns in laser shock peening without absorbing coating in 2024-t351 al alloy: A solution to reduce residual stress anisotropy," *Optics & Laser Technology*, vol. 73, pp. 179–187, 2015. [Online]. Available: https://www.sciencedirect.com/science/article/pii/S0030399215001218

[34] L. Hackel, J. R. Rankin, A. Rubenchik, W. E. King, and M. Matthews, "Laser peening: A tool for additive manufacturing post-processing," *Additive Manufacturing*, vol. 24, pp. 67 – 75, 2018. [Online]. Available: http://www.sciencedirect.com/science/article/pii/S2214860418303397

[35] W. Braisted and R. Brockman, "Finite element simulation of laser shock peening," *International Journal of Fatigue*, vol. 21, no. 7, pp. 719–724, 1999. [Online]. Available: https://www.sciencedirect.com/science/article/pii/S0142112399000353

[36] Q. Liu, S. Barter, and G. Clark, "Comparison of shot peening and laser shock peening techniques in enhancing fatigue life of 7xxx series aluminium alloys," 02 2002, pp. 153–158.

[39] S. R. Mannava, "Us patent no. us5951790a - method of monitoring and controlling laser shock peening using an in plane deflection test coupon," Sep 1999.

[40] A. Clauer, "Laser shock peening, the path to production," *Metals*, vol. 9, p. 626, 05 2019.

[41] S. van Staden, C. Polese, D. Glaser, J. Nobre, A. Venter, D. Marais, J. Okasinski, and J.-S. Park, "Measurement of residual stresses in different thicknesses of laser shock peened aluminium alloy samples," 01 2017.

[42] A. Niku-Lari, J. Lu, and J. Flavenot, "Measurement of residual-stress distribution by the incremental hole-drilling method," *Journal of Mechanical Working Technology*, vol. 11, no. 2, pp. 167–188, 1985. [Online]. Available: https://www.sciencedirect.com/science/article/pii/0378380485900233

[44] N. Rossini, M. Dassisti, K. Benyounis, and A. Olabi, "Methods of measuring residual stresses in components," *Materials and Design*, vol. 35, pp. 572–588, 2012.

[45] C. Riekel, "The use of synchrotron radiation for materials research," *Analysis of Residual Stress by Diffraction using Neutron and Synchrotron Radiation*, 2003. [Online]. Available: https://doi.org/10.1201/9780203608999.ch2

[46] D. Brown, J. Bernardin, J. Carpenter, B. Clausen, D. Spernjak, and J. Thompson, "Neutron diffraction measurements of residual stress in additively manufactured stainless steel," *Materials Science and Engineering*, vol. 678, pp. 291–298, 2016. [Online]. Available: https://doi.org/10.1016/j.msea.2016.09.086

[54] S. Varin, Y. Jain, P. Subramaniyan, and S. Kalainathan, "Influence of multiple laser shock peening without coating on ti-6al-4v alloy for aircraft applications," 04 2017.

[55] P. Barriobero-Vila, J. Gussone, J. Haubrich, S. Sandlobes, J. Da Silva, P. Cloetens, N. Schell, and G. Requena, "Inducing stable a + b microstructures during selective laser melting of ti-6al-4v using intensified intrinsic heat treatments," *Materials*, vol. 10, 03 2017.

[56] K. Tosha, "Influence of residual stresses on the hardness number in the affected layer produced by shot peening," *2nd Asia-Pacific Forum on Precision Surface Machining and Deburring Technology*, 01 2002.

[57] V. Chastand, A. Tezenas, Y. Cadoret, P. Quaegebeur, W. Maia, and E. Charkaluk, "Fatigue characterization of titanium ti-6al-4v samples produced by additive manufacturing," *Procedia Structural Integrity*, vol. 2, pp. 3168–3176, 12 2016.

[58] J. L. Gonzlez-Carrasco, J. L. Ocaa, H. Carreon, J. Porro, and S. Barriuso, "Characterization of laser peening-induced effects on a biomedical ti6al4v alloy by thermoelectric means," *Optical Engineering*, vol. 53, 12 2014.

[59] D. Glaser, S. van Staden, N. Ivanovic, and C. Polese, "The potential enhancement of components produced by metal additive manufacturing using laser shock processing," in *RAPDASA 2017 CONFERENCE PROCEEDINGS*. RAPDASA, 11 2017, p. 91.

Appendix A Conference Abstracts, Proceedings and Posters

THE POTENTIAL ENHANCEMENT OF COMPONENTS PRODUCED BY METAL ADDITIVE MANUFACTURING USING LASER SHOCK PROCESSING

D. Glaser[1*], S. N. van Staden[2], N. Ivanovic[2], C. Polese[2]

ABSTRACT

Additive manufacturing of high performance alloys such as Ti-6Al-4V potentially allows for improved component design and manufacturing, and is of specific interest to the aerospace industry due to the enhancements in final geometry, weight, and even cost. Potential applications of metal additive manufacturing components would offer a performance enhancement compared to conventional manufacturing techniques, therefore the use of a final surface enhancement process to provide further performance improvements may be highly beneficial to achieve superior components. The use of laser shock processing is explored as a potential technology in order to generate beneficial compressive residual stresses into metal additive manufacturing components. Preliminary results reveal that the LSP process can effectively achieve compressive residual stresses to a depth of near 1 mm in Ti-6Al-4V.

1. Introduction

Additive manufacturing (AM) is a general term used to describe methods of building articles directly from a computer model. Typically, AM products are built up layer by layer to produce a complete or near net shaped component [1]. The AM process is specifically attractive for the manufacturing of high-value metal components as the geometric flexibility from a design and manufacturing perspective offers potential benefits in overall component performance in terms of weight and production cost. There is currently significant interest in the aerospace industry regarding the use of AM for component production, due to the perpetual pursuit of the aerospace industry to deliver components with reduced weight and improved performance at lower cost while maintaining high reliability. Since a large drive to develop metal AM technology is based on the requirement for superior component performance, the consideration of potential enhancements due to post-processing techniques is a vital consideration for successful technology adoption.

Peening technology is a well-established technique in order to enhance the mechanical performance of metal components by introduction of beneficial compressive residual stresses. Crack-based failure phenomena such as fatigue or stress corrosion cracking can be drastically affected by the presence of residual stresses. Essentially cracks initiate and propagate under tensile stresses, therefore the introduction of compressive residual stresses into the surface of the component can lead to significant performance enhancements.

Laser shock peening or laser shock processing (LSP) is one of the most advanced forms of peening technology with superior performance compared to conventional techniques such as mechanical shot peening (SP). Typically the depth of compressive residual stresses achievable by with LSP technology are on a millimetre range (often 10 times deeper than conventional SP) with virtually no surface roughness introduced. The implementation of LSP to high value components can result in order of magnitude life enhancements in terms of fatigue performance. The schematic in Figure 1 illustrates the LSP process

mechanism, which uses a pulsed laser beam in order to generate a high pressure plasma expansion on the component surface. The plasma reaches Giga-Pascal magnitudes in a nano-second time frame, which drives a shock wave through the metal work-piece with sufficient strength to yield the metal and hence generate beneficial compressive residual stresses through the target surface [2].

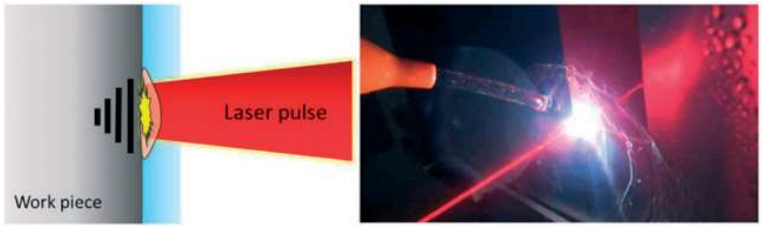


Figure 1

A schematic of the LSP process (left) and a photograph of the LSP process (right)

2. Methodology and results

This research has been conducted in the context of AM of Ti-6Al-4V by the selective laser melting (SLM) process. There is currently substantial development of the SLM process within South Africa and the CSIR National Laser Centre with a strong focus on Ti-6Al-4V due to significant interest from the aerospace and biomedical sectors. In order to obtain optimal mechanical performance in terms of fatigue, it is anticipated that AM components implemented in the aerospace industry will be in a machined state in order to adhere to tight manufacturing tolerances, and to improve the surface finish which is known to affect fatigue performance. The LSP research is therefore primarily on a machined AM surface.

2.1 Experimental approach

SLM has been used to produce samples of 30 x 30 x 10 mm3 using an EOSINT M280 system at the Central University of Technology (CUT, South Africa) from EOS GmbH, which incorporates a fibre laser with a power of 200 W, spot size of 80 microns and power density range of ~ 40 kW/mm2. Samples have been stress relieved and are to be machined. The LSP processing is to be performed at the CSIR National Laser Centre on an in-house developed processing platform which incorporates an Nd:YAG pulsed nano-second laser operating at 1064 nm. A thin water layer is used as inertial confinement, and LSP parameters such as power intensity and coverage were first optimised on wrought Ti-6Al-4V plate using a deflection based technique referred to as an Almen strip approach. Preliminary residual stress analysis has been performed using a SINT MTS3000 incremental hole drilling instrument in order to evaluate the through thickness stress field due to LSP processing. Residual stress analysis using X-ray diffraction will also be conducted using a Proto iXRD in order to evaluate the surface effect.

2.2 Discussion of initial results

The initial residual stress results showing an in depth profile of stresses within the AM coupon (after stress relieving) before and after application of the LSP process is shown in Figure 2. As expected, the residual stresses within the AM coupon after stress relaxation are very low. It is clear that the LSP process has effectively introduced beneficial compressive residual stresses to a depth of almost 1 mm in the SLM build Ti-6Al-4V coupon.

THE POTENTIAL ENHANCEMENT OF COMPONENTS PRODUCED BY METAL ADDITIVE MANUFACTURING USING LASER SHOCK PROCESSING continued

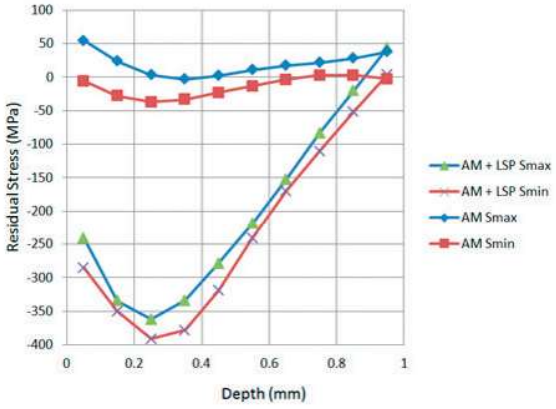


Figure 2

Residual stresses obtained by the incremental hole drilling technique before and after application of the LSP process to an SLM Ti-6Al-4V coupon

3. Conclusion

Preliminary results indicate that the LSP process may be an effective technique in order to introduce beneficial compressive residual stresses into high performance materials such as Ti-6Al-4V. Further analysis will include comprehensive residual stress analysis using the X-ray diffraction technique.

REFERENCES

[1] **ASTM.** 2012. F2792–12e1 Standard terminology for additive manufacturing technologies [Online] [7 July 2017]. Available from: www.astm.org/Standards/F2792

[2] **Ding, K., Ye, L.** 2006. *Laser shoch peening performance and simulation,* Woodhead Publishing Limited, Cambridge, England.

[1*] *National Laser Center, CSIR, South Africa(dglaser@csir.co.za)*

[2] *School of Mechanical, Industrial and Aeronautical Engineering, University of the Witwatersrand, South Africa*

The Potential Enhancement of Components Produced by Metal Additive Manufacturing using Laser Shock Processing

D. Glaser[1*], S.N. van Staden[2], N. Ivanovic[2] & C. Polese[2]

[1*] National Laser Centre, Council for Scientific and Industrial Research, South Africa
DGlaser@csir.co.za
[2] Department of Mechanical, Industrial and Aeronautical Engineering, University of the Witwatersrand, South Africa

Additive Manufacturing (AM) of high performance alloys such as Ti-6Al-4V potentially allows for improved component design and manufacturing, and is of specific interest to the aerospace industry due to enhancements in final geometry, weight, and even cost. Potential applications of metal AM components would offer a performance enhancement compared to conventional manufacturing techniques, therefore the use of a final surface enhancement process to provide further performance improvements may be highly beneficial to achieve superior components. The use of Laser Shock Processing is explored as a potential technology in order to generate beneficial compressive residual stresses into metal AM components. This investigation focuses on a stress relieved and machined AM surface, where preliminary investigations based on laboratory X-Ray Diffraction (XRD) and deflection coupons (Almen strips) were used to identify LSP process parameters for "with" and "without" (LSPwC) a protective coating. The incremental hole-drilling technique for non-uniform residual stress measurements reveals that the LSP process effective introduced high magnitude compressive residual stresses to a depth of around 0.75 mm in AM Ti-6Al-4V.

1. INTRODUCTION

Additive Manufacturing (AM) is a general term used to describe methods of building articles directly from a computer model. Typically, AM products are built up layer by layer to produce a complete or near net shaped component [1]. The AM process is specifically attractive for the manufacturing of high-value metal components as the geometric flexibility from a design and manufacturing perspective offers potential benefits in overall component performance in terms of weight and production costs. There is currently significant interest in the aerospace industry regarding the use of AM for component production, due to the perpetual pursuit of the aerospace industry to deliver components with reduced weight and improved performance at lower cost whilst maintaining high reliability [2]. Since a large drive to develop metal additive manufacturing technology is based on the requirement for superior component performance, the consideration of potential enhancements due to post-processing techniques is a vital consideration for successful technology adoption [3].

Peening technology is a well-established technique in order to enhance the mechanical performance of metal components by introduction of beneficial compressive residual stresses [4]. Crack-based failure phenomena such as fatigue or stress corrosion cracking can be drastically affected by the presence of residual stresses [5]. Essentially cracks initiate and propagate under tensile stresses, therefore the introduction of compressive residual stresses into the surface of the component can lead to significant performance enhancements.

Laser Shock Peening or Laser Shock Processing (LSP) is one of the most advanced forms of peening technology with superior performance compared to conventional techniques such as mechanical Shot Peening (SP) [6]. Typically the depth of compressive residual stresses achievable by with LSP technology are on a millimeter range (often 10 times deeper than

[1*] Corresponding author

conventional SP) with less surface roughness introduced. The implementation of LSP to high value components can result in order of magnitude life enhancements in terms of fatigue performance.

The schematic in Fig. 1 illustrates the LSP process mechanism which uses a pulsed laser beam in order to generate a high pressure plasma expansion on the component surface. A laser pulse with a short duration (typically 5-30 ns) is focused toward the metal target to achieve power intensities in the rage of GW/cm^2 [7].The high irradiance leads to near instantaneous ionization of the surface which produces a plasma at the target surface. The plasma reaches Giga-Pascal magnitudes in a nano-second time frame which drives a shock wave through the metal work-piece with sufficient strength to yield the metal and hence generate beneficial compressive residual stresses through the target surface [8]. It should be noted that an inertial confinement medium (typically water) is essential to the LSP process. When the plasma expansion occurs within a high density medium transparent to the laser irradiation, the pressure delivered to the target is enhanced by an order of magnitude, which enables yielding of high strength materials.

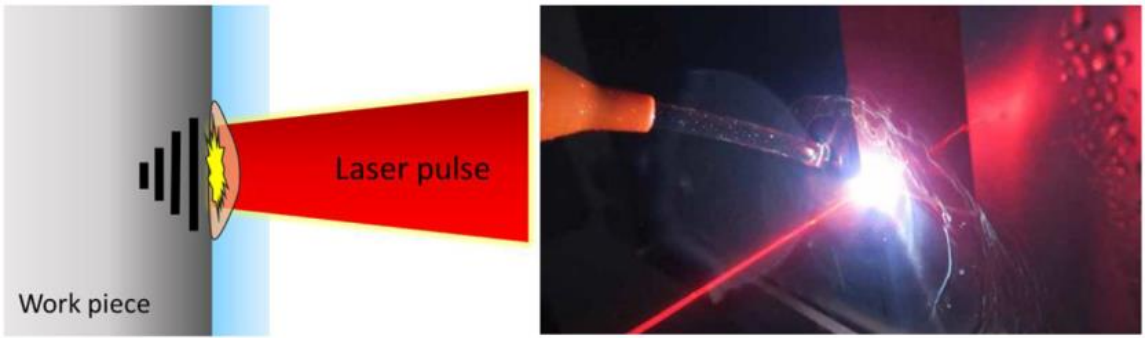


Figure 1: A schematic of the LSP process (left) and a photograph of the LSP process (right).

There are two primary variants of the LSP process. The first commercial applications of the technology were developed whereby a thermal sacrificial ablative coating is used in order to preserve the surface integrity of the component [9]. A temporary coating such as a PVC or aluminium tape may be used in order to protect the surface from the thermal effects of the laser. When a coating is used, the shockwave propagates through the protective medium into the workpiece and the process is essentially a completely non-thermal, cold-working process. A number of sequential applications of tape and LSP may be applied successively, where typically 1-3 sequential applications of LSP with tape layers are used [10].

Alternatively, the LSP process may be applied directly to the metal surface whereby the laser interacts directly with the target material. This form of the process is referred to as Laser Shock Peening without a protective coating (LPwC or LSPwC). The application of LSP without a coating was developed by Toshiba for applications of nuclear reactor maintenance, and it was found that despite the surface ablation, high magnitude compressive residual stresses may still be achieved provided that high overlap is utilized [11]. Essentially, the LSPwC process requires a large number of repetitive pulses in order for the thermal effects to be dominated by the mechanical impulses generated in order to achieve surface compressive residual stresses [12].

Both types of LSP may be attractive to the AM process as each approach has various advantages and disadvantages. When a coating is used, the surface integrity is typically completely preserved with no heat affected zone or surface roughness introduced. However, the application of the sacrificial overlays can be limiting for highly complex 3D geometries, and specifically for an as built AM surface, the adhesion of the tape under GPa shock loading conditions may be problematic due to poor adhesion on the rough as build finish [13]. Due to tape integrity considerations, a low overlap is used to prevent tape failures during processing. Typically increasing the number of impacts by increasing overlap

can increase the depth and magnitude of the resulting residual stresses. For LSP with a coating, sequential applications of the coating and the LSP process are applied (typically up to 3).

The LSPwC process may potentially be more suitable to small geometric features, however a larger number of impacts are required to achieve the desired surface compressive residual stresses. In addition, each laser pulse directly ablates the target surface which results in minor surface roughening and a modified surface due to exposure to the plasma. Since residual stresses are of course a significant concern during the SLM process [13-16], it is therefore expected that a component build would first a stress relief to eliminate detrimental tensile residual stresses. Regarding LSP in the context of AM, Zabeen et al. (2016) have investigated the use of LSP with a coating on as-built AM Ti-6Al-4V, however adhesion of the coatings to the as-built surface proved problematic under shock loading [17]. Kalentics et al. (2017) have investigated the use of LSPwC applied to SLM produced 316L in the as-built state [18] which was shown to develop compressive stresses with depth.

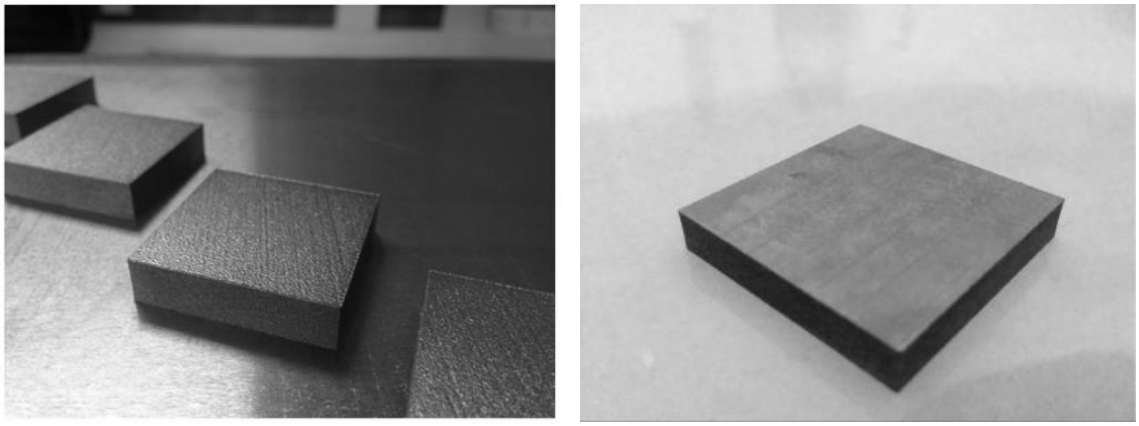
2. METHODOLOGY AND RESULTS

This research has been conducted in the context of Additive Manufacturing of Ti-6Al-4V by the Selective Laser Melting process. There is currently substantial development of the SLM process within South Africa and the CSIR National Laser Centre, with a strong focus on Ti-6Al-4V due to significant abundance of titanium minerals and drive toward value added processes [19]. In order to obtain optimal mechanical performance in terms of fatigue, it is anticipated that immediate applications of AM components implemented in the aerospace industry will be in a machined state in order to adhere to tight manufacturing tolerances, and to improve the surface finish which is known to affect fatigue performance. The LSP research is therefore primarily on a machined AM surface.

2.1 Materials and Methods

2.1.1 AM Sample preparation

Selective Laser Melting has been used to produce samples of 35 x 35 x 8 mm using an EOSINT M280 system at the Central University of Technology (CUT, South Africa) from EOS GmbH which incorporates a fiber laser with a power of 200 W, spot size of 80 microns and power density range of $\sim$ 40 kW/mm^2. The samples were first stress relieved, and then removed from the base plate by wire EDM cutting. The top surface (of 35 by 35 mm) was then machined using an AMCO XH7132A CNC milling machine with a 12 mm diameter endmill at 240 RPM with flood coolant to remove around 0.5 mm by climb milling with an federate of 48 mm/min and cut width of 5 mm. The samples were then each polished using an SiC P#1200 (US#600) grinding paper so that the final surface roughness is within Ra of 0.2 microns which is necessary for the research to extend to future fatigue tests as per the ASTM E466 specification [20]. The samples are depicted in Fig. 2 below.



As built

Stress relieved, wire cutting
+ Machining

Figure 2: Photographs of the samples after Additive Manufacturing (left), and after coupon preparation to a final machined surface (right).

2.1.2 LSP Processing

The LSP processing has been performed at the CSIR National Laser Centre on an in-house developed processing platform which incorporates a Spectra-Physics Quanta-Ray Pro series Nd:YAG pulsed nano-second laser operating at wavelength 1064 nm. A thin layer of de-ionized water is used as inertial confinement applied with a water spray nozzle as depicted in Fig. 1. LSP parameters such as power intensity and coverage were first optimized on wrought Ti-6Al-4V plate using a deflection based technique referred to as an Almen strip approach. The Almen strips were laser cut 1.2 mm thick Ti-6Al-4V plate to the standard designation dimensions of 19.05 mm by 76.2 mm. Verification of LSP on wrought Ti-6Al-4V plate was then conducted by processing samples of 100 by 100 mm by 6 mm with 10 by 10 mm LSP patches applied without a protective coating.

The LSP processing was performed both with and without a sacrificial thermal protective overlay. Essentially, the results described in section 2.2.1 and 2.2.2 of LSP of deflection coupons and on wrought Ti-6Al-4V are regarding the selection of an appropriate LSP parameter combination to be applied to the AM coupons. The coverage of the LSP processed area is achieved by a raster type pattern as depicted in the schematic in Fig. 3. The laser pulse repetition rate is fixed at 20 Hz, therefore control of the scan speed (x direction), and step dimension (y direction) can be used to control the spot to spot placement, which is quoted in terms of number of spots per mm^2 (Np). The Np for the high and low coverage used for processing performed with and without a protective coating is depicted in the schematic in Fig. 3.

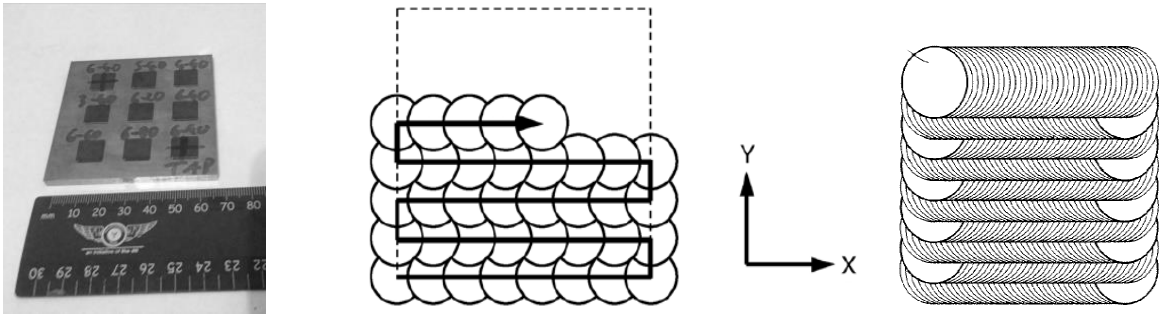
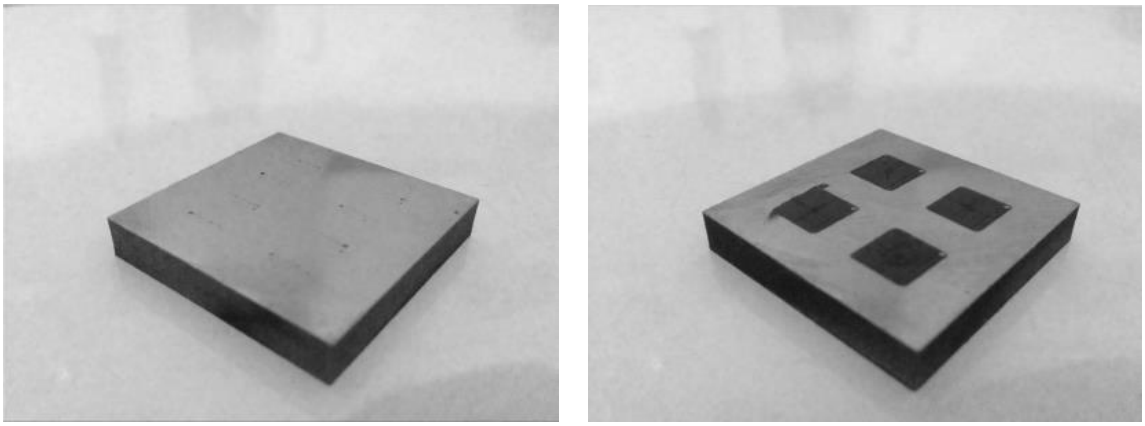


Figure 3: A photograph of preliminary phase LSPwC processing of wrought titanium plate (left), and a schematic of a low and high overlap rater pattern to achieve spot coverage (center and right).

The final parameters selected for LSP with a coating was a power intensity of 8 GW/cm^2, and coverage of 2 spots per mm^2 for a 1.2 mm spot diameter. A black PVC tape coating of around 100 microns thick with a 30 micron adhesive backing was selected. For LSP with a coating, the coverage is required to be low in order to preserve the tape integrity and adhesion to the surface during processing. Therefore to increase the local number of impacts, 3 sequential treatments were applied (where the coating is removed between each). The parameters for the LSP processing performed without a protective also utilized a power intensity of 8 GW/cm^2, but with a smaller spot size of 0.8 mm, and a higher spot overlap of 40 spots per mm^2. Photographs of the AM coupons after LSP processing both with and without a protective coating are depicted in Fig. 4. LSP processing was applied to produce 4 equi-distant LSP patches of 7 mm by 7 mm on the 35 mm by 35 mm AM coupon face. The LSPwC surface is clearly apparent as dark patches due to the direct laser-material interaction.



Stress relieved, wire cut
+ Machining
+ Polish
+ 3 Layers of LSP with coating

Stress relieved, wire cut
+ Machining
+Polish
+ LSP without coating (LSPwC)

Figure 4: Photographs of the AM samples after LSP applied with (left), and without a protective coating (right) with the relevant sample preparation details.

2.1.3 Surface Roughness

Surface roughness measurements were conducted using a MahrSurf PS1 touch probe surface profilimiter with trace lengths of 17.5 mm with an Lc of 2.5 (n=5). For each sample, 5 x line scans were performed at approximately 3 mm spacing, and the reported values are the mean of the 5 measurements.

2.1.4 XRD Residual Stress Analysis

The residual stress analysis was performed using conventional laboratory X-Ray diffraction (XRD) measurements using a Proto iXRD (Proto Manufacturing Inc., Taylor, Michigan USA) instrument. A Cu-Kα X-ray source with a wavelength of 1.5418 Å was used with a round 2.0 mm aperture. Reflections from the 213 peak for the Ti-6Al-4V were used with a goniometer range of ± 20 degrees with a 3 degree oscillation. The measurements were performed as per the $\sin^2\psi$ technique, whereby 20 exposures of 4 seconds each were used for 7 measurement angles per strain measurement. Tri-axial measurements were performed at 0, 45, and 90 degrees in order to obtain the principle stresses. For both the wrought and AM built Ti-6Al-4V, stresses were calculated using the X-ray Elastic Constants of $-S_1 = 2.83 \times 10^{-6}$ MPa^{-1} and $1/2S_2 = 11.89 \times 10^{-6}$ MPa^{-1}.

2.1.5 Incremental Hole-Drilling Residual Stress Analysis

The incremental hole-drilling has been performed using a SINT MTS3000 incremental hole drilling instrument which uses a high speed end mill. The hole drilling analysis has been conducted in order to obtain insight into the residual stresses within the coupons. Tungsten carbide cutters with a TiAlN coating (SINTCTT/1) have been used to effectively drill the titanium. The CEA-13-062UL-120 gauges have been used which have a nominal hole diameter of 2 mm, therefore allowing for computation of stresses to up to 1 mm deep. The data computation is performed using the Restress Eval software where the assumed material properties for the materials is E = 113 800 MPa, Sigma Y = 1000 MPa, V = 0.34. The drilling was performed with 60 increments of 0.02 mm each, and the reported stresses are as per the ASTM E837-13 EXT formulation for non-uniform residual stresses. The computed data is based on 20 linear steps of the interpolated strains, whereby the Tikhonov regularization has been applied. Since the incremental hole-drilling technique is considered a semi-destructive technique whereby execution of the tests is known to affect certainty of the measurements, at least two repeatability trails have been conducted for each test.

2.2 Results and Discussion

The purpose of the LSP processing and analysis of the Almen strips and the wrought titanium was to isolate a LSP parameter combination for the LSP process both with and without a protective coating. This is crucial since the LSP infrastructure used to perform the LSP process is an in-house LSP R&D platform that is still under development, and has not yet been industrialized.

Regarding LSP processing parameters, the peak pressures generated are proportional to the power intensity in terms of GW/cm^2. However, beyond a particular threshold, saturation effects occur due to plasma shielding, whereby plasma generated within the beam path absorbs incident laser irradiation [21]. Industrialized LSP processing typically does not exceed a power intensity of 10 GW/cm^2, as this is the saturation threshold typically found at 1064 nm [22]. Shock processing of titanium typically requires the highest possible pressure to be developed at the surface, as under shock pressures materials such as Ti-6Al-4V experience an increase of their effective dynamic yield strength (known as the Hugonoit Elastic Limits) by as much as 100% [23]. The preliminary Almen strip approach and processing of wrought material was performed to verify that the CSIR LSP processing platform could operate effectively near the typical saturation power intensity of 10 GW/cm^2 for 1064 nm radiation.

2.2.1 LSP Deflection Coupons

Almen strips are simply standard material coupons that were developed for the conventional Shot Peening industry in order to quantify process intensity and an appropriate peening time. Conventionally, an Almen strip is peened and will produce a convex deflection due to the plastic deformation that has been introduced into the surface.

Plotting the Almen arc height deflections with increasing processing time is used in order to determine the saturation curve which enables conventional peening to determine an appropriate peening time by the definition of saturation which states a less than 10% change for twice the peening time [24].

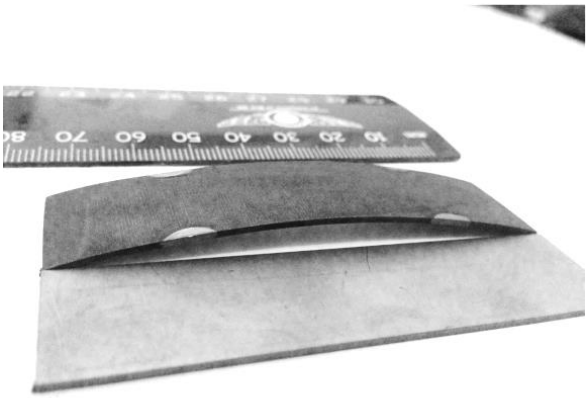


Figure 5: A photograph a LSPwC processed 1.6 mm thick Ti-6Al-4V Almen strip showing convex curvature (compared to a flat unprocessed strip in the foreground).

Almen strips have been incorporated into the LSP AMS-2546 standard for process control and repeatability, however the South African LSP group have also found the technique useful in order to compare preliminary LSP parameters. Specifically, the technique is useful to determine if power intensity saturation has occurred, as beyond the saturation point, the measured deflections will no longer increase due to an effectively maximum pressure developed. In addition, for a fixed LSP power intensity the deflections can be plotted against coverage (effectively peening time) to ensure that material saturation effects have not been reached.

The Almen strip results are shown in Fig. 6. In Fig. 6 (left), the arc height deflections are plotted against power intensity for both LSP with and without a protective coating. For these tests a fixed coverage of 2.5 spots per mm^2 was used with a spot diameter of 0.8 mm. It is clear that operating up until 8 GW/cm^2 does not produce any power intensity saturation effects (which would show a decreased deflection despite increased power intensity). Since 10 GW/cm^2 is typically the limit of the LSP process, 8 GW/cm^2 has been selected to ensure that processing is performed below the power intensity saturation point.

The results in Fig. 6 (right) show the arc height deflections for LSPwC for increasing coverage at 8 GW/cm^2. It is clear that even at 40 spots per mm^2, the saturation point has not yet been reached. In terms of typical LSP processing parameters, Toshiba successfully commercialized LSPwC using the same spot size of 0.8 mm and coverage of 40 spots per mm^2 applied to SUS304 however at a wavelength of 532 nm. The Almen strip deflections reveal that a coverage of Np = 40 spots per mm^2 does not exhibit material saturation effects due to cyclic impacts.

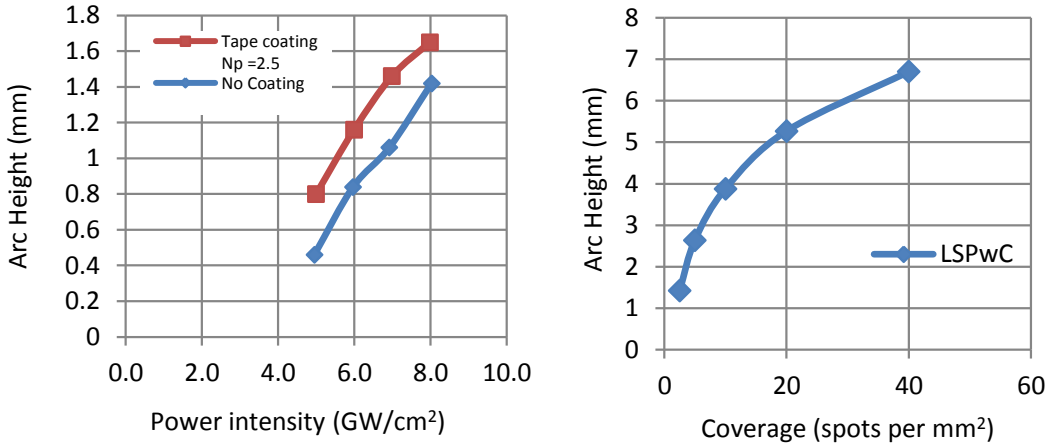


Figure 6: Almen strip deflections of 1.6 mm thick Ti-6Al-4V coupons to evaluate power intensity (left), and coverage (right).

2.2.2 LSP on Wrought Ti-6Al-4V

One of the challenges regarding the development of the LSPwC process (i.e. no coating), is that if the parameters are not correct (in terms of power intensity, spot size, and coverage), then the direct laser-material interaction may produce superficial tensile residual stress due to the thermal effect of the plasma generated at the material surface (which can be seen in Fig. 1). Since the time scale of events are short (due to the nano-second laser pulse durations), the thermal events are extremely rapid with little time for thermal conduction into the material. Typically, it is only the first few microns that are affected by the plasma generated; however a tensile residual stress on the surface can be highly detrimental for a peening process.

LSP processing of 10 mm by 10 mm areas with different LSP parameter combinations were performed as an initial process development approach to ensure that surface compressive residual stresses are generated. The principle stresses for variation of power intensity and spot coverage are shown in Fig. 7 for LSPwC. Fig. 7 (right) shows that increasing power intensity leads to an increase in the compressive stresses generated. Fig. 7 (left) shows that in the range of 20 to 80 spots per mm^2, compressive residual stresses are generated. The maximum compressive stress was achieved for Np = 40 spots per mm^2, however increasing the coverage is seen to increase the compressive state of the Smax as well.

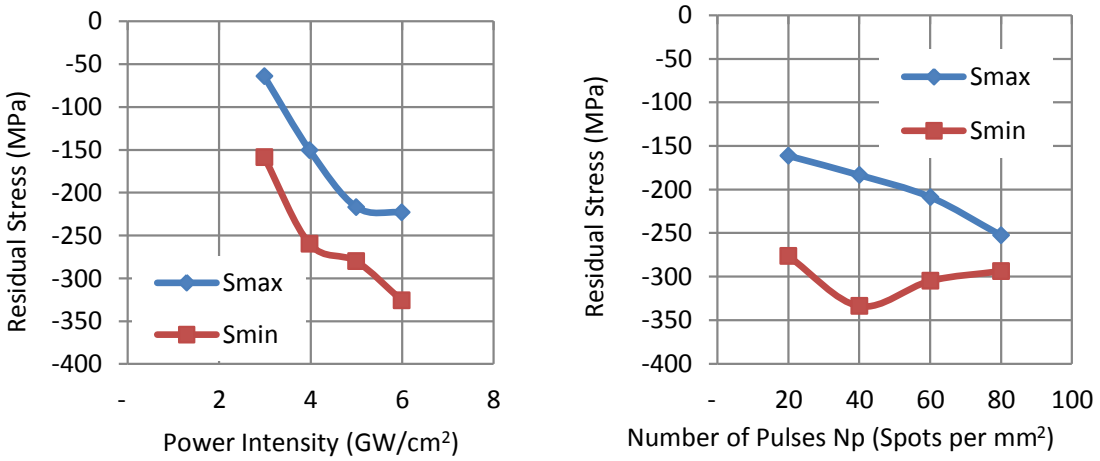


Figure 7: Principle stresses for LSPwC applied to wrought Ti-6Al-4V plate in order to evaluate the effect of power intensity (left) and coverage (right).

The principle stresses shown in Fig. 7 have the minimum (Smin) component aligned to the stepping direction of the LSP raster pattern (indicated as y in Fig. 3). It should be noted that the stress results depicted in Fig. 7 are highly superficial as the laboratory X-Ray radiation only penetrates around 2.5 microns for Ti-6Al-4V. Although there seems to be little variation of the minimum principle stress for increasing the number of spots, there is most likely to be an effect within the depth of the material, whereby deeper levels of compression are expected for increased overlap.

2.2.3 LSP on Machined AM

This investigation is focused toward the application of the LSP process to machined AM Ti-6Al-4V components as it is expected that the first potential applications of LSP technology in the context of high-value AM components would be for a machined surface. Particularly in the aerospace industry, a concern for fatigue for a high-value, complex AM components would most likely have a machined surface due to the known detrimental effect on fatigue crack initiation associated with the as-built surface roughness.

The results in Fig. 8 show the surface residual stress measurements by X-Ray diffraction. The AM sample after stress relieving and removal from the build plate exhibits low level tensile residual stresses which are almost zero which is as to be expected from a stress relieved coupon. The effect of the machining alone can be seen to introduce significant residual stresses on the surface. The machining induced residual stresses are due to a combination of thermal effects and plasticity introduced. The beneficial compressive nature of the stresses introduced suggests that the thermal effects were minimal. Whilst the machining certainly introduced high levels of compressive residual stresses into the surface, these are most likely to be highly superficial, and not exist to significant depths below the surface.

After the application of LSP with a coating (3 consecutive layers), both principle stress components remain in a high level of compressive residual stress. After the direct application of the LSPwC process, the surface is still under compressive residual stress, however a reduction in magnitude is apparent, which is due to the thermally affected surface which consist of re-cast layer after rapid ablation and surface melting occurs during plasma formation during processing.

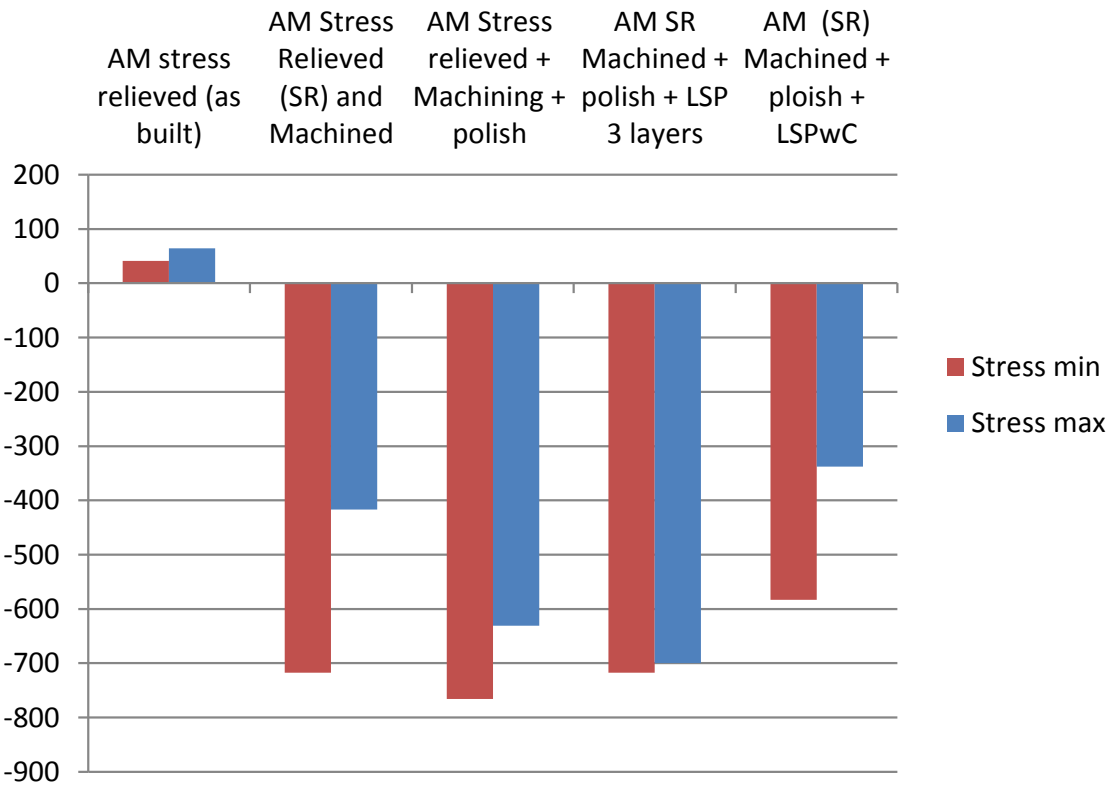


Figure 8: X-Ray diffraction principle residual stresses for different AM surface conditions.

Since the XRD results only provide insight into the very extreme surface condition, the incremental hole-drilling technique as per the ASTM E837-13 has been implemented in order to evaluate the LSP through the material thickness. The incremental hole drilling technique is considered a semi-destructive technique where the guideline state that the largest factors to uncertainty are instrument-to-operator skill [25]. Each measurement has therefore been completed at least twice in order to evaluate the repeatability, and therefore uncertainty of the measurement. The repeat tests for samples with and without a coating are shown in Fig. 9. Both tests (A) and (B) for the sample with a coating, and tests (C) and (D) for LSPwC show reasonable overlap between successive measurements which indicates repeatability of the measurement technique.

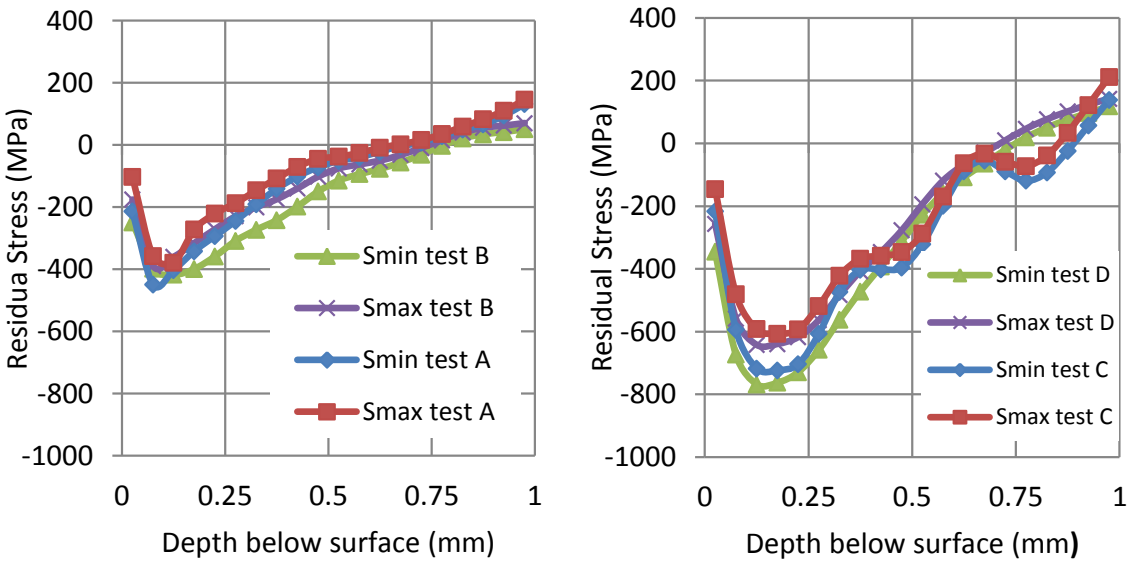


Figure 9: Principle stresses by incremental hole drilling for two repeat tests for LSP with a coating (left) and LSPwC (right).

The comparison between in depth residual stress profiles is provided in Fig. 10. Firstly, it can be seen that the stress relieved, as-built coupons after machining and polishing still have rather low compressive residual stresses within the bulk of the coupons. The compressive residual stresses introduced by the two approaches (with and without a coating) are both seen to extend to around 0.75 mm within the material. However, the LSPwC processing produces far higher magnitudes of compressive stresses, with a peak compressive stress around twice that achieved compared to LSP with a coating.

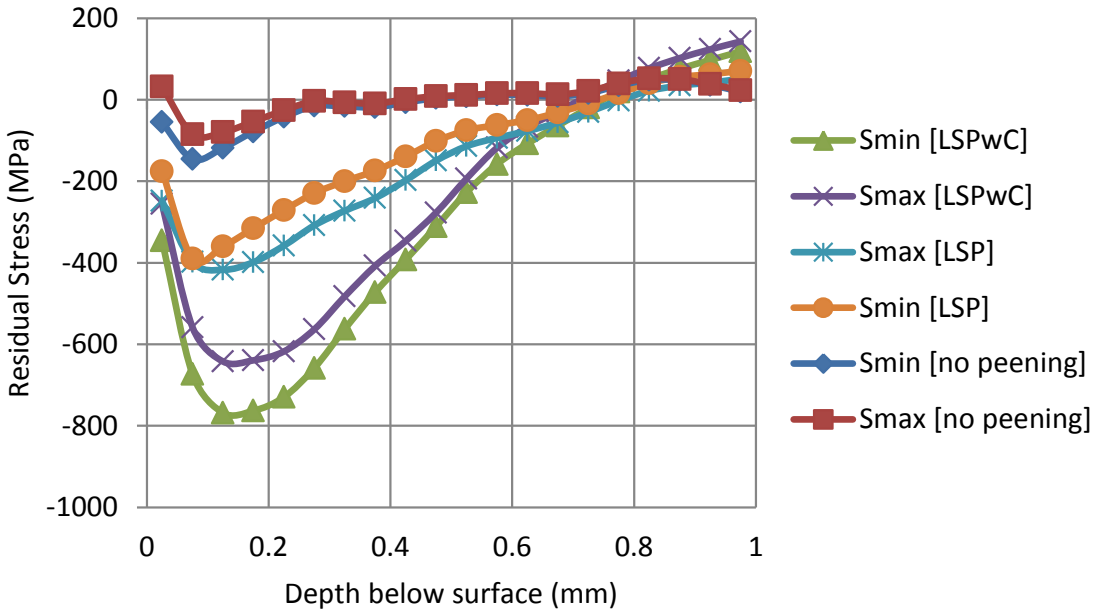


Figure 10: A comparison of the incremental hole drilling residual stress results for the untreated samples, and samples LSP processed with and without a protective coating.

From the Almen strip data shown in Fig. 6, for the exact same LSP processing parameters, the use of a thermal protective coating produces higher arc height deflections, suggesting a higher impact pressure is delivered when a coating is used (possibly due to the lower ionization threshold compared to titanium). Although both LSP processing parameters used for samples with and without a coating both used 8 GW/cm^2 (which directly relates to the impact pressure), the samples without a coating had a larger spot size of 1.2 mm compared to 0.8 mm for LSPwC. The significant difference between samples with and without a protective coating is the number of impacts seen locally. For LSPwC, the impacts seen per local spot on the surface are equivalent to 25.6, whilst the 3 sequential layers of LSP with a coating equate to 8.64 impacts per spot. The almost 3 x higher local number of impacts for the LSPwC process therefore effectively drives higher magnitude compressive residual stresses within the material.

The incremental hole-drilling results prove to be rather promising as is evident by the depth and magnitude of compressive residual stresses achieved. However, these results do not compare well to the laboratory XRD. For example, both the samples before LSP processing and after LSP processing with a protective coating reveal minimum principle surface stresses in the range of -700 MPa, however the hole-drilling indicates a maximum compressive stress of only -350 MPa. The incremental hole-drilling technique is specifically unreliable for near surface resolution, especially where steep stress gradients may be present. The drilling steps were performed at increments of 20 microns. The high levels of compression shown with the XRD would be averaged over the depth increments, which may be very shallow. The fact that even the hole-drilling results before LSP (as seen in Fig. 10) do not indicate any high compressive stresses suggests that the machining and polishing induced compressive residual stresses are very shallow, where a sharp stress gradient may exist.

As mentioned, one of the drives toward investigation of LSP on a machined surface was due to the expected machining to remove significant surface roughness inherent in the AM as-built surface. The surface roughness results are shown in Fig. 11, which illustrates the high Ra and Rz for the as-built coupons as expected. The final surface finish before LSP processing was within Ra of 0.14 microns. Due to the ablation effect of LSPwC, there is some surface roughness introduction compared to a polished surface, however an Ra of 2.28 is still an improvement compared to the as-built surface state.

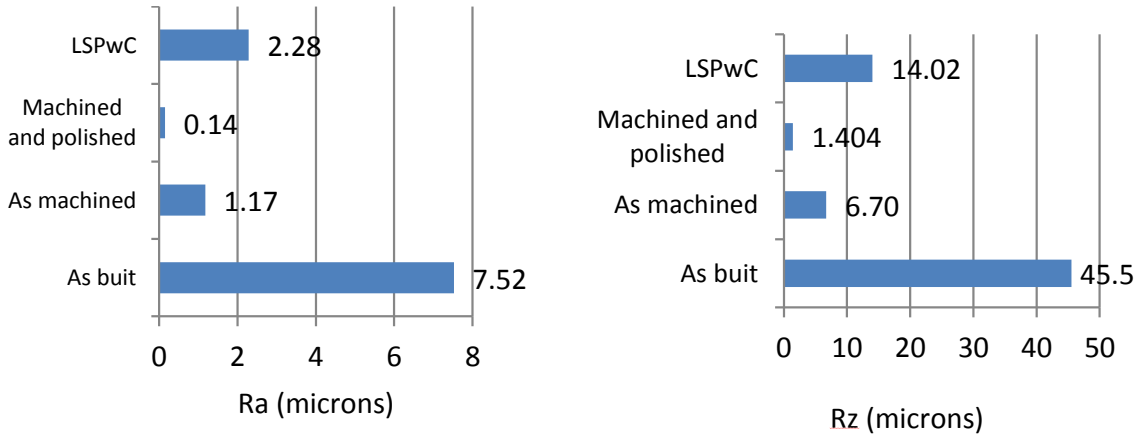


Figure 11: Surface roughness in terms of Ra (left) and Rz (right).

From a technology industrialization perspective, after each LSP coating, the sacrificial coating must first be removed, the component dried (as water from processing will prevent effective coating adhesion) before the next sacrificial coating is applied before shock processing. It is therefore not practical to perform this a large number of times (typically this is performed 1-3 times by commercial LSP service providers). The LSPwC processing is

therefore highly attractive, except for the fact that surface oxidation is produced (as evident by the discoloration seen in Fig. 3 and 4) as well as a highly superficial thermally affected zone in the first few microns due to exposure to the high temperature plasma. Although the LSPwC process can be used effectively with the as-processed surface, future work will need to focus on quantification of the surface alteration due to the thermal effect associated with the LSP plasma. Potential additional future work should consider application of the LSPwC to the as-built surface first, with final machining to simply remove the AM surface roughness and LSPwC surface effect.

3. CONCLUSIONS AND RECOMMENDATIONS

This investigation explored the use of LSP with and without a thermal protective coating for applications in the context of machined Ti-6Al-4V produced by Selective Laser Melting. The first phase focused on identification of suitable LSP process parameters, which was conducted using a coupon deflection based technique (Almen strips), and application of LSPwC to wrought Ti-6Al-4V plate material. The laser power intensity selected was 8 GW/cm^2, where the overlap for the use of a thermal protective coating was kept low (Np = 2 spots per mm^2) in order to maintain coating integrity. The Np of 40 spots per mm^2 was selected based on surface compressive stresses measured by X-Ray Diffraction. The following conclusions regarding LSP in the context of application to machined Ti-6Al-4V by AM:

- Machining introduces highly superficial compressive residual stresses of high magnitude.
- LSP with and without a coating both produced compressive residual stresses to a depth around 0.75 mm in AM stress relieved coupons.
- The LSPwC process produced significantly high magnitude compressive stresses with depth compared to LSP with a coating due to the higher local number of impacts (≈3x).

Due to the significantly enhanced magnitudes of compressive stresses found for LSPwC compared to LSP with a coating, future work should focus to enhance the ability to generate high magnitude compressive stresses with depth when a coating is used without significant increase in overlap. Additional work should include detailed quantification of the surface alteration (such as oxidation) for the LSPwC process. Alternatively, the LSPwC process should be explored potentially before final machining to avoid actual material constituent modifications to final components.

4. REFERENCES

[1] **ASTM**, 2012. F2792–12e1 Standard terminology for additive manufacturing technologies, available from: www.astm.org/Standards/F2792

[2] **Williams, J. C., & Starke, E. A**. 2003. Progress in structural materials for aerospace systems, Acta Materialia, 51(19), 5775-5799.

[3] **Edwards, P. and Ramulu, M**. 2014. Fatigue performance evaluation of selective laser melted Ti–6Al–4V. Materials Science and Engineering: A, 598, pp.327-337.

[4] **Ding, K., Ye, L.** 2006. Laser shock peening performance and simulation, Woodhead Publishing Limited, Cambridge, England

[5] **Withers, P.J. 2007.** Residual stress and its role in failure. Reports on progress in physics, 70(12), p.2211.

[6] **Kulekci, M.K. and Esme, U.** 2014. Critical analysis of processes and apparatus for industrial surface peening technologies. *The International Journal of Advanced Manufacturing Technology*, *74*(9-12), pp.1551-1565.

[7] **Montross, C.S., Wei, T., Ye, L., Clark, G. and Mai, Y.W.** 2002. Laser shock processing and its effects on microstructure and properties of metal alloys: a review. *International Journal of Fatigue*, *24*(10), pp.1021-1036.

[8] **Peyre, P., Fabbro, R., Berthe, L. and Dubouchet, C.** 1996. Laser shock processing of materials, physical processes involved and examples of applications. *Journal of Laser Applications*, *8*(3), pp.135-141.

[9] **Peyre, P., Carboni, C., Forget, P., Beranger, G., Lemaitre, C. and Stuart, D**. 2007. Influence of thermal and mechanical surface modifications induced by laser shock processing on the initiation of corrosion pits in 316L stainless steel. *Journal of Materials Science*, *42*(16), pp.6866-6877.

[10] **Metal Improvement Company.** 2008. Recent Developments in large scale industrial peening. Paper presented *The first International Conference on Laser Peening*, Houston Texas,USA.

[11] **Sano, Y., Obata, M., Kubo, T., Mukai, N., Yoda, M., Masaki, K. and Ochi, Y**. 2006. Retardation of crack initiation and growth in austenitic stainless steels by laser peening without protective coating. *Materials Science and Engineering: A*, *417*(1), pp.334-340.

[12] **Akita, K., Tanaka, H., Sano, Y. and Ohya, S.I**. 2005. Compressive residual stress evolution process by laser peening. In *Materials Science Forum* (Vol. 490, pp. 370-375). Trans Tech Publications.

[13] **van Zyl, I., Yadroitsava, I. and Yadroitsev, I.** 2016. Residual stress in Ti6Al4V objects produced by direct metal laser sintering. *South African Journal of Industrial Engineering*, *27*(4), pp.134-141.

[14] **Knowles, C.R., Becker, T.H. and Tait, R.B.** 2012. Residual stress measurements and structural integrity implications for selective laser melted Ti-6Al-4V. *South African Journal of Industrial Engineering*, *23*(3), pp.119-129.

[15] **Vrancken, B., Cain, V., Knutsen, R. and Van Humbeeck, J**. 2014. Residual stress via the contour method in compact tension specimens produced via selective laser melting. *Scripta Materialia*, *87*, pp.29-32.

[16] **Zaeh, M.F. and Branner, G.** 2010. Investigations on residual stresses and deformations in selective laser melting. *Production Engineering*, *4*(1), pp.35-45.

[17] **S. Zabeen, M. M. Attallah, and M. E. Fitzpatrick**. 2016. Characterization Of Residual Stress In Additively Manufactured Ti-6Al-4V Material After Laser Shock Peening. Paper presented *The 6th International Conference on Laser Peening and Related Phenomena*, Kruger National Park, South Africa.

[18] **Kalentics, N., Boillat, E., Peyre, P., Gorny, C., Kenel, C., Leinenbach, C., Jhabvala, J. and Logé, R.E.** 2017. 3D Laser Shock Peening–A new method for the 3D control of residual stresses in selective laser melting. *Materials & Design*.

[19] **De Beer, D.J., du Preez, W. B., Greyling H., Prinsloo H., Sciammarella F., Trollip N., Vermeulen M.** 2011. A South AfricanAdditive Manufacturing Strategy. Obtained from: http://www.rapdasa.org/wp-content/uploads/2017/02/South-African-Additive-Manufacturing-Strategy.pdf

[20] ASTM E466-02. 2002. Standard Practice for Conducting Force Controlled Constant Amplitude Axial Fatigue Tests of Metallic Materials.

[21] Ready, J. F., & Farson, D. F. 2001. *LIA handbook of laser materials processing*, Orlando: Laser Institute of America. 223-262.

[22] Fabbro, R., Peyre, P., Berthe, L. and Scherpereel, X. 1998. Physics and applications of laser-shock processing. Journal of laser applications, 10(6), pp.265-279.

[23] Brockman, R.A., Braisted, W.R., Olson, S.E., Tenaglia, R.D., Clauer, A.H., Langer, K. and Shepard, M.J. 2012. Prediction and characterization of residual stresses from laser shock peening. *International Journal of Fatigue*, *36*(1), pp.96-108.

[24] SAE AMS-S-13165. 1997. Shot Peening of Metal Parts.

[25] Grant, P.V., Lord, J.D. and Whitehead, P.S. 2002. Measurement good practice guide no. 53. *UK, National Physical Laboratory*.

*Effectiveness of Laser Shock Peening in Post processing Additive Manufactured Ti–6Al–4V

Ivanovic N.[1,2], Polese C.[1,2], Yadroitsev I.[3]

[1]*School of Mechanical, Industrial and Aeronautical Engineering, University of the Witwatersrand, 1 Jan Smuts Avenue, Johannesburg, 2000, South Africa*
[2]*DST-NRF Centre of Excellence in Strong Materials, University of the Witwatersrand, 1 Jan Smuts Avenue, Johannesburg, 2000, South Africa*
[3]*Centre for Rapid Prototyping and Manufacturing, Central University of Technology, 20 President Brand Street, Bloemfontein, 9300, South Africa*

While metal additive manufacturing (Direct Metal Laser Sintering) presents the benefit of complex geometrical design, it also results in components with high residual stresses. These need to be addressed with stress relief treatment. Components still contain surface tensile residual stresses which can be detrimental to the fatigue performance [1]. Laser shock peening induces deep fatigue-beneficial compressive residual stress in the material. It is important to see the effectiveness of LSP as a post processing treatment in additive manufactured parts due to their well-established susceptibility to fatigue failure attributed to their high surface roughness.

LSP without ablative coating is to be performed on samples of AM Ti-6Al-4V in order to determine its effectiveness in inducing beneficial compressive residual stress without compromising surface integrity. Residual stress measurement will be performed using Synchrotron XRD on thinner samples and incremental hole-drilling on thicker samples. The samples will be analysed under scanning electron microscope before and after laser shock peening. Preliminary tests have shown that LSP on titanium results in significant surface oxidation as the water inertial barrier dissociates into its elements. In the presence of this oxide layer it is important to develop a method of reliable surface preparation for mounting strain gauges in samples to be measured using incremental hole-drilling. Since XRD measures stresses to a much smaller depth than incremental hole-drilling, surface treatment will not be performed on these samples in order to preserve the characteristic residual stress induce by LSP. It is also important to consider the effect the oxide layer has on XRD measurement and attenuation depth.

The study will contribute towards a further understanding of LSP on AM titanium alloy, and the challenges presented by the residual stress measurement techniques involved. The aim of the study is to learn to reliably induce compressive residual stress in critically fatigued locations in complex AM parts.

References

1. Yadroitsev, I. Residual stress in metal specimens produced by direct metal laser sintering. Bloemfontein, Free State, South Africa: Central University of Technology. (2015).

Email corresponding author: 363397@students.wits.ac.za

Effectiveness of Laser Shock Peening in Post Processing Additive Manufactured Ti–6Al–4V

N. Ivanovic[1, 2], C. Polese[1, 2], I. Yadroitsev[3], and D. Glaser[4]

[1]School of Mechanical, Industrial and Aeronautical Engineering, University of the Witwatersrand, 1 Jan Smuts Avenue, Johannesburg, 2000, South Africa

[2]DST-NRF Centre of Excellence in Strong Materials, University of the Witwatersrand, 1 Jan Smuts Avenue, Johannesburg, 2000, South Africa

[3]Centre for Rapid Prototyping and Manufacturing, Central University of Technology, 20 President Brand Street, Bloemfontein, 9300, South Africa

[4]CSIR National Laser Centre, Meiring Naudé Road, Pretoria, 0184, South Africa

363397@students.wits.ac.za

While metal Additive Manufacturing (AM) presents the benefit of complex geometrical design, it also results in components with high surface tensile residual stresses, which can be detrimental to fatigue performance. These need to be addressed with stress relief treatment. Laser Shock Peening (LSP) induces deep fatigue-beneficial compressive residual stress in the surface. It is thus important to see the effectiveness of LSP as a form of post processing in AM material. LSP without ablative coating was performed on samples of AM Ti-6Al-4V in order to determine its ability to induce compressive residual stress without compromising surface integrity. Residual stress measurement was performed using laboratory X-Ray Diffraction (XRD) on thinner samples and incremental hole drilling on thicker samples. The samples were analysed under light and scanning electron microscopes before and after LSP. Preliminary trial tests with Glaser et al. [1] have shown that LSP on titanium alloy results in surface oxidation as the water inertial barrier dissociates into its elements. In the presence of this oxide layer it is important to develop a method of reliable surface preparation for mounting strain gauges in samples to be measured using incremental hole drilling. Since laboratory XRD measures stresses to a much smaller depth than incremental hole drilling, surface preparation was not performed on these samples in order to preserve the characteristic residual stress induced by LSP. This research will contribute towards a further understanding of the use of LSP on additive manufactured titanium alloy, and the challenges presented by the residual stress measurement techniques involved.

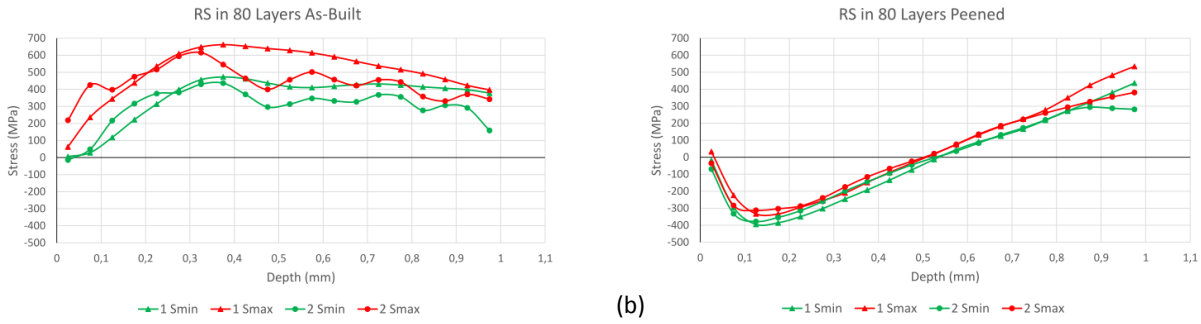


Fig. 1. Comparison of residual stress profile before (a) and after (b) LSP (incremental hole drilling).

[1] D. Glaser, S. N. van Staden, N. Ivanovic, C. Polese, "The Potential Enhancement of Components Produced by Metal Additive Manufacturing using Laser Shock Processing", 18th Annual International RAPDASA Conference, 8-10 November 2017, Durban, South Africa.

WITS UNIVERSITY

SCHOOL OF MECHANICAL, INDUSTRIAL & AERONAUTICAL ENGINEERING

7th International Conference on Laser Peening and Related Phenomena
17th - 22nd June 2018
Singapore

DST-NRF CENTRE OF EXCELLENCE IN STRONG MATERIALS

National Research Foundation

science & technology

Effectiveness of Laser Shock Peening in Post Processing Additive Manufactured Ti–6Al–4V

Nikola Ivanovic (University of the Witwatersrand, Johannesburg),
Prof. Claudia Polese (University of the Witwatersrand, Johannesburg),
Prof. Igor Yadroitsev (Central University of Technology, Bloemfontein)

Introduction

While metal Additive Manufacturing (Figure 1) presents the benefit of complex geometrical design, it also results in components with high residual stresses close to yield point. These stresses combined with a high surface roughness make AM parts particularly good candidates for fatigue failure. It is of value to industry to explore avenues of reversing these stresses to create a part with compressive stress which delays fatigue failure and extends useful service life of high-value components.

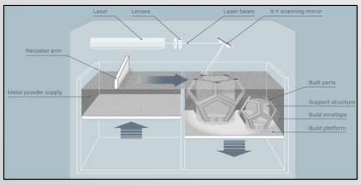


Figure 1 - Direct Metal Laser Sintering Process (DMLS)

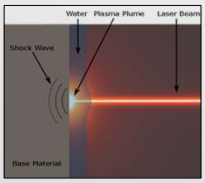


Figure 2 – LSP Process

Laser Shock Peening (LSP) utilizes an imparted shock wave to induce deep compressive residual stress in the surface of a metal (Figure 2). It is important to evaluate the effectiveness of LSP as an innovative post processing surface treatment in additive manufactured parts due to their increasingly abundant use in high-cycle fatigue loaded components in highly specialised industries like aerospace.

Experiment

AM Ti-6Al-4V square samples were manufactured at the Centre for Rapid Prototyping and Manufacturing at the Central University of Technology on a EOSINT M280 DMLS machine. LSP was performed on half of these samples at the CSIR NLC (National Laser Centre) to induce compressive residual stress.



Figure 3 – Sample Array

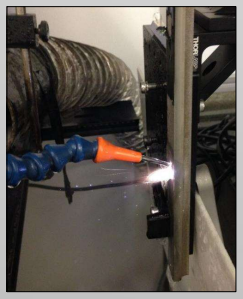


Figure 4 – LSP on Samples

Residual stress measurement was performed using Laboratory XRD (Figure 6a) at the NLC and incremental hole drilling at Wits University (Figure 7a). Surface roughness was measured to determine the effect of LSP on the surface of AM material. Metallographic analysis was performed on the samples to reveal the effect of LSP on microstructure and visualise grain deformation. The samples were analysed under microscope and tested for changes in microhardness related to the cold work done during the LSP deformation.

Results



Figure 6a – Proto iXRD MGR40

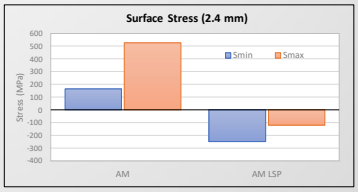


Figure 6b – Surface Stress Comparison



Figure 7a – SINT MTS3000 - Restan

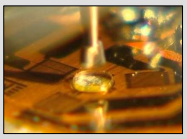


Figure 7b – Incremental Hole Drilling (close-up)

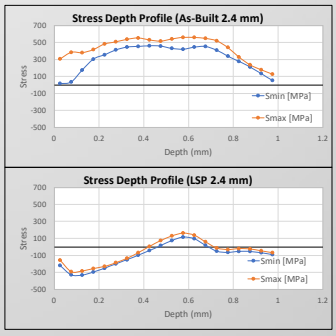


Figure 7c – Stress Depth Profiles

Figure 6b shows the stress state at the surface of a 2.4 mm thick sample in high tension after the DMLS process – up to 500 MPa. This stress was reversed after LSP treatment, and the surface was found to be at 250 MPa compression. Figure 7c shows a comparison between the depth profile of stress before and after LSP. It is seen that compression is induced to a depth of 0.4 mm, well exceeding the capability of shot peening The above results show promise in implementing LSP as a post-processing technique for AM components. The research will form a baseline for further experimentation on the topic and ultimately large scale implementation.

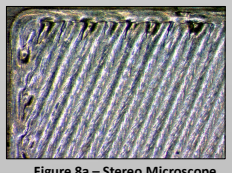


Figure 8a – Stereo Microscope Image of DMLS texture

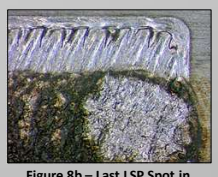


Figure 8b – Last LSP Spot in Raster Pattern

In Figure 8b it is seen that each LSP spot leaves behind a ring of superficial oxide on the surface of the metal, which (due to the raster pattern) appears on the surface as a continuous coating. This oxide is a result of the high surface temperatures and pressures involved in the process.

The above results show promise in implementing LSP as a post-processing technique for AM components. The research will form a baseline for further experimentation on the topic and ultimately large scale implementation.

Acknowledgements

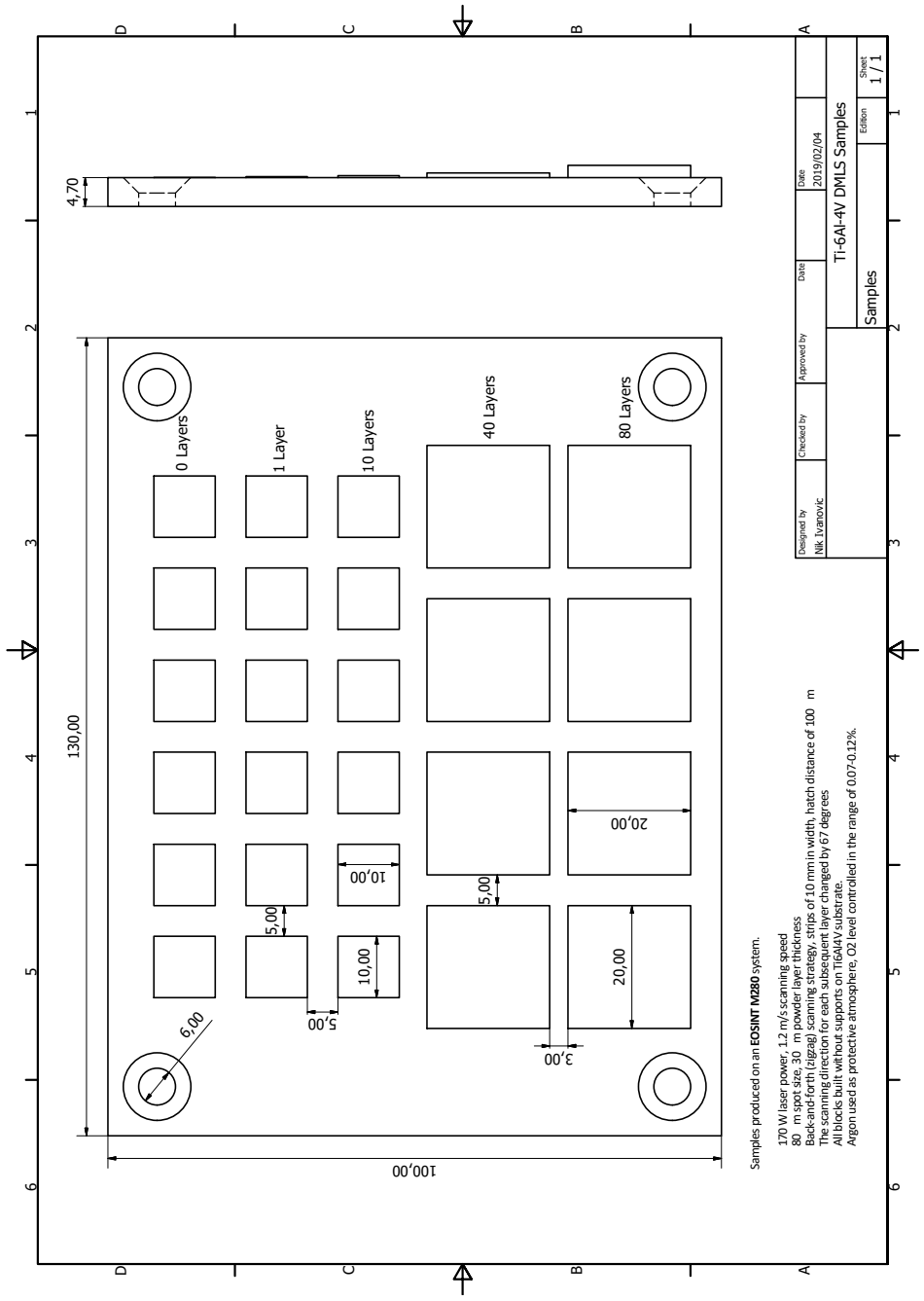
The authors would like to acknowledge the generous contribution of the DST-NRF Centre of Excellence in Strong Materials (COE-SM). Opinions expressed and conclusions at arrived at are those of the author and are not necessarily to be attributed to the CoE-SM.

CENTRAL UNIVERSITY OF TECHNOLOGY, FREE STATE

CRPM CENTRE FOR RAPID PROTOTYPING AND MANUFACTURING

MACFLI METAL AERONAUTICAL COMPONENTS FATIGUE LIFE IMPROVEMENT GROUP

Appendix B Engineering drawing of sample array



Appendix C L-PBF Powder Specification

Powder Ti6Al4V (ELI)

A chemical composition of the employed spherical argon-atomized Ti6Al4V (ELI) powders from TLS Technik is indicated in the table below.

The 10th, 50th and 90th percentiles of equivalent diameter (weighted by volume) of the powder particles were d_{10}=11.2 µm, d_{50}=20.6 µm and d_{90}=31.8 µm.

Chemical composition of employed powders (wt. %)

Ti	Al	V	O	N	H	Fe	C	Yt
Bal	6.44	3.99	0.12	<0.002	0.001	0.19	0.007	<0.001

Appendix D Incremental Hole Drilling ASTM Standard

Designation: E 837 – 01ε1

Standard Test Method for Determining Residual Stresses by the Hole-Drilling Strain-Gage Method[1]

This standard is issued under the fixed designation E 837; the number immediately following the designation indicates the year of original adoption or, in the case of revision, the year of last revision. A number in parentheses indicates the year of last reapproval. A superscript epsilon (ε) indicates an editorial change since the last revision or reapproval.

ε[1] NOTE— Equations 17 and 18, Sections 9.2.2, 9.2.3, 11.2.5 , 11.2.6 and Table 2 were editorially upated in January 2002.

INTRODUCTION

The hole-drilling strain-gage method measures residual stresses near the surface of a material. The method involves attaching strain gages to the surface, drilling a hole in the vicinity of the gages, and measuring the relieved strains. The measured strains are then related to relieved principal stresses through a series of equations.

1. Scope

1.1 This test method covers the procedure for determining residual stresses near the surface of isotropic linearly-elastic materials. Although the concept is quite general, the test method described here is applicable in those cases where the stresses do not vary significantly with depth and do not exceed one half of the yield strength. The test method is often described as "semi-destructive" because the damage that it causes is very localized and in many cases does not significantly affect the usefulness of the specimen. In contrast, most other mechanical methods for measuring residual stress substantially destroy the specimen. Since the test method described here does cause some damage, it should be applied only in those cases either where the specimen is expendable or where the introduction of a small shallow hole will not significantly affect the usefulness of the specimen.

1.2 *This standard does not purport to address all of the safety concerns, if any, associated with its use. It is the responsibility of the user of this standard to establish appropriate safety and health practices and determine the applicability of regulatory limitations prior to use.*

2. Referenced Documents

2.1 *ASTM Standards:*

E 251 Test Methods for Performance Characteristics of Metallic Bonded Resistance Strain Gages[2]

3. Summary of Test Method

3.1 A strain gage rosette with three or more elements of the general type schematically illustrated in Fig. 1 is placed in the area under consideration. The numbering scheme for the strain gages follows a clockwise (CW) convention (**1**).[3]

NOTE 1—The gage numbering convention used for the rosette illustrated in Fig. 1 differs from the counter-clockwise (CCW) convention used for some designs of general-purpose strain gage rosettes and for some other types of residual stress rosette. If a strain gage rosette with CCW gage numbering is used, the residual stress calculation methods described in this test method still apply. The only change is a reversal in the assignment of the direction of the most tensile principal stress. This change is described in Note 7. All other aspects of the residual stress calculation are unaffected.

3.2 A hole is drilled at the geometric center of the strain gage rosette to a depth of about 0.4 of the mean diameter of the strain gage circle, D.

3.2.1 The residual stresses in the area surrounding the drilled hole relax. The relieved strains are measured with a suitable strain-recording instrument. Within the close vicinity of the hole, the relief is nearly complete when the depth of the drilled hole approaches 0.4 of the mean diameter of the strain gage circle, D.

[1] This test method is under the jurisdiction of ASTM Committee E28 on Mechanical Testing and is the direct responsibility of Subcommittee E28.13 on Residual Stress Measurement.

Current edition approved Oct. 10, 2001. Published November 2001. Originally published as E 837 – 81. Last previous edition E 837 – 99.

[2] *Annual Book of ASTM Standards*, Vol 03.01.

[3] The boldface numbers in parentheses refer to the list of references at the end of this test method.

Copyright © ASTM International, 100 Barr Harbor Drive, PO Box C700, West Conshohocken, PA 19428-2959, United States.

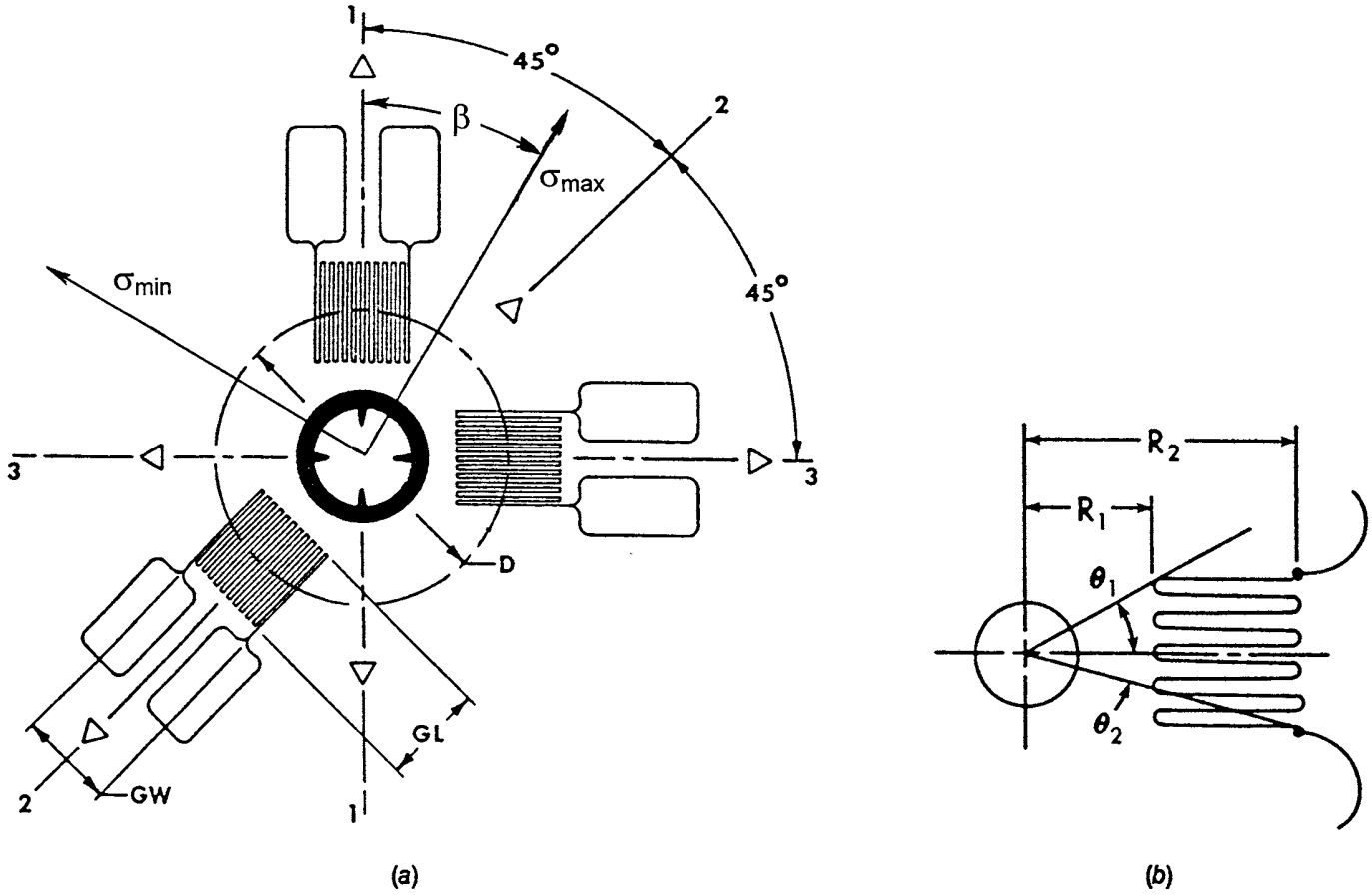


FIG. 1 Schematic Diagram Showing the Geometry of a Typical Three-Element Clockwise (CW) Strain Gage Rosette for the Hole-Drilling Method

3.3 Fig. 2 shows a schematic representation of the residual

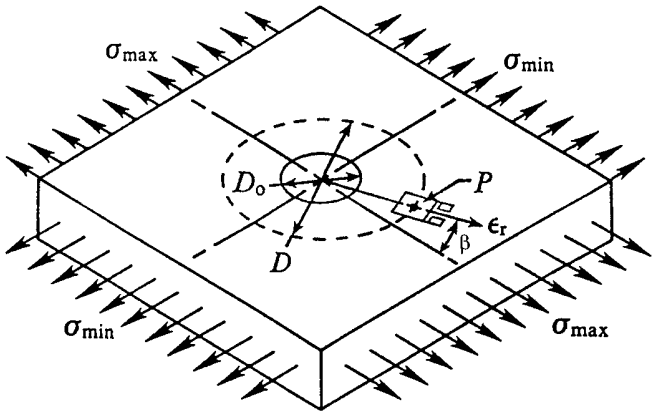


FIG. 2 Definitions of Symbols

stress and a typical surface strain relieved when a hole is drilled into a material specimen. The surface strain relief is related to the relieved principal stresses by the following relationship:

$$\epsilon_r = (\bar{A} + \bar{B}\cos 2\beta)\sigma_{max} + (\bar{A} - \bar{B}\cos 2\beta)\sigma_{min} \quad (1)$$

where:

ϵ_r = relieved strain measured by a radially aligned strain gage centered at P,
$\bar{A},\bar{B}$ = calibration constants,
σ_{max} = maximum (most tensile) and
σ_{min} = minimum (most compressive) principal stresses present at the hole location before drilling,
β = angle measured clockwise from the direction of gage 1 to the direction of σ_{max},
D = diameter of the gage circle,
D_0 = diameter of the drilled hole.

3.3.1 The following equations may be used to evaluate the constants $\bar{A}$ and $\bar{B}$ for a material with given elastic properties:

$$\bar{A} = -\bar{a}\,(1+\nu)\,/\,(2E) \quad (2)$$

$$\bar{B} = -\bar{b}\,/\,(2E) \quad (3)$$

where:

E = Young's modulus,

ν = Poisson's ratio, and

$\bar{a}$ and $\bar{b}$ are dimensionless, almost material-independent constants (see Note 2). Slightly different values of these constants apply for a through-thickness hole made in a thin specimen and for a blind hole made in a thick specimen. The numerical values of these constants are provided in this test method.

NOTE 2—The dimensionless coefficients $\bar{a}$ and $\bar{b}$ vary with hole depth, as indicated in Table 1. They are both nearly material-independent. They do not depend on Young's modulus, E, and they vary by less than 1 % for Poisson's ratios in the range 0.28 to 0.33. For a through-hole in a thin plate, $\bar{a}$ is independent of Poisson's ratio.

3.3.2 The relieved strains ϵ_1, ϵ_2, and ϵ_3 are measured by three correspondingly numbered strain gages as shown in Fig. 1. For specialized applications, a rosette with three pairs of strain gages arranged in directions 1 - 2 - 3 may be used (see 5.2.3). Measurement of these three relieved strains provides sufficient information to calculate the principal stresses σ_{max} and σ_{min} and their orientation β.

3.3.3 For reasons of pictorial clarity in Fig. 2, the principal residual stresses σ_{max} and σ_{min} are shown as uniformly acting over the entire region around the hole location. In actuality, it is not necessary for the residual stresses to be uniform over such a large region. The relieved surface strains depend only on the principal stresses that originally existed at the boundaries of the hole (2). The stresses beyond the hole boundaries do not affect the relieved strains. Because of this, the hole-drilling method provides a very localized measurement of residual stresses.

3.3.4 It is assumed that the variations of the original stresses within the boundaries of the hole are small and that the variation with depth is negligible. It is not necessary for the original stresses outside of the hole location to be uniform.

4. Significance and Use

4.1 Residual stresses are present in almost all structures. They may be present as a result of manufacturing processes or they may occur during the life of the structure. In many cases residual stresses are a major factor in the failure of a structure, particularly one subjected to alternating service loads or corrosive environments. Residual stress may also be beneficial

TABLE 1 Numerical Values of Coefficients $\bar{a}$ and $\bar{b}$

Rosette A	$\bar{a}$					$\bar{b}$				
Blind hole	Hole Diameter, D_0/D					Hole Diameter, D_0/D				
Depth/D	0.30	0.35	0.40	0.45	0.50	0.30	0.35	0.40	0.45	0.50
0.00	.000	.000	.000	.000	.000	.000	.000	.000	.000	.000
0.05	.027	.037	.049	.063	.080	.051	.069	.090	.113	.140
0.10	.059	.081	.108	.138	.176	.118	.159	.206	.255	.317
0.15	.085	.115	.151	.192	.238	.180	.239	.305	.375	.453
0.20	.101	.137	.177	.223	.273	.227	.299	.377	.459	.545
0.25	.110	.147	.190	.238	.288	.259	.339	.425	.513	.603
0.30	.113	.151	.195	.243	.293	.279	.364	.454	.546	.638
0.35	.113	.151	.195	.242	.292	.292	.379	.472	.566	.657
0.40	.111	.149	.192	.239	.289	.297	.387	.482	.576	.668
Through Hole	.090	.122	.160	.203	.249	.288	.377	.470	.562	.651
Rosette B	$\bar{a}$					$\bar{b}$				
Blind Hole	Hole Diameter, D_0/D					Hole Diameter, D_0/D				
Depth/D	0.30	0.35	0.40	0.45	0.50	0.30	0.35	0.40	0.45	0.50
0.00	.000	.000	.000	.000	.000	.000	.000	.000	.000	.000
0.05	.029	.039	.053	.068	.086	.058	.078	.102	.127	.157
0.10	.063	.087	.116	.148	.189	.134	.179	.231	.286	.355
0.15	.090	.123	.162	.205	.254	.203	.269	.343	.419	.504
0.20	.107	.145	.189	.236	.289	.256	.336	.423	.511	.605
0.25	.116	.156	.202	.251	.305	.292	.381	.476	.571	.668
0.30	.120	.160	.206	.256	.309	.315	.410	.509	.609	.707
0.35	.120	.160	.206	.256	.308	.330	.427	.529	.631	.730
0.40	.118	.158	.203	.253	.305	.337	.437	.541	.644	.743
Through Hole	.096	.131	.171	.216	.265	.329	.428	.531	.630	.725
Rosette C	$\bar{a}$					$\bar{b}$				
Blind Hole	Hole Diameter, D_0/D					Hole Diameter, D_0/D				
Depth/D	0.40	0.45	0.50	0.55	0.60	0.40	0.45	0.50	0.55	0.60
0.00	.000	.000	.000	.000	.000	.000	.000	.000	.000	.000
0.05	.065	.084	.106	.130	.157	.105	.132	.158	.185	.217
0.10	.147	.191	.238	.293	.361	.250	.314	.373	.440	.519
0.15	.218	.281	.347	.420	.506	.391	.484	.570	.658	.754
0.20	.270	.343	.421	.504	.595	.506	.617	.719	.816	.912
0.25	.302	.381	.465	.554	.648	.591	.712	.823	.923	1.015
0.30	.321	.403	.491	.583	.679	.650	.778	.893	.994	1.081
0.35	.331	.415	.505	.599	.698	.690	.822	.939	1.041	1.125
0.40	.336	.421	.512	.608	.709	.719	.851	.970	1.073	1.154
Through Hole	.316	.399	.494	.597	.707	.623	.723	.799	.847	.859

as, for example, compressive stresses produced by shot peening. The hole-drilling strain-gage technique is a practical method for determining residual stresses. See Table 1.

5. Strain Gages

5.1 A rosette comprising three single or pairs of strain gage grids shall be used.

NOTE 3—It is recommended that the gages be calibrated in accordance with Test Methods E 251.

5.1.1 The gages shall be arranged in a circular pattern, equidistant from the center of the rosette.

5.1.2 The principal gage axes shall be oriented in each of three directions, *(1)* a reference direction, *(2)* 45° or 135° to the reference direction, and *(3)* perpendicular to the reference direction. Direction *(2)* bisects directions *(1)* and *(3)*, (see Fig. 1).

5.2 Several different standardized rosettes are available to meet a wide range of residual stress measurement needs.[4] Fig. 3 shows three different rosette types.

5.2.1 Fig. 3 (a) shows the type A rosette, first introduced by Rendleer and Vigness (**3**). This pattern is available in several different sizes, and is recommended for general-purpose use.

5.2.2 Fig. 3 (b) shows thr type B rosette. This pattern has all strain gage grids located on one side. It is useful where measurements need to be made near an obstacle.

5.2.3 Fig. 3 (c) shows the type C rosette. This special-purpose pattern has three pairs of opposite strain gage grids that are to be connected as three half-bridges. It is useful where large strain sensitivity and high thermal stability are required (**19**).

NOTE 4—Standardized hole-drilling rosette patterns were first proposed by Rendler and Vigness (**3**). The use of standardized rosette designs greatly simplifies the calculation of the residual stresses.

5.3 The center of the gage circle shall be clearly identifiable both before and after the drilling operation.

5.4 The application of the strain gage (cementing, wiring, protective coating) shall closely follow the manufacturer's recommendations, and shall ensure the protection of the strain gage grid during the drilling operation.

5.5 The strain gages shall remain permanently connected and the stability of the installation shall be verified. A resistance to ground of at least 20 000 MΩ is preferable.

6. Instrumentation

6.1 The instrumentation for recording of strains shall have a strain resolution of $\pm 2 \times 10^{-6}$, and stability and repeatability of the measurement shall be at least $\pm 2 \times 10^{-6}$. The lead wires from each gage should be as short as practicable and a three-wire temperature-compensating circuit (**4**) should be used with rosette types A and B. Half-bridge circuits should be used with rosette type C, the resulting outputs of which are designated ϵ_1, ϵ_2, and ϵ_3.

[4] Strain gage patterns of these designs are manufactured by Measurements Group, Wendell, NC.

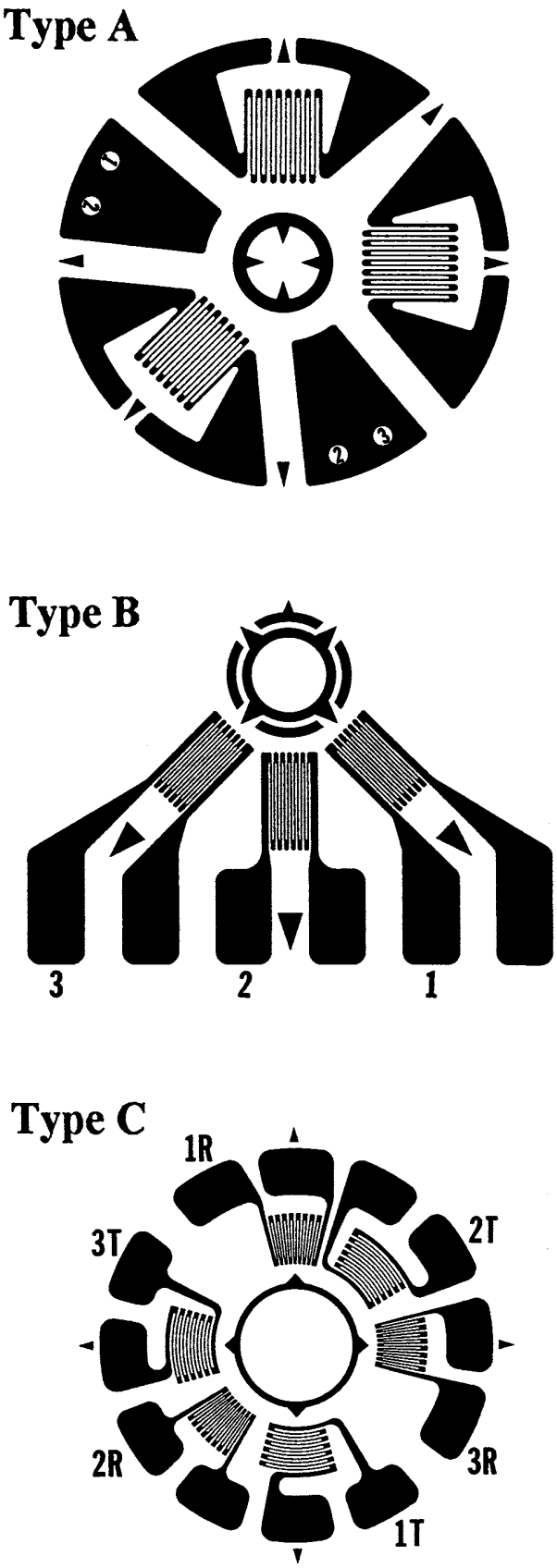


FIG. 3 Hole-Drilling Rosettes

NOTE 5—In general, surface preparation should be restricted to those methods which have been demonstrated to induce no significant residual surface stresses.

7. Specimen Preparation

7.1 The surface preparation prior to cementing the strain gage shall conform to the recommendations of the manufacturer of the cement used to attach the strain gage.

7.1.1 A thorough cleaning and degreasing is required.

7.1.2 A smooth surface is usually necessary for strain gage application. However, abrading or grinding that could appreciably alter the surface stresses must be avoided.

8. Procedure

8.1 *Drilling*:

8.1.1 To protect the strain gage grids, a margin of at least 0.012 in. (0.30 mm) should be allowed between the hole boundary and the end loops of the strain gage grids. The need for this margin limits the maximum allowable diameter, D_0 of the drilled hole. The minimum recommended hole diameter is 60 % of the maximum allowable diameter. Table 2 lists the recommended hole diameter ranges for several common strain gage rosette types.

NOTE 6—As the ratio D_0 / D increases, the sensitivity of the method increases in approximate proportion to $(D_0 / D)^2$. In general, larger holes are recommended because of the increased sensitivity.

8.1.2 The center of the drilled hole shall coincide with the center of the strain gage circle to within either ±0.004 D or ±0.001 in. (±0.025 mm), whichever is greater. Errors due to misalignment of the drilled hole could produce significant errors in the calculated stress. To avoid these errors, it is recommended that an optical device be used for centering the tool holder. A device suitable for this is shown in Fig. 4.[5]

8.1.3 Select the drilling operation and tool to minimize or eliminate the introduction of plastic deformation in the area surrounding the drilled hole.

8.1.3.1 Several drilling techniques have been investigated and reported to be suitable for the hole drilling method:

(1) Abrasive jet machining,[6] a method for hole drilling in which a high-velocity stream of air containing fine abrasive particles is directed against the workpiece through a small-diameter nozzle, has been used successfully (**5, 6**). However, this technique may not be suitable for softer materials such as copper (**7**).

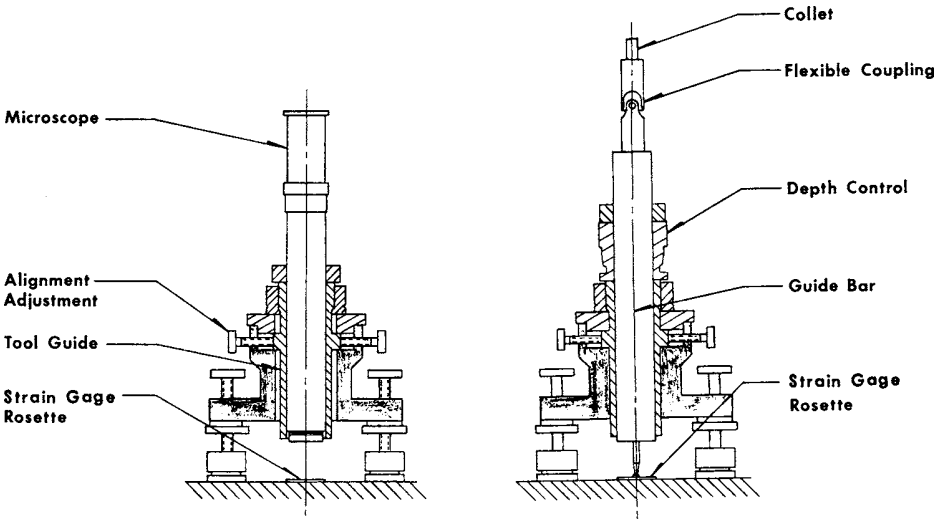
(2) Drilling at very high speed (up to 400 000 rpm) with an air turbine has also been used successfully in this application (**8**). This technique is believed to be generally suitable except for extremely hard materials such as stellite (**7**).

(3) End mills, carbide drills, and modified end mills have been used successfully in a number of studies (**3, 9, 10, 11**). It appears, however, that low-speed drilling with an end mill may be less suitable than abrasive jet machining or high-speed drilling (**7**).

Since any residual stress created by the selected drilling method will adversely affect the accuracy of results, a verification of the selected process is recommended when no prior experience is available. Such verification could consist of applying a strain gage rosette, identical to the rosette used in the test, to a stress-free specimen of the same nominal composition, and then drilling a hole. If the drilling method is satisfactory, the stresses produced by drilling will be small.

[5] A device for centering the tool is manufactured by Measurements Group, Wendell, NC.

[6] Tools for abrasive jet machining may be obtained from S. S. White, Piscataway, NJ.



(*a*) *Alignment*—Tool guide aligned with the center of gage circle

(*b*) *Hole Milling*—After removing the alignment microscope, the drilling tool is introduced

FIG. 4 A Device for Centering the Tool Holder

TABLE 2 Rosette Dimensions and Recommended Hole Diameters[A]

Rosette Type[B]	D	GL	GW	R_1	R_2	Min D_o	Max D_o[C]
Type A Rosette Conceptual	D	0.309 D	0.309 D	0.3455 D	0.6545 D	0.6 Max D_o	Max D_o
1/32 in. nominal	0.101 (2.57)	0.031 (0.79)	0.031 (0.79)	0.035 (0.89)	0.066 (1.68)	0.024 (0.61)	0.040 (1.01)
1/16 in. nominal	0.202 (5.13)	0.062 (1.59)	0.062 (1.59)	0.070 (1.77)	0.132 (3.36)	0.060 (1.52)	0.100 (2.54)
1/8 in. nominal	0.404 (10.26)	0.125 (3.18)	0.125 (3.18)	0.140 (3.54)	0.264 (6.72)	0.132 (3.35)	0.220 (5.59)
Type B Rosette Conceptual	D	0.309 D	0.223 D	0.3455 D	0.6545 D	0.6 Max D_o	Max D_o
1/16 in. nominal	0.202 (5.13)	0.062 (1.59)	0.045 (1.14)	0.070 (1.77)	0.132 (3.36)	0.060 (1.52)	0.100 (2.54)
Type C Rosette Conceptual	D	0.176 D	30° sector	0.412 D	0.588 D	0.6 Max D_o	Max D_o
1/16 in. nominal	0.170 (4.32)	0.030 (0.76)	30° (30°)	0.070 (1.78)	0.100 (2.54)	0.060 (1.52)	0.100 (2.54)

[A]Dimensions are in inches. Dimensions in parentheses are in mm.
[B]Rosette dimensions defined in Fig. 1.
[C]From 8.1.1.

NOTE 7—The most commonly used approach to obtaining stress-free specimens is the annealing heat treatment method (**5, 6, 7, 15, 16**). Recent research (**18**) suggests that electric discharge machining may also merit consideration as a means for removing small stress-free samples from bulk materials. As a general rule, the smaller the sample, the smaller the residual macrostresses that the sample will be able to sustain although it must, of course, be compatible with the size of the strain gage rosette.

NOTE 8—If the drilling method generates measurable levels of residual stress which are reproducible, experimental calibration should be considered (see 9.3).

8.1.3.2 When end mills are used, proceed with the drilling using very light axial thrust and slowly, to permit ample time for heat dissipation.

8.1.4 Carry out the hole drilling test at constant temperature.

8.2 Obtain zero readings from each gage before starting the drilling operation. Then, commence drilling using one of the following two procedures, depending on the thickness of the material specimen.

8.2.1 A specimen whose thickness is at least 1.2D is considered to be "thick." For such a specimen, obtain eight sets of strain readings ϵ_1, ϵ_2, ϵ_3, as the hole depth is increased in increments of 0.05D, up to a final hole depth of 0.4D. Other similar depth increments are acceptable; however, they are less convenient for calculations because they will require additional interpolation or extrapolation of the calibration constants in Table 1.

8.2.2 A specimen whose thickness is less than 0.4D is considered to be "thin." For such a specimen, obtain one set of strain readings ϵ_1, ϵ_2, ϵ_3, after a hole has been drilled through the entire thickness of the specimen.

8.2.3 The intermediate case when the specimen thickness is between 0.4D and 1.2D is not within the scope of this Standard Test Method. An approximate result can be otained for such specimens by using a through hole and interpolating the "Blind Hole" and "Through-the-thickness Hole" calibration data given in Table 1. Residual stress results obtained in this way should be reported as "nonstandard" and "approximate."

8.3 Compute the following combination strains for each set of measured strains ϵ_1, ϵ_2, ϵ_3:

$$p = (\epsilon_3 + \epsilon_1)/2 \quad (4)$$

$$q = (\epsilon_3 - \epsilon_1)/2 \quad (5)$$

$$t = (\epsilon_3 + \epsilon_1 - 2\,\epsilon_2)/2 \quad (6)$$

8.3.1 When working with a "thick" specimen, a test should be made to check that the residual stresses are uniform whithin the hole depth. In this case, identify the numerically larger set of combination strains q or t. Express each set of combination strains p and the larger of q and t as a percentage of their values when the hole depth = 0.4 D. Plot these percent strains versus (hole depth/D). These graphs should yield data points very close to the curves shown in Fig. 5 (**12**). Data points that are removed from the curves in Fig. 5 by more than ±3 % indicate either substantial stress nonuniformity through the material thickness, or strain measurement errors. In either case, the measured data are not acceptable for residual stress calculations using the procedure described here. Other publications, for example, Ref (**21**), give details of methods for evaluating nonuniform residual stresses from incremental hole-drilling strain data. However, such calculations do not fall within the scope of this test method.

NOTE 9—This graphical test is not a sensitive indicator of stress field uniformity. Specimens with significantly non-uniform stress fields can yield percentage relieved strain curves substantially similar to those shown in Fig. 5. The main purpose of the test is to identify grossly non-uniform stress fields and also strain measurement errors. This stress

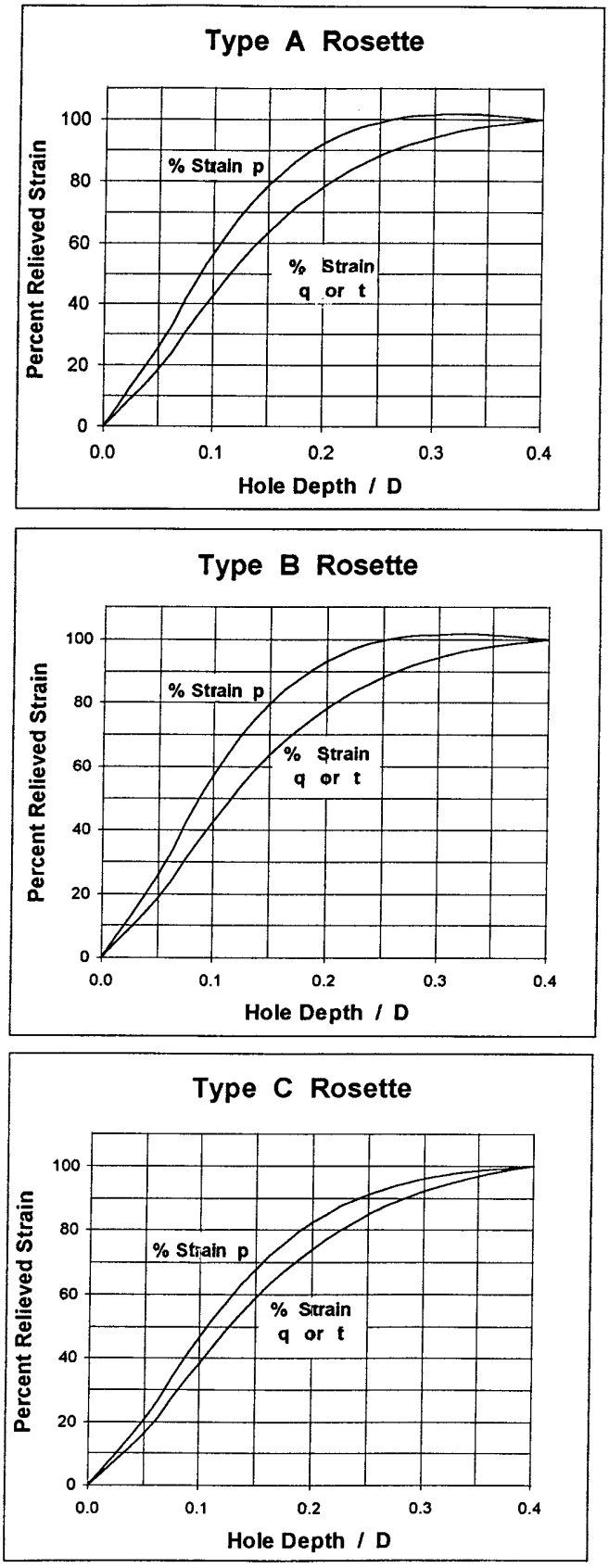


FIG. 5 Typical Plots of Percent of Strain versus Depth for Stress Uniform Through the Thickness, (a) Type A Rosette, (b) Type B Rosette, (c) Type C Rosette

uniformity test is available only when working with "thick" specimens.

9. Computation of Stresses

9.1 *Thin Specimen*:

9.1.1 In the case of a "thin" specimen, only a single set of ϵ_1, ϵ_2, and ϵ_3 measurements is needed to calculate the magnitude and directions of the principal residual stresses. These stresses are assumed to be uniform through the specimen thickness.

9.1.2 The more tensile (or less compressive) principal stress σ_{max} is located at an angle β measured clockwise from the direction of gage 1 in Fig. 1. Similarly, the less tensile (or more compressive) principal stress σ_{min} is located at an angle β measured clockwise from the direction of gage 3.

9.1.3 Compute the angle β from

$$\beta = \frac{1}{2} \arctan (t/q) \tag{7}$$

9.1.4 Direct calculation of the angle β using the common one-argument arctan function, such as is found on an ordinary calculator, can give an error of ±90°. The correct angle can be found by using the two-argument arctan function (function ATAN2 in some computer languages), where the signs of the numerator and denominator are each taken into account. Alternatively, the result from the one-argument calculation can be adjusted by ±90° as necessary to place β within the appropriate range defined in the following table:

	q = < 0	q = 0	q > 0
t > 0	45° < β < 90°	45°	0° < β < 45°
t = 0	90°	undefined	0°
t < 0	−90° < β < − 45°	−45°	−45° < β < 0°

9.1.5 A positive value of β, say β = 30°, indicates that σ_{max} lies 30° clockwise of the direction of gage 1. A negative value of β, say β = −30°, indicates that σ_{max} lies 30° counter-clockwise of the direction of gage 1.

9.1.6 In general, the direction of σ_{max} will closely coincide with the direction of the numerically most negative (compressive) relieved strain. The case where both q = 0 and t = 0 corresponds to an equal biaxial stress field, for which the angle β has no meaning.

NOTE 10—The clockwise measurement direction for angle β defined in 9.1.2 applies only to a strain gage rosette with CW gage numbering, such as that illustrated in Fig. 1. The opposite measurement direction for β applies to a CCW strain gage rosette. In such a rosette the geometrical locations of gages 1 and 3 are interchanged relative to the CW case. The new gage 1 becomes the reference gage. For a CCW rosette, a positive value of β, say β = 30°, indicates that σ_{max} lies 30° counter-clockwise of the direction of gage 1. A negative value of β, say β = −30°, indicates that σ_{max} lies 30° clockwise of the direction of gage 1. All other aspects of the residual stress calculation are identical for both CW and CCW rosettes.

9.1.7 Compute the stresses σ_{max} and σ_{min} from

$$\sigma_{min}, \sigma_{max} = -[p/\bar{a}(1+\nu) \pm \sqrt{(q^2+t^2)/\bar{b}}]E \tag{8}$$

The negative square root in this equation is associated with σ_{max} because the leading minus sign on the right of Eq 8. A tensile (+) residual stress will produce a compressive (–) relieved strain.

9.1.8 Use Table 1 to determine the numerical values of the calibration constants $\bar{a}$ and $\bar{b}$ corresponding to the hole diameter and type of rosette used.

9.2 *"Thick" Specimen*:

9.2.1 In the case of a "thick" specimen, all sets of ϵ_1, ϵ_2, ϵ_3 measurements are used to calculate the magnitude and directions of the principal residual stresses. These stresses are assumed to be be uniform throughout the hole depth.

NOTE 11—It is possible to do a calculation similar to that described in 9.1 using only one set of the ϵ_1, ϵ_2, ϵ_3 measurements, say the values at 0.4D. Such a calculation could be useful to give a quick residual stress estimate; however, the averaging method described in 9.2 is preferred because it uses all the measured strain data, and it significantly reduces the effects of random strain measurement errors.

9.2.2 For each of the hole depths corresponding to the eight sets of ϵ_1, ϵ_2, ϵ_3 measurements, use Table 1 to determine the numerical values of the calibration constants $\bar{a}$and $\bar{b}$ corresponding to the hole diameter and type of rosette used. The numerical values in this table derive from finite element analyses **(14)** and are found to be in excellent agreement with experimental results.

9.2.3 Compute the three combination stresses *P*, *Q* and *T* corresponding to the three combination strains *p, q*, and *t* using the following formulas **(20)**:

$$P = -E \times (\Sigma\bar{a} \cdot p) / (\Sigma\bar{a}^2) / (1 + \nu) \tag{9}$$

$$Q = -E \times (\Sigma\bar{b} \cdot q) / (\Sigma\bar{b}^2) \tag{10}$$

$$T = -E \times (\Sigma\bar{b} \cdot t) / (\Sigma\bar{b}^2) \tag{11}$$

where Σ indicates a summation of the indicated quantities for the eight hole depths.

The stability of the stress results obtained using Eq 9-11 is demonstrated in **(22)**.

9.2.4 Compute the angle β from:

$$\beta = \frac{1}{2} \arctan (-T / -Q) \tag{12}$$

$$= \frac{1}{2} \arctan (\Sigma\bar{b} \cdot t / \Sigma\bar{b} \cdot q)$$

Angle β can be placed in the correct quadrant by evaluating the "arctan" function in a manner analogous to that described in 9.1.3.

9.2.5 Compute the stresses σ_{max} and σ_{min} from:

$$\sigma_{max}, \sigma_{min} = P \pm \sqrt{(Q^2 + T^2)} \tag{13}$$

9.3 *Experimental Calibration*:

9.3.1 If required, the constants $\bar{a}$ and $\bar{b}$ relating the stresses σ_{max} and σ_{min} to the measured strains ϵ_i can be established using a calibration experiment.

When making calibrations for a "thin" specimen (thickness less than 0.4D), use the same thickness as the actual test specimen. When making calibrations for a "thick specimen", a thickness, *T*, of 1.2D or greater is required.

9.3.2 Before drilling the hole, apply the calibration force in five equal steps up to the maximum force. This maximum force should not produce a stress σ_{cal} larger than one-third of the yield stress of the test material.

9.3.3 Compute the combination strains *p, q*, and *t* corresponding to the measured strains of ϵ_1, ϵ_2 and ϵ_3 using Eq 4-6. Plot graphs of *p, q*, and *t* versus the applied stresses. These graphs should be straight lines. Determine their gradients *gp, gq*, and *gt*.

9.3.4 When working with a "thin" specimen, drill a through-hole and repeat the strain measurements for a sequence of five equal loading steps up to the maximum force.

9.3.5 When working with a "thick" specimen, drill a blind hole in a series of eight hole depth increments of 0.05D up to a maximum of 0.4D. After each hole depth increment, repeat the strain measurements for a sequence of five equal loading steps up to the maximum force.

9.3.6 Subtract the *p, q*, and *t* gradients measured before any hole drilling from the corresponding gradients at each hole depth:

$$(gp)_{cal} = (gp)_{hole} - (gp)_{before} \tag{14}$$

$$(gq)_{cal} = (gq)_{hole} - (gq)_{before} \tag{15}$$

$$(gt)_{cal} = (gt)_{hole} - (gt)_{before} \tag{16}$$

The calibrated values of constants $\bar{a}$ and $\bar{b}$ for the eight depths to be used in equations (9) – (12) are:

$$\bar{a} = -2(gp)_{cal} \times E / (1+\nu) \tag{17}$$

$$\bar{b} = 2\sqrt{((gq)^2_{cal} + (gt)^2_{cal})} \times E \tag{18}$$

10. Report

10.1 Report the following information:

10.1.1 Description of the test specimen,

10.1.1.1 Material,

10.1.1.2 Pertinent mechanical properties,

10.1.2 Location of strain gages,

10.1.3 Model and type of strain gages used,

10.1.3.1 Strain gage geometry,

10.1.4 The method used to drill the hole,

10.1.5 Plot of strain versus depth for each gage,

10.1.6 Tabulation of strains ϵ_1, ϵ_2, and ϵ_3 at all locations, and

10.1.7 Tabulation of stresses and direction of stresses at all locations.

11. Precision and Bias

11.1 *Bias*:

11.1.1 Residual stresses determined by this method may be expected to exhibit a bias not exceeding ±10 % provided that the conditions set forth in 1.1 apply and the drilling technique does not induce significant machining stresses in the material (**6**, **15**). The most elusive of these conditions may be the requirement that the residual stresses not vary significantly with depth. Residual stresses are commonly induced by various working, forming, welding, and other manufacturing processes which involve the application of energy to and through the surface of the object. As a result, there are usually stress gradients near the surface, and a depthwise uniform residual stress is apt to be rarely encountered. If a significant nonuniform stress distribution goes unrecognized, the error may be much more than 10 %, and will usually be in the direction of underestimating the maximum stress.

11.2 *Precision*:

11.2.1 A round-robin test program (**16**) was carried out on AISI 1018 carbon-steel specimens that had been subjected to a prior stress relief treatment. High-speed, low-speed, and air abrasive drilling were used. In all, measurements were made by eight laboratories on eight nominally identical specimens, giving a standard deviation of 2.0 ksi (14 MPa) about the mean of all 26 measurements.

11.2.2 A round-robin test program (**17**) was carried out on type 304 stainless steel specimens that had been subjected to a prior stress relief treatment. In all, 46 nominally identical specimens were tested by 35 laboratories using a variety of methods. Forty-six residual stress measurements, made using high-speed drilling and air abrasive drilling, produced standard deviations that did not exceed 1.7 ksi (12 MPa) about the mean of either drilling technique. Results of six measurements made using low-speed drilling were not consistent.

11.2.3 The variability of results obtained on stressed specimens may be expected to be considerably greater than that observed on specimens that are relatively stress free. A round-robin test program on stressed stainless steel specimens is being planned by the Residual Stress Technical Division of the Society for Experimental Mechanics with participation by ASTM Subcommittee E28.13.

11.2.4 Evaluations of the precision of this test method as applied to carbon or stainless steels may not be applicable to other materials, which exhibit machineability characteristics that differ considerably from those of steel and even from each other. The high-speed hole drilling technique has been reported as being effective with such diverse materials as copper, aluminum, zirconium and stellite (**7**).

11.2.5 Eq 9-11 reduce the effect that random experimental errors have on the results, and improve the precision. Random experimental errors occur at individual drilling depths from events like strain reading errors, strain gage anomalies, and test environment changes. The best-fit techniques of strain data averaging used in Eq 9-11 can accommodate large random experimental errors without significant stress errors(**20**).

11.2.6 Use of the six-element rosette, type C, increases electrical output for a given residual stress level, compared with the three-element types A and B. This increase in electrical sensitivity can improve the precision of the hole-drilling measurements. However, use of six-element rosettes involves greater installation effort and expense. For general-purpose work, rosette types A and B typically give satisfactory results. Type C rosettes are appropriate for critical applications and for work with low-conductivity materials.

12. Keywords

12.1 hole-drilling; residual stress measurement; strain gages; stress analysis

REFERENCES

(1) Perry, C. G. "Data-Reduction Algorithms for Strain-Gage Rosette Measurements," Experimental Techniques, Vol 12, No. 5, 1989, pp. 13–18.

(2) Schajer, G. S.," Application of Finite Element Calculations to Residual Stress Measurements," Journal of Engineering Materials and Technology, *Transactions*, ASME, Vol 103, April 1981, pp. 157–163.

(3) Rendler, N. J., and Vigness, I., "Hole-Drilling Strain Gage Method of Measuring Residual Stresses," *Experimental Mechanics*, Vol 6, No. 12, 1966, pp. 577–586.

(4) Perry, C. C., and Lissner, H. R., *Strain Gage Primer*, McGraw-Hill Book Co., Inc., New York, NY, 1955

(5) Bush, A. J., and Kromer, F. J., "Simplification of the Hole-Drilling Method of Residual Stress Measurements," *ISA Transaction*, Vol 112, No. 3, 1973, pp. 249–260.

(6) Beaney, E. M., "Accurate Measurements of Residual Stress on Any Steel Using the Centre Hole Method," *Strain*, *Journal BSSM*, Vol 12, No. 3, 1976, pp. 99–106.

(7) Flaman, M. T., and Herring, J. A., "Comparison of Four Hole-Producing Techniques for the Center-Hole Residual-Stress Measurement Method," *Experimental Techniques*, Vol 9, No. 8, 1985, pp. 30–32.

(8) Flaman, M. T., "Investigation of Ultra-High Speed Drilling for Residual Stress Measurements by the Center Hole Method," *Experimental Mechanics*, Vol 22, No. 1, 1982, pp. 26–30.

(9) Kelsey, R. A., "Measuring Non-Uniform Residual Stresses by the Hole Drilling Method," *Proceedings*, SESA, Vol 14, No. 1, 1956, pp. 181–194.

(10) Sandifer, J. P., and Bowie, G. E., "Residual Stress by Blind Hole Method with Off-Center Hole," *Experimental Mechanics*, Vol 18, No. 5, 1978, pp. 173–179.

(11) "Measurement of Residual Stresses by the Hole Drilling Strain Gage Method," *Tech Note TN-503-4*, Measurements Group, Raleigh, NC.

(12) Schajer, G. S. "Judgment of Residual Stress Field Uniformity when Using the Hole-Drilling Method," Proceedings of the International Conference on Residual Stresses II, Nancy, France. November 23–25, 1988, pp. 71–77.

(13) Redner, S., and Perry, C. C., "Factors Affecting the Accuracy of Residual Stress Measurements Using the Blind Hole Drilling Method," *Proceedings of 7th International Conference Experimental Stress Analysis*, August 1982, pp. 604–616.

(14) Schajer, G. S. "Measurement of Non-Uniform Residual Stresses Using the Hole Drilling Method," Journal of Engineering Materials and Technology, Vol 110, No. 4, 1988, Part I: pp. 338–343, Part II: pp. 344–349.

(15) Beaney, E. M., and Procter, E., "A Critical Evaluation of the Centre Hole Technique for the Measurement of Residual Stresses," *Strain*, Vol 10, No. 1, 1974, pp. 7–14, 52.

(16) Yavelak, J. J. (compiler), "Bulk-Zero Stress Standard—AISI 1018 Carbon-Steel Specimens, Round Robin Phase 1," *Experimental Techniques*, Vol 9, No. 4, 1985, pp. 38–41.

(17) Flaman, M. T., and Herring, J. A., "SEM/ASTM Round-Robin Residual-Stress-Measurement Study—Phase 1, 304 Stainless-Steel Specimen," *Experimental Techniques*, Vol 10, No. 5, 1986, pp. 23–25.

(18) Weng, C. C., Lin, Y. C., and Chou, C. P., "A Study on the Induced Drilling Stresses in the Centre Hole Method of Residual Stress Measurement," *Strain*, Vol 28, 1992, pp. 45–51.

(19) Schajer, G. S., and Tootoonian, M., "A New Rosette Design for More Reliable Hole-Drilling Residual Stress Measurements," *Experimental Mechanics*, Vol 37, No. 3, 1997, pp. 299–306.

(20) Schajer, G. S., "Strain Data Averaging for the Hole-Drilling Method." *Experimental Techniques*, Vol 15, No. 2, 1991, pp. 25–28.

(21) Lu, J. (ed.)," Handbook of Measurement of Residual Stresses," *Society for Experimental Mechanics*, Fairmont Press, Lilburn, GA, 1996, Chapter 2.

(22) Kroenke, W.C., Holloway, A.M., and Mabe, W.R., "Stress Calculation Update in ASTM E 837 Residual Stress Hole Drilling Standard", *Advances in Computational Engineering & Sciences*, Tech Science Press, Vol. 1, 2000, p. 695–699.

ASTM International takes no position respecting the validity of any patent rights asserted in connection with any item mentioned in this standard. Users of this standard are expressly advised that determination of the validity of any such patent rights, and the risk of infringement of such rights, are entirely their own responsibility.

This standard is subject to revision at any time by the responsible technical committee and must be reviewed every five years and if not revised, either reapproved or withdrawn. Your comments are invited either for revision of this standard or for additional standards and should be addressed to ASTM International Headquarters. Your comments will receive careful consideration at a meeting of the responsible technical committee, which you may attend. If you feel that your comments have not received a fair hearing you should make your views known to the ASTM Committee on Standards, at the address shown below.

This standard is copyrighted by ASTM International, 100 Barr Harbor Drive, PO Box C700, West Conshohocken, PA 19428-2959, United States. Individual reprints (single or multiple copies) of this standard may be obtained by contacting ASTM at the above address or at 610-832-9585 (phone), 610-832-9555 (fax), or service@astm.org (e-mail); or through the ASTM website (www.astm.org).